DSPACE

https://dspace.org/

Monitoring crop water use using unmanned aerial vehicle (UAV) and surface energy balance algorithms: a case study of Vaalharts Irrigation Scheme, Northern Cape Province, South Africa

Ratshiedana, Phathutshedzo Eugene

2022

https://hdl.handle.net/10539/34571

Downloaded from a DSpace repository. https://dspace.org/

UNIVERSITY OF THE
WITWATERSRAND,
JOHANNESBURG

Monitoring crop water use using unmanned aerial vehicle (UAV) and surface energy balance algorithms: A case study of Vaalharts Irrigation Scheme, Northern Cape Province, South Africa

By

Ratshiedana Phathutshedzo Eugene (2386546)

Supervisor: Prof. Mohamed A. M. Abd Elbasit (Sol Plaatje University)

Co-supervisor: Prof. Elhadi Adam (University of the Witwatersrand)

A dissertation submitted to the Faculty of Science, University of the Witwatersrand, Johannesburg, in fulfilment of the requirements for the degree of Master of Science

Faculty of Science

School of geography, archaeology and environmental studies

University of the Witwatersrand Johannesburg, South Africa

June 2022

Johannesburg, South Africa

ABSTRACT

Crop water use is an important component of the hydrological system. The fact that there is continuous and persistent drought in the face of global environmental change and ongoing tensions over water use is enough to warrant crop water use monitoring. This study applied different methods to quantify crop water use in an 18-hectare barley field accurately. Soil water content spatial distribution was determined by integrating ground measurements using a Daiki-311A soil moisture meter probe, an HS2 Hydrosense II handheld sensor and by calibration of soil electrical conductivity fluxes recorded using an electromagnetic induction instrument (EM 38). Estimating evapotranspiration was done using different approaches, including smart weather station data for reference evapotranspiration by applying Penman-Monteith, Priestley and Taylor's methods. In contrast, actual evapotranspiration was estimated using two smart field weighing lysimeters and Unmanned Aerial Vehicle (UAV) data in a temperature-vegetation triangular algorithm. The results for this research are presented as graphs and spatial distribution maps, while their comparisons and evaluations were made using statistical approaches. The findings were that the determination of crop water use and soil water content makes it possible for stakeholders in agriculture to determine irrigation requirement, irrigation scheduling, water use monitoring, and irrigation planning, which is positively attributed to water resources management. The evapotranspiration obtained from the UAV remote sensing simulation showed coherence with the lysimetric evapotranspiration. The soil water content obtained using ground handheld sensors was consistent with the soil water content derived from the AUV data set as a moisture index. Since unmanned aerial vehicles, lysimeters, and electromagnetic instruments cannot be used over large areas, mapping crop water use under the surveillance of high-resolution sensors integrated with remote sensing techniques will be improved in the future. The accurate and timely monitoring of crop water use will improve agricultural stakeholders' decision-making towards irrigation scheduling and water management while optimising yields.

Keywords: Evapotranspiration; Unmanned Aerial Vehicle (UAV); Smart-Field Weighing Lysimeters (SFL); Electromagnetic Induction (EM38); Soil Water Content; Electrical Conductivity.

DECLARATION

I **Ratshiedana Phathutshedzo Eugene** declare that: Monitoring crop water use using unmanned aerial vehicle (UAV) and surface energy balance algorithms: A case study of Vaalharts Irrigation Scheme, Northern Cape Province, South Africa is my work. All reference sources quoted in support of this research work have been acknowledged in the reference list. This work is being submitted for the Master of Science degree at the University of the Witwatersrand, Johannesburg. It has not been presented anywhere for a degree or examination purposes at any other University.



(Signature of candidate)

08 day of June 2022 at University of the Witwatersrand

DEDICATION

This work is dedicated to my parents, who gave me the support I needed from childhood. To my younger brothers, I dedicate this work to be a form of motivation in academics. This work is also dedicated to all people who guided me and supported me at all times; my hat is off to you all.

ACKNOWLEDGEMENTS

Research objectives are always achieved when people and organisations come together to implement, share techniques and offer support. Several people and organisations were, directly and indirectly, involved in support of this project. Such people and organisations will always be honoured. I thank the following people and institutes:

- Before all, I thank almighty God who gave me the strength, ideas and knowledge, including everyone who was involved through this MSc journey (I bow before you and give thanks).
- Prof Mohamed Abd Elbasit; Prof Elhadi Adam, and Dr George Chirima, my supervisors and my advisor, for your unending guidance, knowledge sharing positive critiques and comments and patience, which are highly appreciated.
- The Agricultural Research Council (ARC)-Institute for Natural Resources and Agricultural Engineering for providing its resources during my fieldwork and laboratory work.
- I appreciate Dr. Nyamugama Adolph for his guidance in writing.
- NRF for providing training and funding to cover the costs for the study.
- SABBI for permitting me to use their experimental farm as my study area.
- AB-InBev for providing research equipment during the project.
- SACNASP and the GSSA for providing mentorship through Regina Molloy.
- I also express my thanks to Mr Eric Benjamin Economon for his assistance during data collection, Mr. Pitso Khoboko, Dr. Wonga Masiza, Mr. Fagan Scheepers, Mr. Willem Vermeulen and Mr. William for their help during instrument installation.
- Lastly but not the least, I appreciate the assistance by Aerial Works through Mr. Bertus van Zyl and Kim James for their UAV field support.

Table of Contents

ABSTRACT i
DECLARATION ii
DEDICATION iii
ACKNOWLEDGEMENTS iv
LIST OF FIGURES viii
LIST OF TABLES xii
LIST OF SYMBOLS AND ABBREVIATIONS xiii
CHAPTER ONE 1
GENERAL INTRODUCTION 1
1.1 Introduction 1
1.2 Problem Statement 2
1.3 Justification 4
1.4 The Aim of the Study 4
1.5 Research Questions 5
1.6 Thesis Outline 5
CHAPTER TWO 6
LITERATURE REVIEW 6
2.1 Evapotranspiration Overview 6
2.2 Evapotranspiration Measurement Approaches 7
2.2.1 Use of field Lysimeters in evapotranspiration estimation 8
2.2.2 Use of meteorological data in evapotranspiration estimation 9
2.2.3 The use of remote sensing models in evapotranspiration estimation 10
2.3 Soil Water Content Estimation for Crop Water use Monitoring 14
2.3.1 Soil water content measurement 15
CHAPTER THREE 20
MATERIALS AND METHODS 20
3.1 Study Area Description 20
3.1.1 Climatic conditions 20
3.1.2 Topography 22
3.1.3 Soils 22
3.1.4 Irrigation systems 22
3.1.5 Farming system 23
3.2 Data Acquisition Methods 23
3.3 Determination of Soil Water Content Distribution at Farm Scale 24

3.3.1 Soil Water Content (SWC) measurements 24
3.3.2 Field Apparent Electrical Conductivity 25
3.3.3 Data transformation and cleaning 26
3.3.4 Calibration of the electromagnetic induction instrument (EM38) 27
3.4 Data Processing and Analysis 28
3.4.1 Spatial distribution of soil properties 28
3.4.2 Conversion from ECa to SWC 28
3.4.3 Data analysis and evaluation 29
3.5 Evapotranspiration Estimation using Smart Weighing Lysimeters 29
3.5.1 Lysimeters installation and data measurements 29
3.5.2 Evapotranspiration Estimation using weighing lysimeters 30
3.5.3 Evaluation and validation of lysimetric evapotranspiration 31
3.6 Evapotranspiration Estimation using Weather Data 32
3.6.1 Validation 37
3.7 Use of Unmanned Aerial Vehicle (UAV) for Aerial Surveys 37
3.7.1 Pre-flight planning 39
3.7.2 Survey sensor types 41
3.7.3 Image processing and ortho-rectification 42
CHAPTER FOUR 47
RESULTS 47
4.1 The Assessment of Soil Water Content using Soil Electrical Conductivity 47
4.1.1 Spatial distribution of electrical conductivity use in determining soil water content 47
Relationship between the soil water content measured and predicted electrical conductivity. 50
Relationship between in-situ soil electrical conductivity and in-situ soil water content. 51
The Relationship between soil electrical conductivity and soil physiochemical properties. 52
4.1.2 Soil electrical conductivity conversion to soil water content 52
4.1.3 The Spatial distribution of soil water content 53
4.2 Irrigation events 56
4.3 Actual Evapotranspiration Estimation from Smart Field Weighing Lysimeters 57
4.4 Reference Evapotranspiration Estimation from weather data 59
4.4.1 Reference evapotranspiration evaluation 60
4.4.2 Comparison between actual evapotranspiration (ETa) and Reference Evapotranspiration (ET_0) 60
4.5 The Capabilities of Unmanned Aerial Vehicle (UAV) Data in Estimation of Evapotranspiration and Soil Water Content 62
CHAPTER FIVE 70
DISCUSSIONS 70

Estimation of soil water content using an electromagnetic induction instrument 70
Evapotranspiration Estimation based on lysimeters 72
Unmanned Aerial Vehicle (UAV) Evapotranspiration and Soil Water Content Estimation 73
CHAPTER SIX 75
CONCLUSIONS, CHALLENGES AND RECOMMENDATIONS 75
REFERENCES 78
APPENDIX 90
Appendix I: Multispectral UAV data processing report (10 August 2020) 90
Appendix II: Multispectral UAV data processing report (22 September 2020) 91
Appendix III: Multispectral UAV data processing report (14 October 2020) 92
Appendix IV: The calibration for the RED and NIR bands based on the calibration panel images 93

LIST OF FIGURES

Figure 2.2: A triangular method scatterplot from remotely sensed Temperature Ts and Vegetation index (Adopted from Zhu *et al*., 2017). 12

Figure 3.1: Showing the study area location within South Africa and its reference province. 20

Figure 3.2: Temperature patterns in Hartswater (Agricultural Research Council, Natural Resources and Agricultural Engineering, Weather station).....21

Figure 3.3: Mean annual rainfall patterns in Hartswater (Agricultural Research Council, Natural Resources and Agricultural Engineering, Weather station).....21

Figure 3.4: General flow diagram illustrating data collection approaches for the study.....24

Figure 3.5: Showing the soil water content measuring probe, the thermal analyzer, a GPS and the surveyor during ground measurements. 25

Figure 3.6: Showing the experimental farm and the area of interest used for the EM38 survey.....26

Figure 3.7: Showing the electromagnetic induction instrument and its components. 26

Figure 3.8: Soil sampling at different depths for EM38 calibration. a) Different layers of soil taken at each calibration point, b) Surveyors taking core samples at different depths equivalent to the EM38 measurement depth.....27

Figure 3.9: Showing the installed lysimeters in the field. 30

Figure 3.10: Showing the schematic overall lysimetric system and its components.....30

Figure 3.11: The top view of the lysimeter and the dimensions.....31

Figure 3.12: Weather station installed north of the lysimeter in the field. 32

Figure 3.13: M600 DJI drone equipped with a multispectral camera. 38

Figure: 3.14: DJI Inspire 1 UAV equipped with a Zenmuse XT thermal camera.....38

Figure 3.15: Flow diagram illustrating the steps necessary to achieve UAV data set.....39

Figure: 3.16: Showing flight lines, height and duration. 41

Figure 3.17: Showing the calibration panel for multispectral radiometric calibration. 43

Figure 3.18: Thermal calibration images were taken using a handheld FLIR thermal camera (A) showing the natural colour of the field while (B) depicts the thermal image of the same field part. 43

Figure: 3.19: Schematic chat illustrating stepwise quantification of evapotranspiration. 46

Figure 4.1: Spatial variability of soil electrical conductivity for four depths (A-D, represent top to bottom layers on 11 August 2020).....48

Figure 4.2: Spatial variability of soil electrical conductivity for four depths (A-D, represent top to bottom layers on 22 September 2020). 48

Figure 4.3: Spatial variability of soil electrical conductivity for four depths (A-D, represent top to bottom layers on 23 September 2020). 49

Figure 4.4: Spatial variability of soil electrical conductivity for four depths (A-D, represent top to bottom layers on 14 October 2020). 49

Figure 4.5: A Relationship between soil electrical conductivity and soil water content where (a to d) represent (11 August 2020; 22 September 2020; 23 September 2020 and 14 October 2020) dates of the survey. 51

Figure 4.6: Pair relationship between in-situ soil electrical conductivity and soil water content at varying soil depths at sampled locations. 52

Figure 4.7: Showing a model used to convert ECa to soil water content (θ). 53

Figure 4.8: Predicted θ at four depths (A-D represents 0.25 m to 1 m on 8 August 2020). ...54

Figure 4.9: Predicted θ at four depths (A-D represents 0.25 m to 1 m on 22 September 2020). 55

Figure 4.10: Predicted θ at four depths (A-D represents 0.25 m to 1 m on 23 September 2020). 55

Figure 4.11: Predicted θ at four depths (A-D represents 0.25 m to 1 m on 14 October 2020). 56

Figure 4.12: Soil water content depicting irrigation occurances. 56

Figure 4.13: Evapotranspiration from lysimeters on the 10th of August 2020. 58

Figure 4.14: Evapotranspiration from lysimeters on the 22 September 2020. 58

Figure 4.15: Evapotranspiration from lysimeters on the 14th of October 2020. 58

Figure 4.16: Reference evapotranspiration estimation using Penman-Monteith (Blue) and Priestly-Taylor (Green) methods between August 2020 and 20 October 2020. 59

Figure 4.17: Relationship between reference evapotranspiration estimated from Penman-Monteith and Priestly-Taylor methods. 60

Figure 4.18: Showing daily evapotranspiration fluxes from lysimeters and weather data. 61

Figure 4.19: The relationship between actual and reference evapotranspiration. 61

Figure 4.20: Showing multispectral composite for different phenological stages, labels (A-C) represent; August, September and October 2020 survey days. 62

Figure 4.21: Normalized Difference Vegetation Index (NDVI) for different phenological stages, labels (A-C) represent; August, September and October 2020 survey days. 63

Figure 4.22: Showing fractional vegetation cover at three phenological stages, labels (A-C) represent; 10 August, 22 September and 14 October 2020 survey days, while D-F represents the same days of the images above them. 64

Figure 4.23: Showing vegetation-temperature relationship derived triangles, labels (A-C) represent; August, September and October 2020 survey days. 65

Figure 4.24: Showing moisture availability at different phenological stages, labels (A-C) represent; August, September and October 2020 survey days. 66

Figure 4.25: Showing evaporative fraction at different phenological stages, labels (A-C) represent; August, September and October 2020 survey days. 66

Figure 4.26: Depicts the correlation between the estimated moisture availability from the UAV-based simulated triangular method and in-situ soil water content measurements, labels (A-C) represent; August, September and October 2020 survey days. 67

LIST OF TABLES

Table 3.1: Flight plan details table for each survey. 39

Table 4.1: Statistical summary for the relationship between the measured soil water content and predicted electrical conductivity. 51

Table 4.2: Correlation matrix of soil physiochemical properties and extractable cations with electrical conductivity ECa and Ece. 52

Table 4.3: Irrigation and EM38 survey date with time included the amount of water irrigated throughout the season. 57

Table 4.4: Statistical relationship between field soil water content and evapotranspiration. .59

LIST OF SYMBOLS AND ABBREVIATIONS

CPR	Calibrated Reflectance Panel
DEM	Digital Elevation Model
DFM	Dirk Friedhelm Mercker
DTD	Dual Temperature Difference Model
DTM	Digital Terrain Model
EC	Electrical Conductivity
ECa	Apparent Electrical Conductivity
ECe	Electrical Conductivity of a saturated paste
EF	Evaporative Fraction
ET	Evapotranspiration
ET_0	Reference evapotranspiration
ETa	Actual Evapotranspiration
ETp	Potential Evapotranspiration
Fr	Fractional Vegetation Cover
GPS	Global Positioning System
Ha	Hacter
Hz	Horizontal Mode
LAI	Leaf Area Index
METRIC	Mapping Evapotranspiration at high resolution with Internalized Calibration
Mo	Moisture Availability
MODIS	Moderate Resolution Imaging Spectro-radiometer
MSI	Multispectral Image
NDVI	Normalized Difference Vegetation Index
NIR	Near-Infrared
RGB	Red-Green-Blue
SAR	Sodium Absorption Ration
SEBAL	Surface Energy Balance Algorithm for Land Surface
SFL	Smart Field Lysimeter
SWC	Soil Water Content
TDR	Time Domain Reflectometry
TIR	Thermal Infrared
TSEB	Two Source Energy Balance Model

UAV	Unmanned Aerial Vehicle
USSR	Union of Soviet Socialist Republics
Vz	Vertical Mode
Θ	Theta (Soil water content)

CHAPTER ONE
GENERAL INTRODUCTION

1.1 Introduction

Water scarcity in arid regions remains a critical challenge as they face crop productions globally, and fewer water resources are available to satisfy the water exploitation requirements (Damkjaer and Taylor, 2017). Nowadays, the scarcity of water continues to intensify due to severe droughts, rising temperatures, increased evaporation, salinity challenges, degradation of agricultural soils and temporal variability in rainfall patterns (Javadinejad *et al*., 2019; Corwin, 2021). Although various factors contribute to water scarcity, rising populations continue to pressure the available water resources (Salamé *et al*., 2021). An increase in population consequently leads to increased demands for food production to meet population feed demands, as well as equally facing the pressure faced in water resources to meet food and fibre requirements. Therefore, more water is demanded for other domestic and industrial uses to satisfy rising populations. Any increase in population causes a high increase in demand of water resources with a high reduction in water availability if it is not matched by frequent precipitation to replenish the insufficient water supply. Changes in climate conditions influenced by deforestation, increased industrialization, food production, transportation, and power generations pose threats to future water availability (Maliva, 2021; Peng *et al*., 2021). Moreover, weather conditions vary due to climate changes, causing increased heat waves, freezing winters, insufficient rainfall and increased evapotranspiration fluxes (Trenberth, 2011; Guion *et al*., 2021). These conditions reduce surface and ground water when rivers stop flowing and groundwater levels drop.

Globally, three percent of the global water supply comes from freshwater resources, of which only 0.5 percent is accessible for use, about 70 percent of from the accessible water is utilised on irrigation (Fischer *et al*., 2007). The fact that agricultural activities utalizes about 70 percent of freshwater resources of the accessible water resources, there is a need to accurately and continuously monitor crop water usage. Accurate crop water usage data is critical for water management planners and managers for decision making towards water use sustainability. There is an increasing demand in crop water use monitoring techniques and methods, for accurate information on water use for better planning and decision making (Evans and Sadler, 2008). However, more technical approaches are required to accurately quantify the amount of water used by crops post irrigation. Nowadays, farmers focus on

precision agricultural practices to improve their production and easy management of farm resources. Among many techniques, monitoring crop water usage has been achieved by using soil moisture sensors, tensiometers, lysimeters, weather stations not excluding satellite remote sensing techniques (Inman-Bamber and McGlinchey, 2003; Williams and Ayars, 2005). For the agricultural lands, the use of water in a sustainable way remains a priority and requires appropriate technologies in planning, use monitoring, conserving water, environmental impact assessment and handling economic viability concerns (Prinz and Singh, 2000). Besides the significance of water in the agricultural environment, water resources drive all forms of life, which is the main reason it should be sustainably utilized and managed; without water availability, there is no balance in the hydrological cycle which consequently affects the entire ecosystem (Pereira *et al*., 2002).

Sovoe (2011) stated that the development and increase of irrigation croplands demands good knowledge about the spatial extent of different crop types, evapotranspiration patterns, water demand, and local hydrology. Remote sensing technology offers the opportunity to map and monitor different crop types during their phenological stages as well as factors affecting their productivity (Mutanga *et al.*, 2017). The use of satellite-derived vegetation indices which include the normalized difference index (NDVI), the soil adjusted vegetation index (SAVI), normalized difference water index (NDWI) and other indices permits remote sensors to understand the water and health status of crops at different stages (Mokhtari *et al*., 2019). Although satellites provide an option, the use of unmanned aerial vehicles gives very reliable and high-resolution information regarding various environmental components.

Irrigation in arid areas alleviates poverty by ensuring food security when there is no sufficient rainfall for better yields. Besides food security, irrigated farms provide many households with employment which makes-up most of their incomes (Masasi and Ng'ombe, 2019). Declines in water resources cause water rates to increase, which negatively affects food production when the input requirements budget is altered, causing production expenses and food prices to rise to meet their production costs.

1.2 Problem Statement

The Vaalharts irrigation scheme was developed to alleviate poverty and increase food security among the small communities from Jan-kempdorp through Hartswater to Taung (Kruger *et al*., 2009). The scheme utilizes fresh water quantities from the Vaal and the Harts Rivers. Salinity within the area prevents farmers from using groundwater for irrigation

(Herold and Bailey, 1996; Verwey and Vermeulen, 2011)**.** Therefore, high volumes of water are being used for irrigation within the area, in competition with other water uses (Arp et al., 2017). Although the Vaalharts irrigation scheme gets water from two rivers, the overuse negatively affects the two rivers by reducing water downstream, leading to sedimentation, contaminant accumulations, and salinity problems (Braune and Roger, 1987; Grobler et al., 1987; Le Roux et al., 2007). The reduction in water quantity also leads to ecological damage wherein wetland ecosystems, peat lands and flood forest ecosystems are lost. Fishing opportunities are also affected by water reduction downstream because weirs are constructed to cater to irrigation. The Vaal River supplies most parts of South Africa; as such, the overuse of water from this resource will lead to future irrigation and water availability challenges. However, farmers know the amount of water they supplement their crops with, mostly in pivot controlled irrigation. Knowledge about how much water their crops use and or lose through infiltration and evapotranspiration remains inadequate. The amount of soil water content available at varying depths for root development and nutrients transfer in the soil remains a challenge. Consequently, more or less water is given to crops. Farmers usually rely on traditional methods to assess the health status of their crops, which generally involves guesswork derived from visual observations. As a result, they miss the critical factors that affect their crop growth and yields, including evapotranspiration and soil water content, which cannot be visually observed. The temporal and spatial distribution of evapotranspiration and soil water content in irrigated crops is critical for water resource management, decision-making and planning (Anderson et al., 2012). In the previous years, most researchers have explored and applied remote sensing technology using different satellite sensors to estimate evapotranspiration, soil water content and crop water use (Calera *et al*., 2017; Singels *et al.*, 2018; Ellsäßer *et al.*, 2020; Bawa *et al*., 2021). The limitations of the satellite based-approach in monitoring crops water use are the cloud cover and other sky conditions and the spatial and temporal resolutions (Lei *et al.*, 2018; Nhamo *et al.*, 2020). The availability of unmanned aerial vehicles (UAV) provides the opportunity to overcome the limitations of the satellites based-approach in estimating crops evapotranspiration and soil water content at high resolution and without the interference of cloud cover (Acharya et al., 2021). However, the drawback of unmanned vehicles is that they are costly and limited to small area coverage and specific weather conditions. To solve problems experienced when using unmanned aerial vehicle platforms, ground-based monitoring instrumentation such as lysimeters, weather stations, electromagnetic sensors, handheld thermal sensors, and moisture sensors integrated with energy balance models can improve the accuracy of measurement

estimations. However, the issue of spatial resolution can only be solved by satellite integrated remote sensing using high-resolution satellite imageries, although they are costly.

1.3 Justification

Water is becoming scarce in most South African parts as the increasing population demands and competition for use increases. It is unquestionably necessary to monitor and implement conservation management strategies towards sustainable water use. To achieve that, there is a need to understand how water is being used and the hydrological cycle components, especially in irrigated croplands, where water is highly used. The use of remote sensing technology provides a fast and accurate way for crop monitoring and estimation of different factors affecting the development of crops during different phenological stages; this includes the estimation of soil moisture, evapotranspiration, yields and water demand in irrigated croplands. The use of remote sensing technology provides a better approach to decision-making and planning for resource use, management and sustainability. In this study, high-resolution imageries obtained from unmanned aerial vehicles combined with ground measurements and surveys will be used instead of using satellite data. This data combination assesses water use in irrigated crop areas to close yield gaps, simultaneously conserving water and achieving water use sustainability. The UAV remote sensing technology can detect in-season variability of crop water use combined with other measurements. Although satellite imageries can do the same, the problem with satellites is that free satellite imageries have a coarse resolution. High-resolution satellite imageries obtained from commercial satellites, on the other hand, are very expensive to use for the entire cropping season. Replacing satellite technology with an aerial survey using human-crewed aircraft, on the other hand, is challenging since aircraft are also very expensive to use for surveying and data processing. Although UAV's can map at high resolution; they can map almost every day while satellites have overpass days which might not align well with planned ground field surveys preferred by the farmer. UAV's fly below clouds, thus eliminating the effects of clouds on imageries.

1.4 The Aim of the Study

The main aim of this study is to utilize unmanned aerial vehicles data and field-based data to estimate and monitor crop water use under an irrigated system. The specific objectives of the study are to:

i. Assess the variability of soil water content within the irrigated study area.
ii. Assess the variation of evapotranspiration using smart field Lysimeters.

iii. To test the capability of unmanned aerial vehicle (UAV) data in estimating evapotranspiration compared to ground observation.

1.5 Research Questions

i. How will soil water content variability be assessed within the study area?
ii. How will the smart field Lysimeters be used to estimate the actual crop evapotranspiration at the field scale?
iii. What is the performance or visibility level of an unmanned aerial vehicle in the estimation of crop evapotranspiration?

1.6 Thesis Outline

Chapter one provides a general introduction to the research. This includes an overview of the water issue in the arid environments, emphasising crops water use, water scarcity, population growth, and increased food demand. The chapter also highlights the specific research problem in the South African context, the research aims and objectives of the study.

Chapter two reviews the literature and defines the concepts around crop water use. Different methods of crop water use estimating are reviewed, with a particular focus on local and existing South African literature, demonstrating research gaps.

Chapter three is the research methodology chapter, which provides information about the study area location, climatic conditions, topography, flying restrictions, water resources and rainfall history. Data application methods, which range from using ground measuring devices for soil water content, electrical conductivity, weather data, evapotranspiration and aerial devices for aerial images with their processing techniques, are shown in chapter three. The chapter explains the use of smart field weighing lysimeters, automatic weather stations, electromagnetic instrument (EM38), handheld thermal sensors (Thermal, Moisture, temperature and Electrical conductivity) and unmanned aerial vehicle platforms.

Chapter four provides comprehensive results from the collected data.

Chapter five of the study briefly discusses the results on evapotranspiration, soil water content from weather data, smart field lysimeters, in-situ data, and unmanned aerial vehicles relating to different crop developmental stages.

Chapter six provides conclusions, challenges experienced and recommendations for future studies.

CHAPTER TWO
LITERATURE REVIEW

2.1 Evapotranspiration Overview

The concept of evapotranspiration has been clarified as a transfer of water content from different sources on land as evaporation combined with water from plants' leaves as transpiration into the surrounding atmosphere (Verstraeten *et al.,* 2008). This phenomenon can be further defined under three categories, namely, Potential evapotranspiration, Actual evapotranspiration and Reference evapotranspiration. The potential evapotranspiration is defined by Irmak and Haman (2003) as the evaporation of water from extended surfaces of a short green crop that covers the ground but cannot resist water flow and is always water supplied. Such evapotranspiration cannot exceed free water body evaporation, even under the same weather conditions.

On the other hand, the actual evapotranspiration is the quantity of water used by a surface vegetated extensively by a crop within an active growth stage, and its canopy covers the soil surface (Bhatt and Hossain, 2019). Lastly, the term reference evapotranspiration was introduced to clarify the short green crop on the potential evapotranspiration definition (Irmak and Haman, 2003). Allen *et al*. (1998) defined the reference evapotranspiration as the evapotranspiration estimated from a reference hypothetical crop surface with a crop height of 0.12 m, 70 ms-1 surface resistance with an albedo reading of 0.23. Reference evapotranspiration indicates the actual evapotranspiration's upper limit and the total amount of energy available in an arid or humid environment (Gong *et al*., 2006). Reference evapotranspiration has been used to estimate actual evapotranspiration by multiplication of ET_0 with soil and crop coefficients (Allen *et al.*, 1998).

Several factors drive evapotranspiration; such factors include wind speed, air temperature, soil water content, air humidity and radiation (Allen *et al*., 1998). Evapotranspiration increases during the daytime when there is high solar radiation and low moisture (Gaastra, 1959; Li *et al*., 2012; Marques *et al*., 2020). It is, however, critical to understand the concept of evapotranspiration as the crucial component of the hydrological cycle contributing to about 10 percept of the total atmospheric moisture responsible for cloud formation. Otherwise; without evapotranspiration, no precipitation would happen to lead to vegetation water stress conditions (Bhatt and Hossain, 2019).

However, arid areas are dominantly characterized by the highest potential evapotranspiration readings, which exceed the total amount of rainfall received annually. At the same time, much of the rainfall gets evaporated back into the atmosphere before reaching the ground (Lehmann *et al*., 2019). In such areas with low rainfall, it is essential to quantify evapotranspiration fluxes for water management, planning and sustainable use of water resources to maintain the ecological balance (Irmak and Haman, 2003; Wang *et al.*, 2009).

Traditionally, crop water requirement has been assessed through the crop leaves wilting and darkening. Among others, the consequence is that when signs and symptoms show that the overall crop productivity is reduced by delayed crop growth (Marques *et al*., 2020). Until canopy closure occurs, evapotranspiration increases when there is growth in the leaf area index (LAI) (Kergoat *et al.*, 2002). The uptake of water and available nutrients by plants occurs when the stomata open and close, depending on the number of roots and their distribution within the soil (Scott and Biederman, 2017). When the plant roots cannot take more water, they close the stomata and any excess water given to the plant is not used by the plant but rather infiltrates the soil, thus contributing to groundwater or evaporates simultaneously with plant transpiration leading to evapotranspiration (ET) (Irmak *et al.*, 2013). In precision agriculture, quantification of evapotranspiration plays a crucial role in crop irrigation scheduling, planning and management (Mukherjee *et al.*, 2010).

2.2 Evapotranspiration Measurement Approaches

Measurement of evapotranspiration can be made from a leaf scale, plant scale, field-scale to regional scales, depending on the platforms used (Gentine *et al.*, 2016). Various instruments such as weather stations, field lysimeters, eddy covariance, satellite data and handheld equipment have been used over the years (Gentine *et al.*, 2016; Moorhead *et al.*, 2017: Hashem *et al.*, 2020). For regional and global scales, earth observation technologies, which include remote sensing models, are the most affordable and suitable approaches that can be used to cover the gap in the spatial extent of estimations made by ground-based instruments (Carlson and Buffum, 1989; Carlson *et al.*, 1994; Granger, 2000; Moran *et al.*, 2000; Carlson, 2007).

This study focuses on the use of advanced smart field weighing lysimeters that are recently new in the advancement of lysimeters, the use of automatic weather station data, and

unmanned aerial vehicles, which is also a recent development in agricultural field estimate evapotranspiration.

2.2.1 Use of field Lysimeters in evapotranspiration estimation

Field lysimeters are devices that contain core like columns containing undisturbed soil samples and vegetation, representing a particular field that measures the evapotranspiration of the vegetation contained (Meissner *et al.,* 2010). Depending on the use, lysimeters can be classified as weighable, groundwater lysimeters, non-weighable, large lysimeters with big chambers and monolithic lysimeters (Amankwah, 2007). Lysimeters were designed to measure the leachate in the soil, which changed when years changed, and they have been applied in hydrogeology, hydrology, ecology, the economics of water and crop water balance studies (Toth *et al.,*1998; Kutilek and Neilsen, 1994). According to BBA (1990), field lysimeters in Germany were used to aid in local authorities' decision-making as a tool to identify vulnerable areas where monitoring is demanded and where the need to protect water resources was a need in pesticide testing. Lysimeters can estimate evapotranspiration at a high temporal resolution that can be computed every minute, hourly, daily and monthly; compared to other products such as MODIS data with course temporal resolutions of eight to ten days (McNally, 2016). According to Makkink (1959), lysimeters are expensive devices; they cover small areas, and their maintenance is time-consuming, resulting in data gaps.

Researchers have been using lysimeters with their various improvements, to understand evapotranspiration fluxes for crop water use management over decades (Hutson *et al*., 1980; Berliner and Oosterhuis, 1987; Gebler *et al*., 2015). The use of weighing lysimeters in South Africa was first conducted by Hutson *et al*. (1980) in Roodeplaat to investigate crop evapotranspiration. They used three lysimeters with a square design to fit in row cropping. Their daily evapotranspiration ranged between 0 mm and 120 mm, with high evapotranspiration being observed during rain and irrigation days. Their investigation continued for two years, leading them to conclude that lysimeters are accurate and reliable for evapotranspiration estimation. They further suggested improvements in the lysimeter systems to enhance the understanding of interaction between water, soil, crops, and the atmosphere.

Berliner and Oosterhuis (1987) used two field plots set under different conditions to install lysimeters in an attempt to test the representativeness of the lysimeter in crop water stress determination. One lysimeter was well irrigated while the other was left in a dry condition.

They planted winter wheat in each lysimeter and monitored evapotranspiration, soil water content and canopy temperature to determine water stress conditions. They monitored crop water stress by assessing the leaf water potential in each lysimeter. Changes in evapotranspiration were observed with changes in soil water content, with higher evapotranspiration being observed in dryer conditions. They concluded that crop water stress could be determined using lysimeters in plots representing prevailing field conditions. They mentioned that conclusions on the relationship between canopy conditions and soil conditions influence on water stress could not be made. Gebler *et al*., 2015 investigated the use of lysimeters in actual evapotranspiration and precipitation, compared with Eddy Covariance and tipping bucket in Germany Rollesbroich. Six weighing lysimeters were used to estimate evapotranspiration. The Eddy Covariance and Penman-monteith methods were used to estimate the actual and the reference evapotranspiration. They reported that comparisons between eddy covariance and lysimeters are limited in the literature. They obtained their hourly evapotranspiration ranging between 0 mm and 0.5 mm for the lysimeters, eddy covariance and the Penman-monteith method. They concluded that the evaluation of the two methods showed good agreement with a slight difference.

2.2.2 Use of meteorological data in evapotranspiration estimation

Estimating evapotranspiration using weather data commonly uses energy balance equations, such as the Penman-Monteith method, the Priestly-Taylor method and the Makkink method (Wang *et al*., 2014; Doležal *et al*., 2018). The Penman-Monteith and Priestly-Taylor methods are very similar to the parameters used in computing reference evapotranspiration with the difference in albedo, which in Penman-Monteith is 0.23 and 1.26 in the Priestly-Taylor method (Allen *et al*., 1998; Zotarelli *et al*., 2010; Doležal *et al*., 2018). The advantage of using weather data in estimating evapotranspiration is that the climatic conditions of an area are considered while the spatial resolution and maintenance cost remains a setback (Allen *et al*., 1998). Using the Penman-Monteith equation under the food and agricultural organisation (FAO-56), ET_0 can be calculated using the equation as follows:

$$ET_0 = \frac{0.408\Delta(R_n - G) + \gamma(C_n/(T + 273))U_2(e_s - e_a)}{[\Delta + \gamma(1 + C_d U_2)]} \qquad (2.1)$$

ET_0 denotes the standardized reference ET (mm d-1 or mm h^{-1}), Δ representing the slope of saturation vapour pressure against air temperature (kPa°C^{-1}). Rn being the total or net radiation on the surface of a crop under investigation (MJ m^{-2} d^{-1} for 24-hours' time), G

denotes the heat flux density at the soil surface (for 24-hours' time steps). T is the average daily air temperature per hour (°C), and U_2 is the mean hourly wind speed measured at a 2 m height (ms^{-1}). e_s denotes saturation vapour pressure (kP_a), e_a is the actual vapour pressure (kPa), e_s - e_a saturation vapour pressure deficit (kPa). γ is the psychrometric constant (kPa °C^{-1}), C_n is the numerator constant that changes with the reference surface, and C_d is the denominator constant that changes with the reference surface (Carlson and Buffum, 1989; Allen *et al.,* 1998; Alavi and Rahimikhoob, 2016).

2.2.3 The use of remote sensing models in evapotranspiration estimation

Estimation of evapotranspiration, especially for regional and global scales, has been achieved through the use of satellite, unmanned aerial vehicle (UAV) sensors and remote sensing models as a surrogate of direct measurements, which are expensive and tedious (Rauneker and Lischeid, 2012; Ortega-Farías *et al.,* 2015; Aboutalebi *et al.,* 2020). Several surface energy balance models used in the estimation of evapotranspiration which includes two-source energy balance model (TSEB), dual temperature difference model (DTD), surface energy balance algorithm for land model (SEBAL) and the METRIC model exist (Wolff *et al.,* 2016; Cavalcante *et al.,* 2016). All models use the surface energy equation to estimate evapotranspiration as the residual given as:

$$\mathrm{Rn} = \mathrm{LE} + \mathrm{G} + \mathrm{HE} \qquad (2.2)$$

Where Rn is the net radiation in ($W.m^{-2}$), LE is the latent heat which is consumed during evapotranspiration in ($W.m^{-2}$). G is the ground flux conducted into the ground in ($W.m^{-2}$) which is negligible in cases of dense canopy cover, and HE is the sensible heat that is converted to the atmosphere in ($W.m^{-2}$) (Bastiaanssen *et al.,* 1998).

Two-Source Energy Balance model (TSEB)

TSEB model was created in the mid-90s by a team of researchers to estimate evapotranspiration as the residual (Norman *et al.,* 2000). The model has been declared to work effectively in homogeneous land conditions (Elfarkh *et al.,* 2020). The TSEB model separates land surface into vegetation surface temperature and soil surface temperature, wherein the sensible heat and latent heat are transferred back into the atmosphere; Xia *et al.* (2016) later improved the Priestley-Taylor model.

Dual Temperature Difference (DTD) model

The DTD model is similar to the TSEB model in the way they both separate land surface temperatures into vegetation surface temperature and soil surface temperature. However; the model varies from TSEB because it adds one more input, which is the use of land surface temperature obtained just after sunrise to account for energy fluxes and bias, since fluxes are minimal after sunrise (Norman *et al.,* 2000). Norman and his team created the model in the early 2000s.

Surface Energy Balance Algorithm for Land model

Surface Energy Balance Algorithm for Land (SEBAL) uses the energy balance principles to predict hydrological features such as evapotranspiration and water deficit; Professor Bastiaanssen created the model in the late ’90s (Bastiaanssen *et al.,* 1998). The model has been validated under several conditions for different locations (Bastiaanssen, 2000; Allen *et al.,* 2002; Santos *et al.,* 2010; Sun *et al.,* 2011; Ruhoff *et al.,* 2012; Singh and Senay, 2016). SEBAL model uses a set of mathematical equations and meteorological data, including atmospheric corrections, surface albedo, net radiation, surface temperature, vegetation index and heat flux to estimate evapotranspiration per pixel in a given area.

The METRIC model

The METRIC model is a popular energy balance model used to estimate evapotranspiration; the model was built by the University of Idaho (Morse *et al.,* 2004). The model has the self-calibration process, which involves ground reference evapotranspiration hourly (Gowda *et al.,* 2008). The METRIC model is based on the SEBAL model, which uses a near-surface temperature gradient. At the same time, it requires no computation of aerodynamic surface temperature; it does not regard sensible heat flux as zero and it selects the cold pixel in the agricultural setting rather than using biophysical factors. It uses a standardized Penman-Monteith equation to estimate evapotranspiration.

The Triangular Method

The triangular model makes use of two components, namely, the Normalized Vegetation Index (NDVI) and the radiant surface temperature (Tir), from which other parameters for determining evapotranspiration fractions are derived (Carlson, 2007). The NDVI is partitioned into NDVIs, which denotes the portion of an image covered by dense vegetation and NDVIo, which indicates bare soil surfaces. Surface radiant temperature is scaled between

0 and 1 with temperatures close to zero representing wet area or densely vegetated portions, while temperatures close to one represent surfaces that are dry and covered only with bare soil (Yang et al., 2008; Minacapilli et al., 2016; Fuzzo and Rocha, 2018; Carlson, 2020). According to Carlson and Ripley (1997), scaling radiant surface temperature helps isolate cloud-covered pixels outside the triangle, allowing the comparison of pixels within one framework. From NDVI computations, fractional vegetation cover can be computed. Plotting the vegetation index against radiant temperature results in triangular pixels where generation model inputs are derived, as shown in Figure (2.2) below. Low temperatures are associated with wet surfaces, while high temperatures are associated with dry surfaces (Zhu *et al.,* 2017; Carlson, 2020). The model derives soil moisture availability (Mo), defined as the ratio of evapotranspiration to the potential evaporation at radiant soil temperatures given at a particular time (Zhao and Liu, 2014). Evapotranspiration fraction is the ratio of LE/Rn, where LE is the surface ET which is the total of vegetation and evapotranspiration, and Rn is the surface net radiation (Carlson and Pertropoulos, 2019).

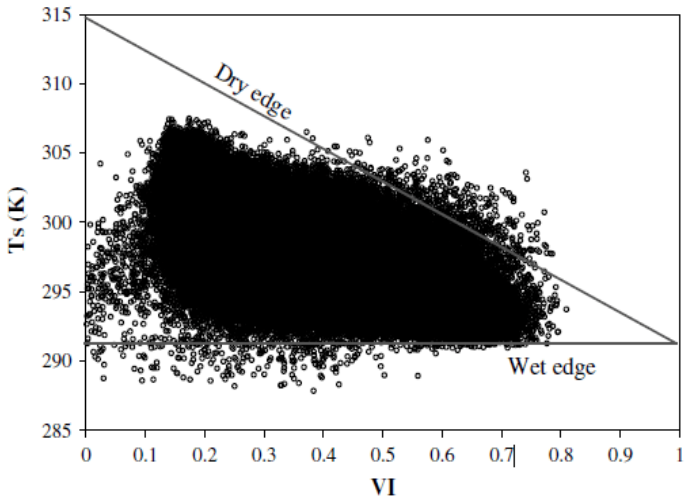

Figure 2.2: A triangular method scatterplot from remotely sensed Temperature Ts and Vegetation index (Adopted from Zhu *et al*., 2017).

Globally, remote sensing approaches integrated with surface energy models have been applied in different studies to estimate variations in evapotranspiration (Mkhwanazi, 2014; Ellsäßer et al., 2020; Elkatoury et al., 2020; Ghaderi et al., 2020). Ellsäßer *et al.* (2020) conducted a study to estimate evapotranspiration in a tropical oil palm plantation using three energy balance models: Two-Source Energy Balance- Priestley-Taylor (TSEB-PT), Dual Time Difference (DTD) and Deriving Atmosphere Turbulent Transport Useful To Dummies Using Temperature (DATTUTDUT). They used an octocopter drone mounted with thermal and RGB cameras to obtain a set of imageries for their study. They used individual images

instead of doing the normal stitching and mosaicking of imageries. Their studies measured land surface temperatures using a fixed emissivity of one of the models used. Following various models, they used an eddy covariance instrument for their measurements validation. They applied regression methods in x and y variables to establish the coefficients of determination (R^2), Root Mean Square Error (RMSE) and the Mean Absolute Error (MAE) of their findings. They found that TSEB-PT model works better than the other models they used.

Mkhwanazi (2014) conducted a study in south-eastern Colorado near the Rocky Ford using SEBAL and the METRIC models to evaluate their evapotranspiration mapping. SEBAL performed well in the estimation of advection and evapotranspiration. Elkatoury *et al.* (2020) conducted a study to quantify evapotranspiration using three surface energy balance algorithms: SEBAL, METRIC and S-SEBI in the Saudi Arabia agricultural area. They compared their findings with ground measured evapotranspiration using an Eddy covariance (EC) device. On their results, SEBAL rated second after the METRIC model as best for modelling evapotranspiration for arid areas. There were fluctuations in evapotranspiration measured by the models, compared to eddy covariance device. Their findings were further compared with Lysimeter data, where the agreement between the methods used was high.

Zhao and Liu (2014) investigated the triangular approach to understand the influence of topography on evapotranspiration. They used MODIS data to model their triangles, including the temperature and vegetation derived index. Their model requirements for the triangular method stated that a flat surface is required but they should rather focus on the mountainous area to do their investigations. They applied topographic corrections to their data and estimated evapotranspiration of the area, which they compared with the findings of the uncorrected data, which yielded no greater difference. They concluded and recommended that there is no greater difference in corrected data; satellite data can be used without being corrected for the effects of topography for evapotranspiration estimations.

Du *et al*., (2016) also used the triangular method, comparing two methods for temperature vegetation dryness as part of drought monitoring. They also used MODIS data as Zhao and Liu (2014) used. Based on the triangular results, they were able to detect areas that are arid and areas that are humid. They validated their findings using in-situ ground measurement of meteorological information. They concluded that the triangular method has the potential to monitor drought. Fuzzo and Rocha (2018) used MODIS 1 km resolution data to simplify the triangular method for estimating evapotranspiration. They also focused on a regional scale to

do their investigations. They observed that the warm edges of the triangles represent a drying out of the land surface while the cold edge represents the wet or moist land surface. An increase in NDVI causes a decrease in temperature due to shading. They concluded that the triangular method could be used as a substitute for ground-based agro-meteorological instrumentations. Except for the study by Ellsäßer *et al.* (2020), the above studies focused mainly on satellite retrieved data to estimate evapotranspiration, with an emphasis on the problems of resolutions and revisit times; but high-resolution images were lacking.

In South Africa, several studies dominantly applied the SEBAL model among other models to estimate evapotranspiration in agricultural lands at different scales (Kongo and Jewitt, 2006; Ndou *et al.*, 2018; Singels *et al.*, 2018). Kongo and Jewitt (2006) used the SEBAL model to monitor the hydrology of a catchment with the response to the water use innovations in agriculture. The SEBAL results were compared with the weather station data for evapotranspiration. They found that the results differed between the evapotranspiration produced by SEBAL and those of the weather station. Although the differences exist, SEBAL potential in mapping evapotranspiration was realized.

Ndou *et al.* (2018) compared the SEBAL model and groundwater levels monitoring to establish the relationship between the water table and spatial variation in evapotranspiration. The study demonstrated that the SEBAL method could map variations in evapotranspiration over time and space, wherein fluctuations in evapotranspiration were noted as fluctuations in the water table for groundwater. Singels *et al.* (2018) undertook a study in Mpumalanga sugarcane farms to assess the capability of remote sensing technology in the estimation of evapotranspiration; comparing it to the surface renewal system on a field. On their findings, the SEBAL method estimated evapotranspiration as being 5 mm per week greater than the surface renewal system. However, despite a slight difference, they regarded SEBAL and surface renewal system results as reliable.

2.3 Soil Water Content Estimation for Crop Water use Monitoring

Soil water content is a crucial component of the hydrological cycle which plays a huge role in crop development and growth (Dorigo *et al.*, 2017). The amount of water available in soil enables the movement of essential nutrients, usually on the planted field's upper surface, downwards through dissolution and seepage (Robock *et al.*, 2000; Andresen *et al.*, 2020). The soil water availability near the earth's surface drives the distribution of the energy

available to exchange latent and sensible heat with the surrounding atmosphere, connecting energy balance and water through temperature and moisture content (Lei *et al.,* 2018). Soil water content can be defined using various units with the well-known volumetric (W), which is plant-available or as the total volumetric soil moisture content (WT), which is given as the water column depth or as volumetric water percentage for a given soil depth (Robock *et al.,* 2000). Soil water content is governed by soil porosity, the total number of pores available in a given soil sample that water, or air can fill. The more pores, the higher the porosity of a medium is (Zwieback *et al.,* 2019). Supposing that the number of pores is filled by water in a soil medium, the sample then becomes saturated, and no more water can percolate through, which is usually evident by water logging conditions on the surface of the earth (Belcaid *et al.,* 2020). In cases where vegetation extracts as much water as possible from the saturated soil until it wilts, the soil's remaining moisture is referred to as the wilting level, and the remaining water content is not available for plant use anymore (Robock *et al.,* 2000).

2.3.1 Soil water content measurement

Depending on the method applied, soil moisture measurements can be gravimetric or volumetric. Gravimetric soil moisture focuses on the principle of sampling soil at various depths, using a core or an auger up to 1.5 m deep and then taking them to a laboratory where they are weighed for a wet sample mass, dried then weighed again for a dry sample mass. The mass difference then yields the total moisture in the soil sample which is further converted to volumetric units using soil density (Robock *et al.,* 2000; Evett *et al.,* 2008; Datta *et al.,* 2018). The limitation of this standard form of obtaining soil water content is that measurement at the same sampled location is not possible since the homogeneity of the soil is changed immediately when a sample is taken, the method is therefore not suitable for measurement variability with the time of the same environment (Evett *et al.,* 2008).

Recently, sensors to measure water content have been applied in research as an alternative (Evett *et al.,* 2008). Most of the alternative ways of determining soil water content do not directly measure volumetric water content, but rather measure a different parameter which can be related to soil water content which alternates when water content changes in time and space, which is then referred to as a surrogate (Evett *et al.,* 2008). Soil water content increases when precipitation changes, and evapotranspiration increases when soil water content increases; such relationships can be used to obtain one variable from another (Wang *et al.,* 2018). Getting the volumetric soil water content using a surrogate requires estimating

soil water content using a calibration method, thus establishing a relationship between the soil water content and the surrogate, which can be expressed graphically mainly in a linear relationship (Little *et al.,* 1998; Evett *et al.,* 2008). Through the use of sensors and receivers, studies have been undertaken to obtain soil properties which include: salinity, texture, soil and water content (Topp *et al.,* 1980).

Using soil moisture probes such as the neutron probe is one way to obtain soil moisture measurements without taking destructive soil samples from the field. The probe has the flexibility to use and measure accurately, taking real-time measurements (Robock *et al.,* 2000). The disadvantage of neutron probes is the requirement for calibration, especially in varying soil types to each type of soil and different zones with time (Kramer *et al.,* 2018).

Other ways of measuring soil moisture include heat dissipation sensors, frequency domain, and time-domain sensors that measure volumetric water content (Sudduth, 1999). TDR probes have the capability of measuring soil water content and apparent electrical conductivity. It was used in the 1980s to measure soil water content (Sudduth, 1999; Eigenberg *et al.,* 2002). TDR makes use of the voltage-time travelling through the soil medium and back as a function of dielectric constant. TDR at the same time measures apparent electrical conductivity (ECa) as a result of applied voltage signal through the soil (Corwin and Plant, 2005). Heat dissipation sensors records show soil moisture measurements by recording the heat pulse changes (Zhang *et al.,* 2019). A ceramic block in the sensor is heated depending on the ability of soil to dissipate heat, which relates to the content of soil moisture. In this kind of sensor, the rate of heating must be calibrated (Zhang *et al.,* 2019). The measurements can be taken every 30 minutes (Zhang *et al.,* 2019). Frequency and time domain soil moisture sensors generate measurements of soil moisture depending on the dielectric properties of the soil (Zhu *et al.,* 2019). The limitation to this is the depth covered during measurement.

Using electrical conductivity to measure soil water content using the EM38 conductivity relationship with water content is a mostly applied method in estimating soil water content with zero disturbances to soils and crops (Hedley and Yule, 2009; Robinson *et al.,* 2010). Devices such as EM38 have come a long way in the history of being used to estimate soil water content by measuring apparent electrical conductivity (ECa) and relating it to soil water content through calibration methods (Sudduth, 1999; Eigenberg *et al.,* 2002; Corwin and Plant, 2005). Through electromagnetic induction instruments, the electrical conductivity in

soils is a function of the soil moisture or water content available to move the cations available to conduct electrical current (Sudduth, 1999). The instrument does not disturb the soil and goes over 1 meter in-depth, while the limitations are that it works between -40°C to 50°C, thus incurring expensive maintenance and cost; and surveying can be time-consuming. When water enters the soil as recharge, it changes the soil properties' structure, including removing soluble chemicals such as salts and storing them elsewhere through discharge, seepage, or precipitate. Wet soil causes the readings of ECa to be high, whereas soil that is too dry will also affect the ECa readings below as the flow of electrical current stops (Kitchen *et al.,* 1999).

Electrical conductivity can be linked with soil properties that affect the growth and yields of crops, such as pH and water holding capacity. For that reason, farmers doing precision farming usually conduct EC assessments in soils as one of the cheapest measurements they can do to understand their farm soil conditions (Grisso *et al.,* 2009). Although EC varies with the temperature and moisture content availability in soils, different soil types have different conductivities, depending on vegetation cover. The clay soils have the highest electrical conductivities compared to the silts soils, which have a medium conductivity and low EC in the condition of sandy soils (Grisso *et al.,* 2009).

Stanley *et al.* (2014) conducted a study to assess the apparent electrical conductivity (ECa) capabilities to replace neutron probe counts to measure soil moisture content in clay soils in Australia. They reported a very strong correlation between ECa and soil water content when they compared readings for samples taken within the EM38 survey interpolated map. ECa increased with wetting during irrigation from their findings. They also reported that the number of sample points available could affect ECa conversion to any other soil attribute.

Costa *et al.* (2014) conducted a study wherein the apparent electrical conductivity was used to map the spatial distribution of soil moisture and other soil properties that relate to it. They made use of Land Mapper ERM 02 to acquire the apparent electrical conductivity readings around the field. The system used four electrodes configured in the Wenner array configuration to measure the resistivity in soil and convert it to conductance. To measure soil moisture, they collected soil samples during the electrical conductivity surveying and used them to establish gravimetric soil moisture, excluding volumetric soil moisture. They made lab analyses for the samples' calcium, magnesium, phosphorus, potassium, and soil pH. They

used statistical analysis for their set of data and found a high correlation between mean electrical conductivity and mean soil moisture determined for each survey date.

Sudduth *et al.* (2005) used Veris 3100 and EM38 to assess the relationship between soil electrical conductivity and other soil properties. They paired electrical conductivity values obtained at the exact geographic location by EM38 with those of Veris 3100. Soil samples were collected at different depths for calibration. Their findings showed a very low correlation between electrical conductivity and soil properties' results of calibration, which they assumed was due to fewer samples. Consequently, they conducted a non-spatial analysis between electrical conductivity and soil properties using regressions, achieving a statistically significant ($p<0.05$). They made conclusions that for the entire study, the apparent electrical conductivity correlation to most soil properties was low except for clay content since it can store water better than other soils.

Martinez *et al.* (2018) recently evaluated the variability of soil moisture and electrical conductivity within the olive field to implement a better irrigation management strategy. They used a DUALEM-21 sensor for electrical conductivity determination and soil moisture with sensors at opposite directions of the tree trunk to avoid signal interference. Their study found a highly significant correlation of (0.76, $p < 0.001$) of electrical conductivity and soil moisture for the entire analysis. Electrical conductivity increased with increases in the degree of soil wetness.

Altdorff *et al.* (2018) investigated the effects of agricultural treatments on the capability of electromagnetic induction use in soil water content mapping. They used the CMD-Mini Explorer instrument to measure electrical conductivity across the field and soil moisture probes for soil water content, which measured both moisture and temperature. Additional soil water content measurements were carried out using a portable Time-Domain Reflectometry sensor. Mean temperature readings were used to correct the apparent electrical conductivity readings for temperature effects using the equation given by Sheets and Hendrickx (1995). They analysed their results using a statistical approach where they looked at the correlation of apparent electrical conductivity to ground-truthing soil water content measurements. They obtained a statistically significant difference between soil water content and electrical conductivity.

Edeh (2017) conducted a study in South Africa to quantify Spatio-temporal soil water content by using the electromagnetic data acquisition using EM38. She collected soil water content information of a field using Dirk Friedhelm Mercker (DFM) moisture probes set up in the area of the survey. In her study, she reported that EM38 can map soil attributes using apparent electrical conductivity, which depends highly on the chemical properties of a soil medium. She sampled soil for laboratory analysis and apparent electrical conductivity calibration within the study area. She stated that soil sampling on a larger scale is not practical every time a survey is undertaken and recommended using soil water probes and immediate sensors used during surveys. Using the statistical regression approach, she analysed her data and found a good positive correlation between the soil apparent electrical conductivity and DFM soil water content measurements.

Bai *et al.* (2013) assessed the effects of physical properties of compacted soil on electrical conductivity. They performed geotechnical sieve analyses to determine soil particle distribution from soil samples collected at their study site. A self-designed device that measures electrical conductivity was used for the soil apparent electrical conductivity. A chamber that measures soil water content mounted on the device was used to measure water content through the drying of collected specimens. They found that electrical conductivity increases with increased soil water content and decreases with increasing dry density. They concluded that the electrical conductivity values become constant with increases in wetness, dryness, or a particular saturation degree.

CHAPTER THREE
MATERIALS AND METHODS

3.1 Study Area Description

The study area is the South African Barley Breeding Institute (SABBI) experimental farm number 5JII (18 ha) in Hartswater (see Figure 3.1), which is situated in the Phokwane Local Municipality of the Frances Baard District Municipality in the Northern Cape Province of South Africa around the coordinates: 24.739827° East and -27.720237° South. It is located near the border of the Northern Cape and North-West province in the Northern part of the Northern Cape. The study area is within the Vaalharts Irrigation Scheme in the northern regions. The Province is the biggest of all nine provinces in South Africa, with the lowest population and the highest poverty rate (Pauw, 2005).

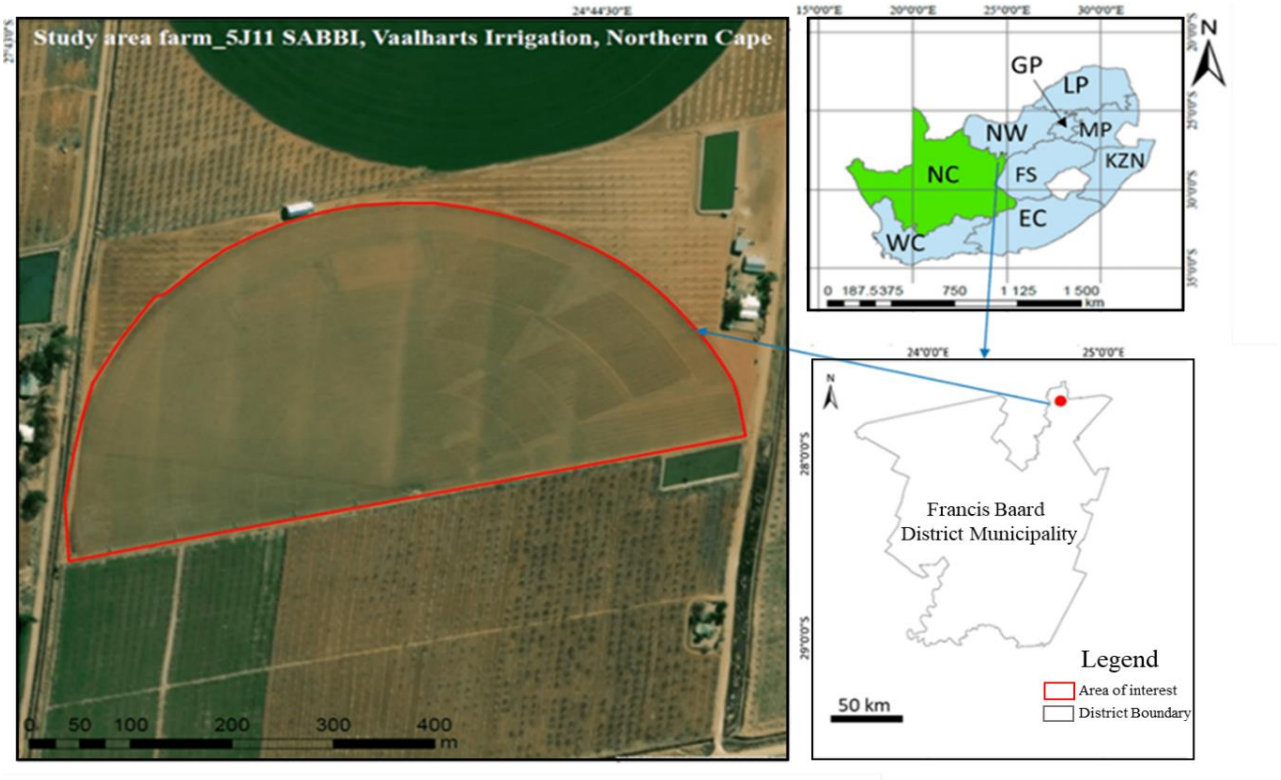

Figure 3.1: Showing the study area location within South Africa and its reference province.

3.1.1 Climatic conditions

The climate in Hartswater is characterized by long hot summer days and freezing winter days, with most of the rain occurring during the summer seasons between 1 November and 28 February (Seshoka and Faysse, 2004). Recordings of the average annual rainfall in the study area from 1975 to date have been 35 mm, while the minimum and maximum rainfall has been 13.5 mm and 77 mm, respectively. The mean maximum temperatures have been recorded at

31.8°C and mean minimum temperatures at 7 °C during the 1975 to 2019 period. From Figure (3.2), since 1975, there has been an increase in gradient for the mean annual maximum temperatures in summer and a decline in mean yearly minimum temperatures see Figure (3.3) below. The decrease in trends explains the shift in climate variability which has a greater influence in water resaources when temperatures become extremely high or too low with less precipitation events.

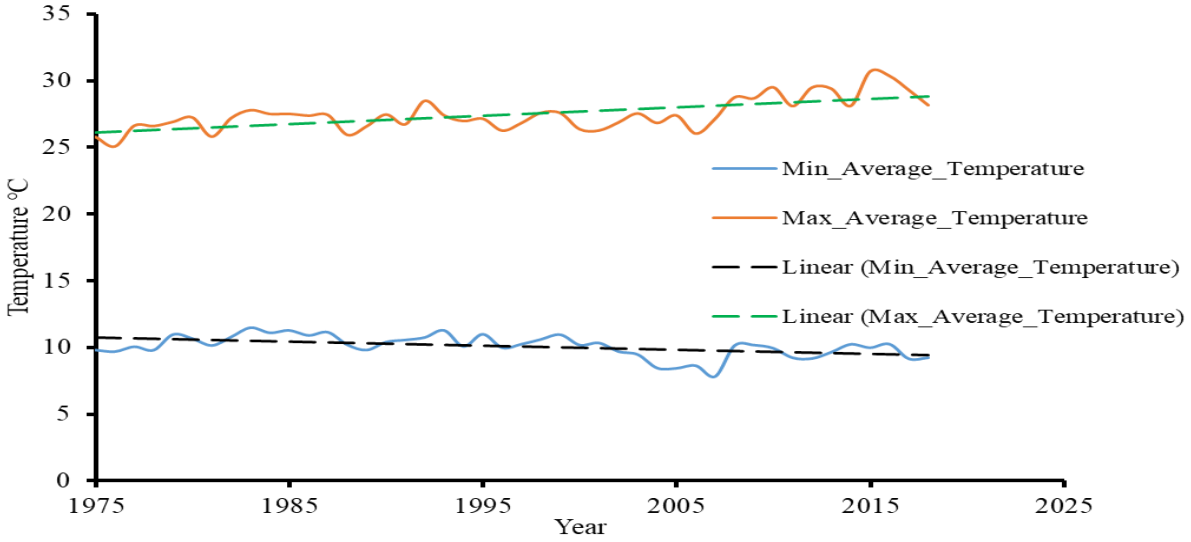

Figure 3.2: Temperature patterns in Hartswater (Agricultural Research Council, Natural Resources and Agricultural Engineering, Weather station).

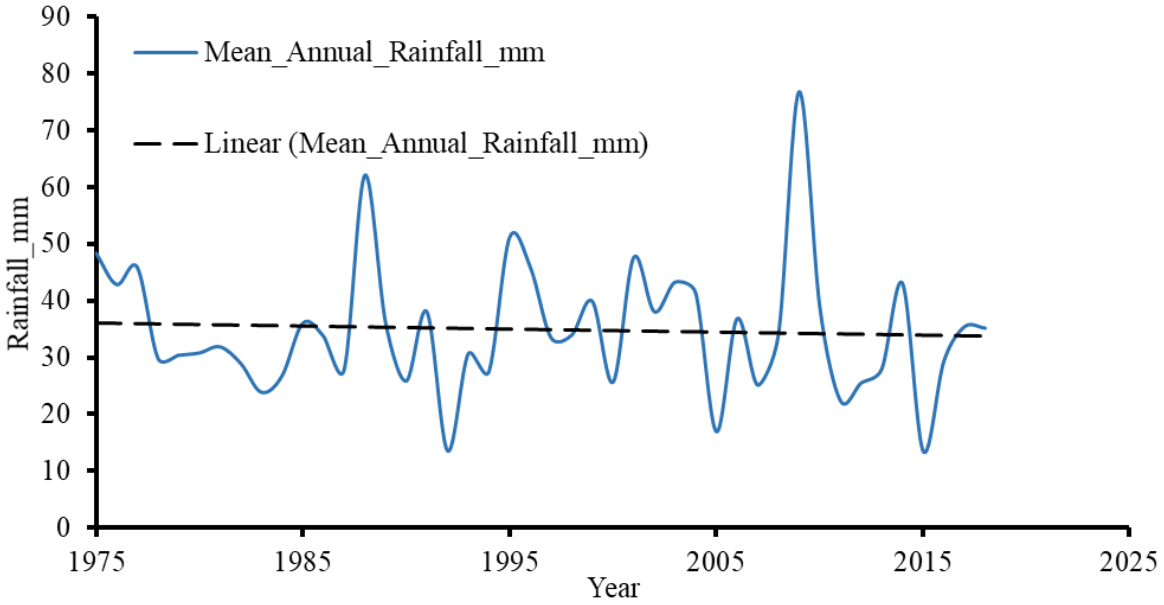

Figure 3.3: Mean annual rainfall patterns in Hartswater (Agricultural Research Council, Natural Resources and Agricultural Engineering, Weather station).

3.1.2 Topography

The study area is located in a flood plain of the Harts River with elevations ranging between 1170 m and 1080 m above sea level from Jan-Kempdorp to Hartswater (Verwey and Vermeulen, 2011).

3.1.3 Soils

Sandy soils dominate the study area with high silica content. Hough and Rudolph (2003) described the soil as the Kalahari sands. The sandy soil in Hartswater is susceptible to salinization and waterlogging conditions, due to a poor drainage system (Ramatsimela, 2007). Recently, a drainage network has been constructed in open canals, and subsurface drainage pipes have been installed to control water-logging conditions (Verwey and Vermeulen, 2011). According to Streutker (1977), the study area consists of two soils: Sunbury and Hutton. Irrigation on sandy soil replenishes soil water content to sustain the healthy growth of plants and crops. As a consequence, the rate at which water infiltrates this type of soil determines the frequency of irrigation which can be high; clay soil is only found at one-meter depth to two meters, which is far below the root zones of many crops (Verwey and Vermeulen, 2011).

3.1.4 Irrigation systems

Various forms of irrigation exist within the Vaalharts irrigation scheme, including surface flow irrigation using water from the canals, primarily used for plant irrigation, pivot irrigation systems, drip irrigation, bubblers, and sprinklers. Five dams exist within the scheme to support irrigation (Verwey and Vermeulen, 2011). The irrigation scheme is splitted into blocks with numbered farm plots per street. All plots feed on the main water canal into their dams which are located on every farm plot (Verwey and Vermeulen, 2011). Drip irrigation is one method that manages water as less evaporation loss occurs and reduces canopy damage through lodging (Verwey and Vermeulen, 2011). According to Brown (2008), the centre pivot irrigating system gives plants uniform irrigation, reduces human power and helps in fertigation, but much of the water is lost through evaporation. Like drips in reducing crop damage, Sprinklers can add fertilizers just like the pivot system (Verwey and Vermeulen, 2011).

3.1.5 Farming system

Farming activities taking place in the Vaalharts irrigation scheme include crop farming, fruit trees, and livestock farming. A number of crops are found in the scheme, which includes winter barley, groundnuts, potato, ground beans, oats, lucerne, tomatoes, spinach, beetroots, pumpkins, carrots, cabbages, onions, grapes, strawberries, watermelons, wheat and maize during the summer season, which is all irrigated. Fruit trees, including pecan nuts, olives, and citrus, exist within the scheme. The scheme is divided into two categories of farmers; small-scale and subsistence to commercial (Pretorius, 2018).

3.2 Data Acquisition Methods

This section provides details on all the techniques and approaches used to achieve the study's objectives (see Figure 3.4) below. Assessing crop water use within the irrigated barley field required a set of surveys which included: the use of unmanned aerial vehicle (UAV) surveys, smart lysimeters, the use of Dirk Friedhelm Mercker (DFM) capacitance probes, using EM38 and soil samples which were conducted in the experimental farm for a period of four months within the cropping season of August to November 2020. The Electromagnetic induction instrument (EM38) and an EC meter were used for soil electrical conductivity, to determine soil water content and soil moisture meters were utilized to acquire in-situ soil water content. Field lysimeters and a meteorological station were used to estimate crop water use.

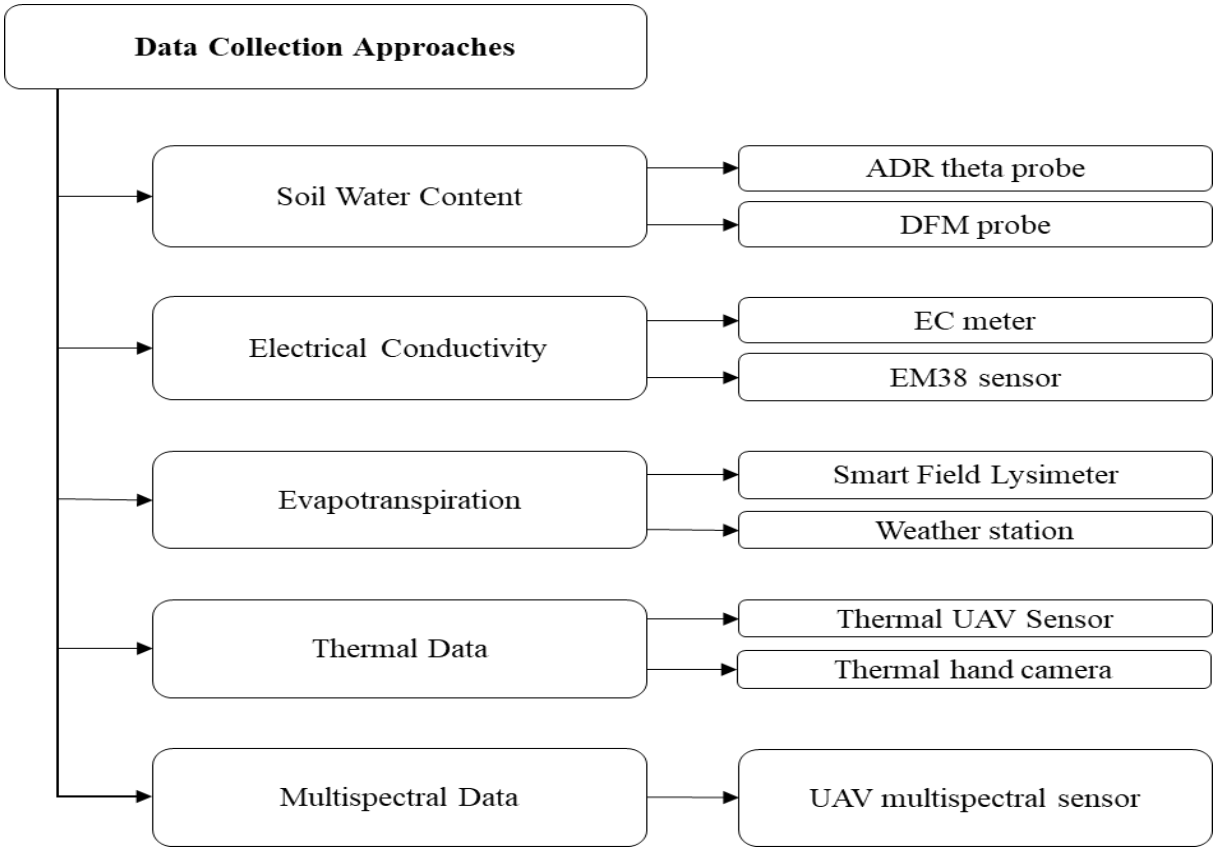

Figure 3.4: General flow diagram illustrating data collection approaches for the study.

3.3 Determination of Soil Water Content Distribution at Farm Scale

3.3.1 Soil Water Content (SWC) measurements

The in-situ soil water content measurement points were randomly selected across the study area over four fieldwork visits (11 August 2020, 22 September 2020, 23 September 2020 and 14 October 2020), using a Daiki-311A soil moisture meter probe which uses dielectric constant to measure the volumetric water content. A minimum of 20 points were collected around the field, all points were located using a Garmin global positioning system, and different locations were measured during each survey campaign. Measurements were taken at (0 cm -10 cm). The temperature and electrical conductivity were measured simultaneously during soil water content measurements using the thermal meter and the electrical conductivity meter. Measurements were done within the barley covered area and bare soil surfaces within the farm. Irrigation events data was extracted from Dirk Friedhelm Mercker (DFM) soil moisture probes installed within the field at different locations; the data included daily temperatures and soil water content percentages at different depths.

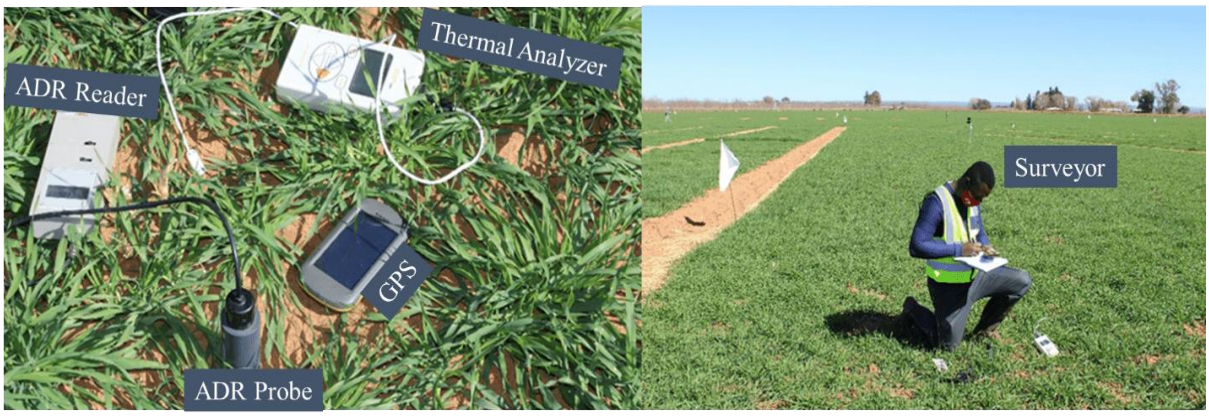

Figure 3.5: Showing the soil water content measuring probe, the thermal analyzer, a GPS and the surveyor during ground measurements.

3.3.2 Field Apparent Electrical Conductivity

For each soil water content (θ) measurement, apparent electrical conductivity (ECa) measurements were taken between 0-30 cm depths using a hand-held soil water content probe and an EC-meter. For spatial distribution of soil apparent electrical conductivity for the four field campaigns, a non-destructive electromagnetic induction (EM38) instrument was used to survey the area of interest indicated in (see Figure 3.6), taking measurements at four depths. The EM38 instrument was calibrated each time before the survey was done, according to the Geonics® instructions published in Canada. The surveyed area was cleared of all metallic objects to avoid the introduction of artificial magnetic noise, which included the removal of metal belts, watches, cell phones or any electronic devices that could affect the measurements. The surveying was done in two orientations: the horizontal dipole (Hz) measuring apparent electrical conductivity at 0-25 cm and 0-75 cm and the vertical dipole (Vz) measuring 0-50 cm and 0-100 cm. The survey lines followed the raw paths available between the barley crops, which changed with different field campaigns as the crop grew and canopy cover became dense. All stations surveyed were located using a GPS connected to the computer and the computer was connected to the instrument for data logging during the survey, (see Figure 3.7).



Figure 3.6: Showing the experimental farm and the area of interest used for the EM38 survey.

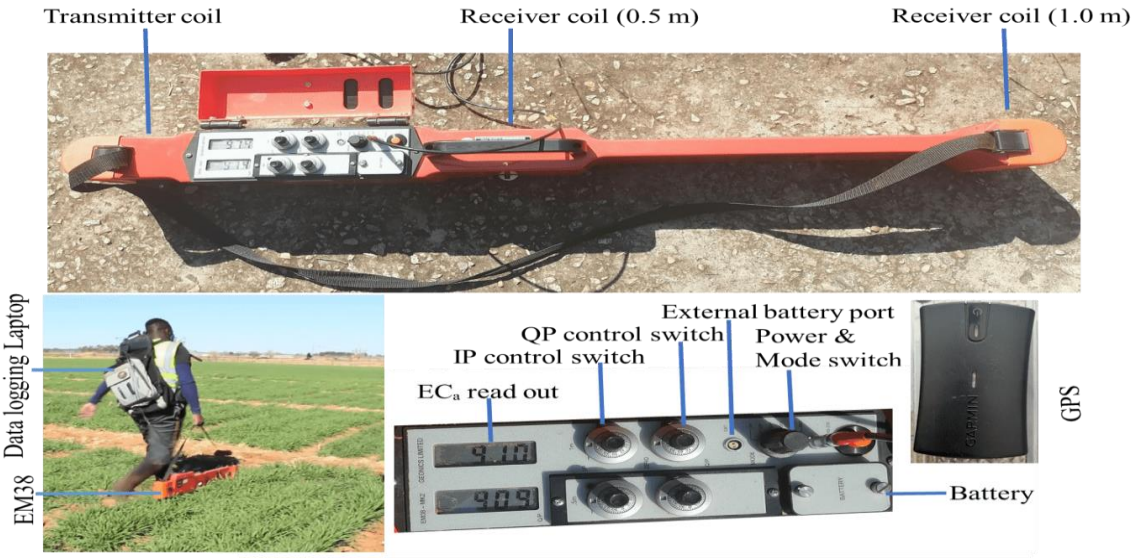

Figure 3.7: Showing the electromagnetic induction instrument and its components.

3.3.3 Data transformation and cleaning

All apparent electrical conductivity readings from EM38 were inspected for out of range, including negative and zero readings. Electrical conductivity readings from each survey station were corrected for temperature effects using Van Meerveld and McDonnell's (2009) equation given as:

$$ECa(T25) = ECa[0.4479 + 1.3801e^{\frac{T}{26.815}}] \quad (3.1)$$

Where ECa is the apparent conductivity measured at a point, T is the mean daily temperature with depth 0-1 m obtained from Dirk Friedhelm Mercker (DFM) probes.

3.3.4 Calibration of the electromagnetic induction instrument (EM38)

To calibrate the electromagnetic induction instrument (EM38), apparent soil electrical conductivity was measured in the horizontal mode (0.25 m – 0.75 m) and vertical mode (0.50 m- 1 m) within the EM38 survey area of interest. Following the EM38, soil samples were collected at four different sites within the EM38 survey area of interest to determine soil properties. At each point, a hand auger was used to take cores from 0 m -1 m at an interim of 0.25 m with depth adding to four cores being taken from each point (see Figure 3.8).

For every core taken, physical properties including in-situ soil water content, electrical conductivity and temperature were measured before sample packaging. All core soil samples were stored in zip-lock bags labelled with GPS coordinates, depth and sample number; zip-lock bags were used to prevent moisture loss from the samples. The samples were taken to the laboratory for physiochemical analysis. Similar soil properties, including soil water content and electrical conductivity saturated at 1:2.5, were analysed at the laboratory. Additional soil properties that included the SAR properties (Mg, Ca, Na and K) cations and the soil pH were also analysed as other soil attributes influencing the ECa response. Linear regression analyses were applied for all depths and sample points to establish a relationship between temperature corrected ECa-EM38, ECa from EC-meter, ECe, soil water content and other soil properties, which best describes their correlations.

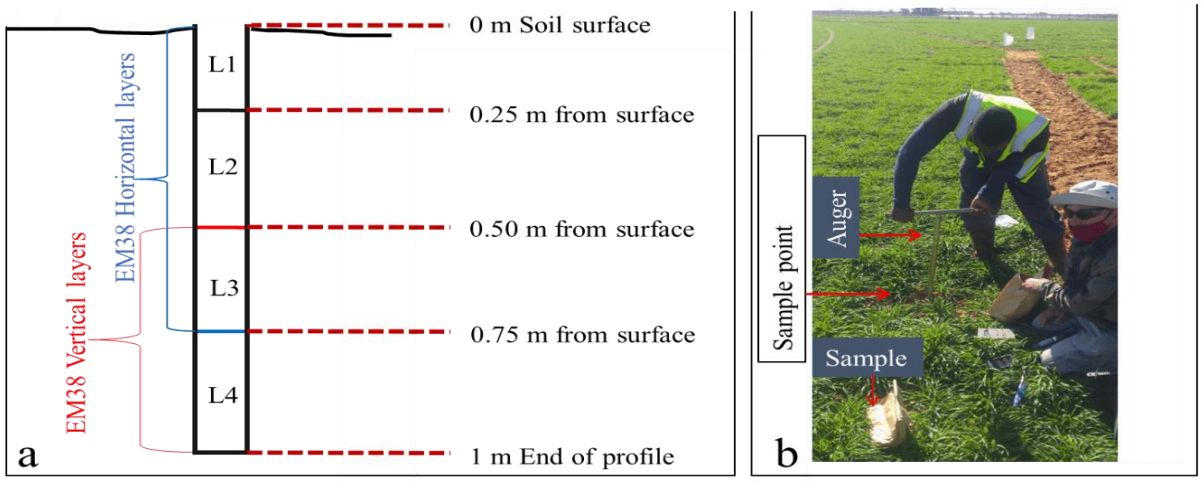

Figure 3.8: Soil sampling at different depths for EM38 calibration. a) Different layers of soil taken at each calibration point, b) Surveyors taking core samples at different depths equivalent to the EM38 measurement depth.

3.4 Data Processing and Analysis

3.4.1 Spatial distribution of soil properties

The spatial distribution patterns of soil electrical conductivity under different irrigation events were determined using EM38 readings. The survey EM38 measurements were interpolated by applying inverse distance weighting model in ArcGIS to map the spatial distribution of electrical conductivity in the selected area of interest within the barley field.

The inverse distance weighting interpolation model was selected due to its capability to interpolate unknown areas without making estimations below the minimum or above the maximum electrical conductivity reading.

The maps showing the soil's apparent electrical conductivity were produced with a pixel size of 35 cm x 40 cm. Spatial distribution maps were done for four depths of the farm soil at the selected area of interest for all four field campaigns, with the first layer being the root zone of the barley crop.

3.4.2 Conversion from ECa to SWC

From the interpolated electrical conductivity spatial distribution layers, soil water content was estimated, employing a calibration relationship between in-situ soil water content and electrical conductivity. A power regression model was developed from EM38 field campaign data to estimate the soil water content percentage in four layers of each campaign.

On the developed model, electrical conductivity was set as the independent variable, while soil water content was selected as a dependent variable. From the power equation $Y=AX^B$, the relationship between soil water content (θ) and soil electrical conductivity (ECa) was expressed as.

$$\theta = \mathrm{ECa}^{B} \tag{3.2}$$

Where θ represent the soil water content, and ECa is the apparent electrical conductivity; to determine θ, equation (3.2) was applied to the ECa raster files in the raster calculator in the ArcMap environment to produce θ maps.

3.4.3 Data analysis and evaluation

The interpolation approach was used to process and map the spatial variability and distribution of soil electrical conductivity, while the statistical approach for evaluating the relationships between the apparent electrical conductivity (ECa), soil water content (θ) and other soil attributes were used. The relationships were established using regression analysis.

A correlation coefficient (r) with a coefficient of determination (R^2) values was established in every relationship between the soil electrical conductivity and soil attributes, as the primary measure of model goodness of fit. Furthermore, correlation analysis using Pearson's Correlation (p-value) was conducted to understand the relationship between soil water content (θ) and the soil electrical conductivity, to assess whether the relationship has a statistically significant difference.

3.5 Evapotranspiration Estimation using Smart Weighing Lysimeters

3.5.1 Lysimeters installation and data measurements

To determine the rate of evapotranspiration occurring within the field, two field smart lysimeters (SFL-600) were installed at the beginning of the cropping season within the experimental barley farm, to measure and monitor soil water components behavior.

The lysimeters measured soil water content, electrical conductivity, drainage and evapotranspiration.

The lysimeters measured the actual evapotranspiration in real-time and monitored the water usage within the irrigated crop field. Each lysimeter was a cylinder with 60 cm height and a diameter of 30 cm; the cores were used to cut an undisturbed core sample of soil and crop that represented the in-situ conditions of the field (see Figures 3.9 to 3.11).

The lysimeters were mounted with soil moisture and potential sensors at different depth intervals (5 cm, 30 cm and 55 cm). Each lysimeter had a weighing balance, which measured the weight of the lysimeter. All lysimeters were connected to one data logger box, which was equipped with a solar panel for power supply for the entire system.

The data logger had the capability of recording and sending measurements to a central database using a built-in modem connection which can be accessed from the office throughout the season. Each lysimeter was also connected to its drainage box, which

contained a drainage pump and a container with a balance to measure the drainage container's weight (see Figure 3.10). A tensiometer was installed at an angle for soil water tension measurement alongside each box. Measurements were automatically taken every 10 minutes.

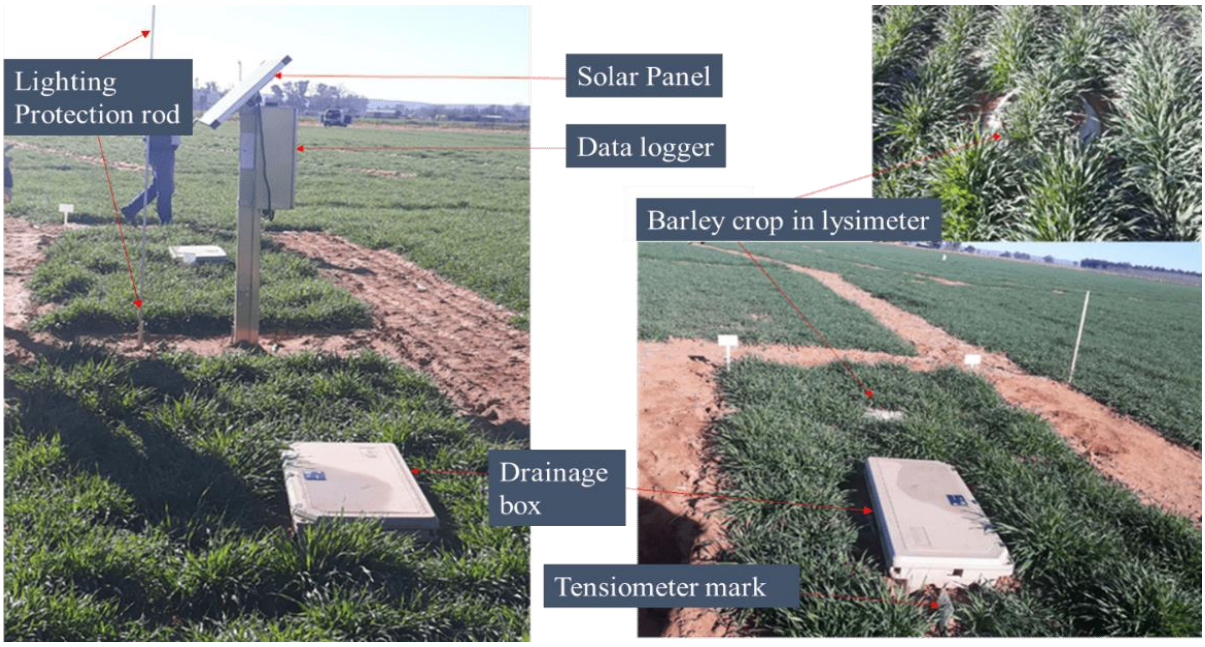

Figure 3.9: Showing the installed lysimeters in the field.

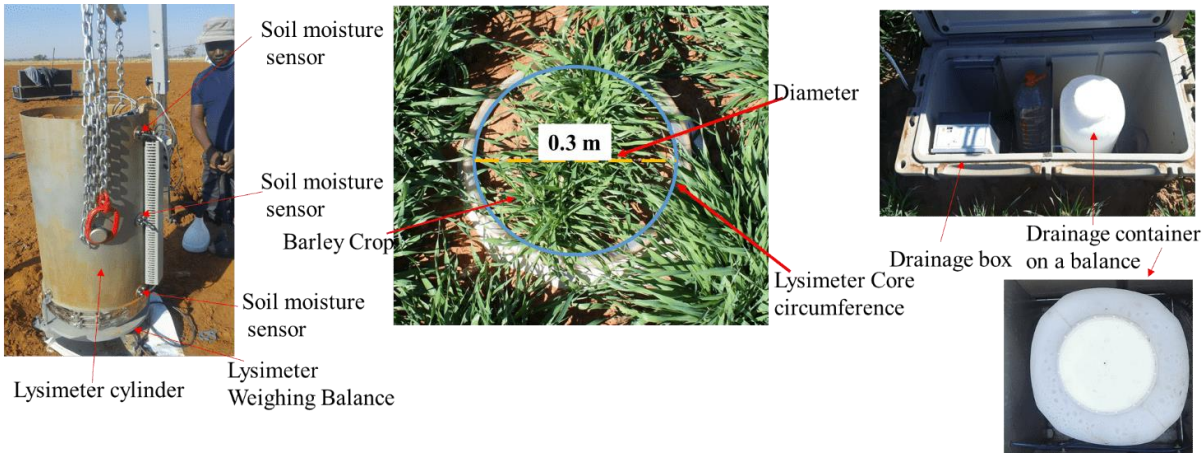

Figure 3.10: Showing the schematic overall lysimetric system and its components.

3.5.2 Evapotranspiration Estimation using weighing lysimeters

Estimation of evapotranspiration using weighing lysimeters was computed based on the weight changes of the lysimeter balance during the periods when irrigation has ceased and on rainless days. The lysimeter evapotranspiration was estimated using the formula:

$$ET_a = \frac{(LYW_n + SWW_n) - (LYW_{n+b} + SWW_{n+b})}{\left(\frac{\pi}{4}\right) 0.3^2} \quad (3.3)$$

ET_a represents the actual evapotranspiration on an nth day, LYW_n represents the weight of the lysimeter in kg on the midnight of the nth day, SWW_n represents the weight of the percolate water vessel storage also in kg on the midnight of the nth day. LYW_{n+b} and SWW_{n+b} represents the lysimeter weight and storage vessel weight on the nth day of the next day. The water density was assumed to be 1000 kg $m^{-3,}$ while 0.3 is the diameter of the inner core barrel of the lysimeter.

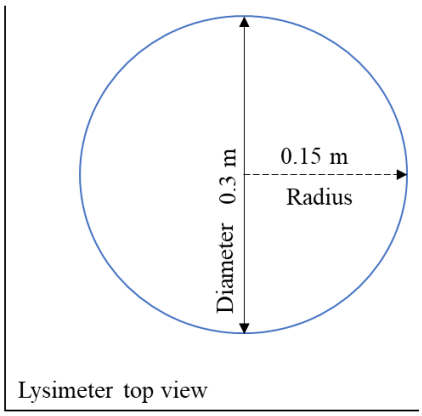

Figure 3.11: The top view of the lysimeter and the dimensions.

To convert the mass of the lysimeter from kilograms to millimetres, the water density assumed to be 1000 kg m^{-3} which was converted to 0.001 m^3. The water density of 0.001 m^3 was divided by the surface area of the lysimeter being 0.0707 m^2 as shown in (see Figure 3.11), equal to 0.014 m equivalent to 14 mm.

3.5.3 Evaluation and validation of lysimetric evapotranspiration

Soil water content (θ percent) measurements obtained from the lysimeter sensors were used to evaluate and validate the accuracy of the lysimeter's evapotranspiration estimation on an hourly basis. Estimates of daily evapotranspiration were evaluated using weather data computed evapotranspiration.

3.6 Evapotranspiration Estimation using Weather Data

The Penman-Monteith method was used to determine the reference evapotranspiration (ET_0) as the readily available soil water content which has been vaporized from the surfaces of the barley crop.

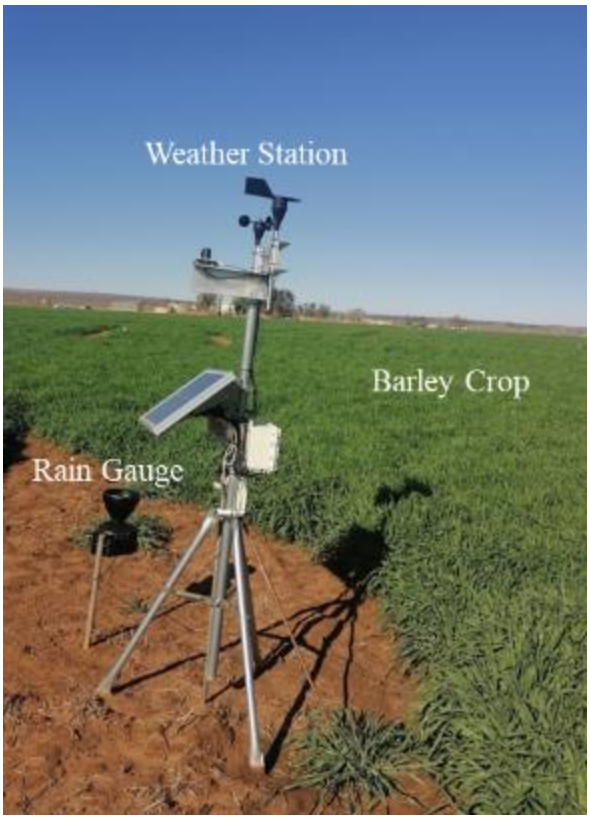

Figure 3.12: Weather station installed north of the lysimeter in the field.

The parameters from the weather station in (see Figure 3.12) were applied in the equation given as:

$$ET_0 = \frac{0.408\Delta(R_a - G) + \gamma\left(\frac{900}{T+273}\right)u_2(e_s - e_a)}{\Delta + \gamma(1 + 0.34u_2)} \quad (3.4)$$

Where the reference evapotranspiration is denoted by ET_0 in mm/day, Δ notation represents the slope of saturated vapour pressure against temperature curve in Kpa/℃. Rn denotes the total daily net radiation in $MJm^2\ day^{-1}$. The term G, represents the total net soil heat flux. ϒ denotes psychrometric constant in Kpa/℃, T is the average daily temperature in℃. U_2 represents the average daily wind speed in $m\ s^{-1}$, where e_s represent the average daily saturated vapour pressure in Kpa while e_a represents actual average vapour pressure in Kpa measured on a daily basis.

The parameters of the above equation were calculated in 22 steps which are as follows:

Step one (1) was to calculate the mean daily temperatures using the equation:

$$T_{_mean} = \frac{Temperature_{max} + Temperature_{min}}{2} \quad (3.5)$$

T_mean is the daily mean temperatures in℃, Temperature max and Temperature min are the highest and lowest daily temperatures in℃.

Step two (2) was to calculate the daily mean solar radiation using the equation:

$$R_S = \frac{Radiation_{Max} + Radiation_{Min}}{2} \quad (3.6)$$

Where Radiation max and Radiation min are the maximum and minimum radiation respectively in MJ m^{-2}, from the weather station data in was expressed in W $m^{-2,}$ which was changed to MJ m^{-2} by multiplying the values by 0.0864 as the conversion constant.

Step three (3) was to determine the daily average speed of wind in m s^{-1} measured at 2 meters above ground using the formula:

$$U_2 = \frac{U_{Max} + U_{Min}}{2} \quad (3.7)$$

Where U_{max} and U_{min} represent lowest and the highest temperatures in℃.

The fourth step (4) was to compute the slope of saturation vapour pressure s follows:

$$\Delta = \frac{4098[0.6108\exp(\frac{17.27 \times T_{Mean}}{T_{Mean} + 237.3})}{(T_{Mean} + 237.3)^2} \quad (3.8)$$

Where (exp) is the natural logarithm base equal to 2.7183, while T_{mean} is the daily average temperature in℃.

Step five (5) was calculating the atmospheric pressure as follows:

$$P = 101.3[\frac{293 - 0.0065Z}{293}]^{5.26} \quad (3.9)$$

Where Z denotes height above the mean sea level of the area in meters (m).

Step six (6) was to calculate the Psychrometric constants as follows:

$$\gamma = \frac{C_p P}{\varepsilon \lambda} = 0.000665P \tag{3.10}$$

Where P denotes the atmospheric pressure in Kpa calculated in step six.

Step seven (7) was to calculate the delta term as follows:

$$DT = \frac{\Delta}{\Delta + \gamma(1 + 0.34U_2)} \tag{3.11}$$

The Δ sign is the slope of saturation vapour pressure as calculated in step four, ϒ is the psychrometric constant and U_2 is the wind speed.

Step eight (8) was to calculate the Psi term used to compute the wind term in the late stages as follows:

$$DT = \frac{\Upsilon}{\Delta + \gamma(1 + 0.34U_2)} \tag{3.12}$$

Where the variables in the equation are the same as step seven.

Step nine (9) was to determine the temperature term calculated as follows:

$$TT = \left[\frac{900}{T_{mean} + 273}\right] \times U_2 \tag{3.13}$$

Where T_{mean} represents the daily average temperature in ℃ and U_2 being the wind speed term.

Step ten (10) was to calculate the mean saturated vapour pressure using the three equations below as follows:

$$eT_{max} = 0.6108\exp[\frac{17.27T_{max}}{T + 237.3}] \tag{3.14}$$

$$eT_{min} = 0.6108\exp[\frac{17.27T_{min}}{T + 237.3}] \tag{3.15}$$

$$e_s = \frac{e_{(Tmax)} + e_{(Tmin)}}{2} \tag{3.16}$$

Tmax = highest air temperature in 24 hours, ºC; Tmin = lowest air temperature in 24 hours, ºC.

Step eleven (11) was to calculate the actual vapour pressure as follows:

$$e_s = \frac{e_{(Tmin)}\left[\frac{RH_{max}}{100}\right] + e_{(Tmax)}\left[\frac{RH_{min}}{100}\right]}{2} \quad (3.17)$$

The component e_a is the actual vapour pressure in KPa; $e_{(Tmin)}$ denotes the saturation vapour pressure at a daily lowest temperature in KPa, while $e_{(Tmax)}$ is the saturation vapour pressure at a daily highest temperature in Kpa. In contrast, RHmax denotes the highest relative humidity a percentage, and RHmin represents the lowest relative humidity in percentage.

Step twelve (12) was to calculate the inverse distance of the earth to the sun, as well as the declination of the sun, using the two equations below as follows:

$$d_r = 1 + 0.033COS\left[\frac{2\pi}{365}J\right] \quad (3.18)$$

$$\delta = 0.409Sin\left[\frac{2\pi}{365}J - 1.39\right] \quad (3.19)$$

Where J = the number of the day of the year between 1 January and 31 December of that year.

Step thirteen (13) was to convert the latitude to radians using the following formula:

$$\varphi = \frac{\pi}{180}[Decimal\ degrees] \quad (3.20)$$

Step fourteen (14) was to calculate the sunset hour angle using the equation:

$$w_s = arcos[-\tan(\varphi)\tan(\delta)] \quad (3.21)$$

Where φ is the latitude expressed in radians and δ is the solar declination.

Step fifteen (15) was to calculate the extraterrestrial radiation using the formula:

$$R_a = \frac{24(60)}{\pi} G_{sc} d_r[(w_s sin\varphi sin\delta) + (\cos\varphi\cos\delta w_s)] \quad (3.22)$$

Ra represents the extraterrestrial radiation in MJ $m^{-2}day^{-1}$, Gsc represent solar constant which is 0.0820 MJ m^{-2} min^{-1}, dr is the inverse earth distance to the sun calculated in step 12, s being the angle of the sun at sunset hours, φ is the latitude in radiant, while δ is the sun declination.

Step sixteen (16) was to calculate the clear sky sun radiation as follows:

$$Rso = (0.75 + 2E10 - 5z)Ra \quad (3.23)$$

The component z represents the height above sea level in meters and Ra is the extraterrestrial radiation in MJ m^{-2} in a day.

Step seventeen (17) was to calculate the net solar radiation using the equation:

$$Rns = (1 - a)Rs \quad (3.24)$$

Where Rns denotes the total solar radiation expressed in MJ m^{-2} day^{-1}, while a is the albedo equal to 0.23 for a reference crop, and Rs is the incoming sun radiation in MJ m^{-2}/day^{-1}.

Step eighteen (18) was to compute the total outgoing long radiation as:

$$R_{nl} = \sigma\left[\frac{(T_{max} + 27.3.16)^4 + (T_{min} + 273.16)^4}{2}\right](0.34 - 0.14\sqrt{e_a})\left[1.35\frac{R_s}{R_{s0}} - 0.35\right] \quad (3.25)$$

Rnl represent the total outgoing long-wave radiation in MJ $m^{-2}day^{-1}$, whereas a represent the Stefan-Boltzmann constant equivalent to 4.903×10^{-9} MJ K^{-4} m^{-2} day^{-1}. At the same time, Tmax is the lowest absolute temperature in a day measured in °C. Tmin is the lowest absolute temperature in a given day, and ea being the actual vapour pressure expressed in KPa. At the same time, Rs denotes the incoming sun radiation in MJ $m^{-2}day^{-1}$, and Rso is the clear sky condition solar radiation, MJ $m^{-2}day^{-1}$ calculated in step 16.

Step nineteen (19) was to calculate the net radiation as follows:

$$Rn = Rns - Rnl \quad (3.26)$$

Rns is the net shortwave solar radiation measured in MJ m^{-2} day^{-1}, and Rnl is the net outgoing long-wave radiation in MJ $m^{-2}day^{-1}$. Expressing the total radiation (Rn) being equivalent to the rate of evaporation (Rng), the following equation was used:

$$Rng = 0.408 \times Rn \quad (3.27)$$

Where Rn is the total sum of radiation in MJ m^{-2} day^{-1}.

Step twenty (20) was to calculate the radiation term using the following equation:

$$ETrad = DT \times Rng \quad (3.28)$$

Where ETrad is the radiation measured in mm day ^{1}, while DT is the Delta term and Rng is the net radiation in mm.

Step twenty-one (21) was to calculate the wind term using the equation:

$$ETwind = PT \times TT\,(es - ea) \quad (3.29)$$

Where ETwind denotes the wind term measured mm day^{-1}, PT is the Psi term, TT is the Temperature term, and e_a is the actual vapour pressure in Kpa.

The final step, which is step twenty-two (22), is the estimation of the reference evapotranspiration using the formula:

$$ETo = ETwind + ETrad \quad (3.30)$$

Where ET_0 denotes reference evapotranspiration measured in mm day^{-1}, ETwind is the wind term in mm day^{-1}, while ETrad is the radiation term in mm day^{-1}.

3.6.1 Validation

The reference evapotranspiration computed from the Penman-Monteith method was validated for un-biasness using Priestley and Taylor's equation given as:

$$ET_0 = \frac{1}{\lambda}[\alpha \frac{\Delta}{\Delta + \gamma}(R_n - G)] \quad (3.31)$$

From the equation, α is the imperial coefficient, which in FAO 56 it is 1.26, λ denotes the latent energy of vaporization which is 2.45 MJ kg^{-1} according to FAO-56, γ represent the Psychrometric constants. At the same time, Rn and Δ are the total radiation and the slope of saturation vapour pressure, respectively.

3.7 Use of Unmanned Aerial Vehicle (UAV) for Aerial Surveys

A DJI Matrice M-600 unmanned aerial vehicle was used in this study. The vehicle can be used for various applications in different industries such as the movie filming industry, security companies, mining monitoring, food deliveries, and application in agriculture. The vehicle carries up to 5.5 kg of weight using six TB48S batteries and 6 kg using six TB47S

batteries. For this study, the unmanned aerial vehicle was connected with a Multispectral (MSI) camera to accomplish the study's objectives. At the same time, an Inspire-1UAV was used equipped with a thermal (TIR) Zenmuse sensor (see (Figures 3.13 and 3.14). The vehicles are equipped with onboard GPS, which locates the vehicle's position and the location of captured imageries (see Figure 3.13).



Figure 3.13: M600 DJI drone equipped with a multispectral camera.

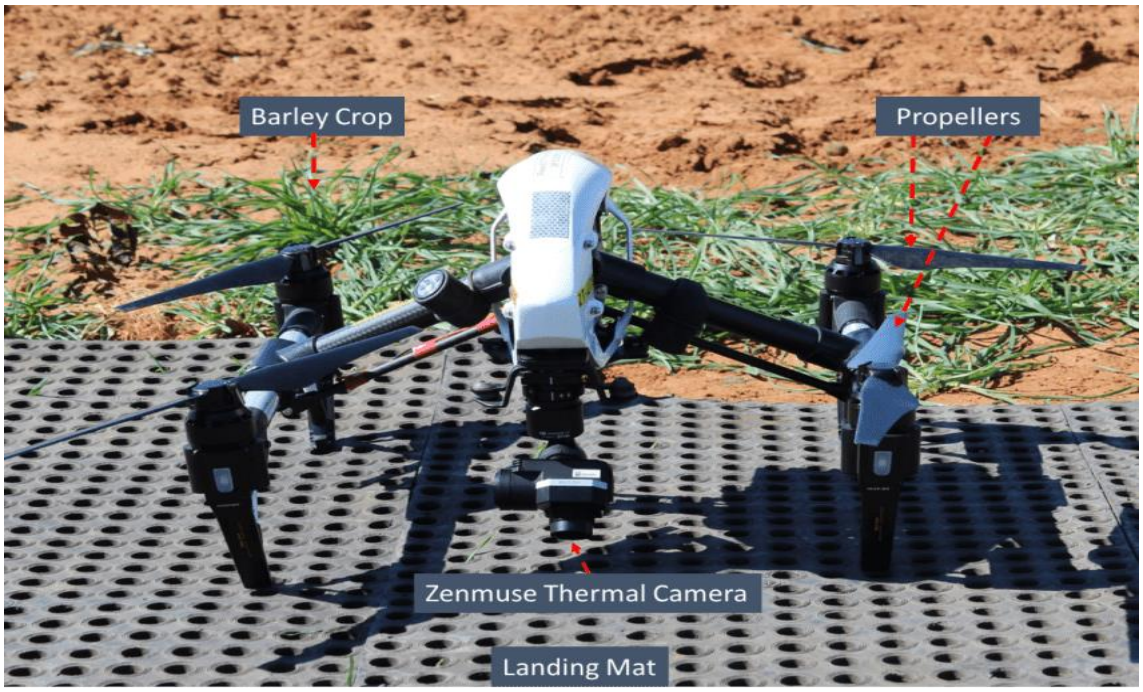

Figure: 3.14: DJI Inspire 1 UAV equipped with a Zenmuse XT thermal camera.

3.7.1 Pre-flight planning

For this study, two types of cameras, Multi-spectral (MS) and Thermal infrared radiance (TIR) sensors, were used mounted on an the UAV to survey within the study area for three months within the barley-cropping season. Acquired imageries were processed and used to derive various crop water use related variables. As outlined in figure (3.15) below, for the successful acquisition of high-resolution multispectral and thermal imageries, before any UAV flying; the selection of a site that best fits the requirements of flying as required by South African Aviation were key for all the survey. This includes the flying region, wind speed, climatic conditions and flying time. Morning, afternoon, and sunset flights were undertaken, and all records were kept (see Table 3.1). Air control security measures were performed, which involved communicating with other pilots within the flying region as an incident control measure. Multispectral and thermal infrared radiance sensors were applicable for the survey in this study. The flight path design were designed in a manner that covers the entire area of interest fully.

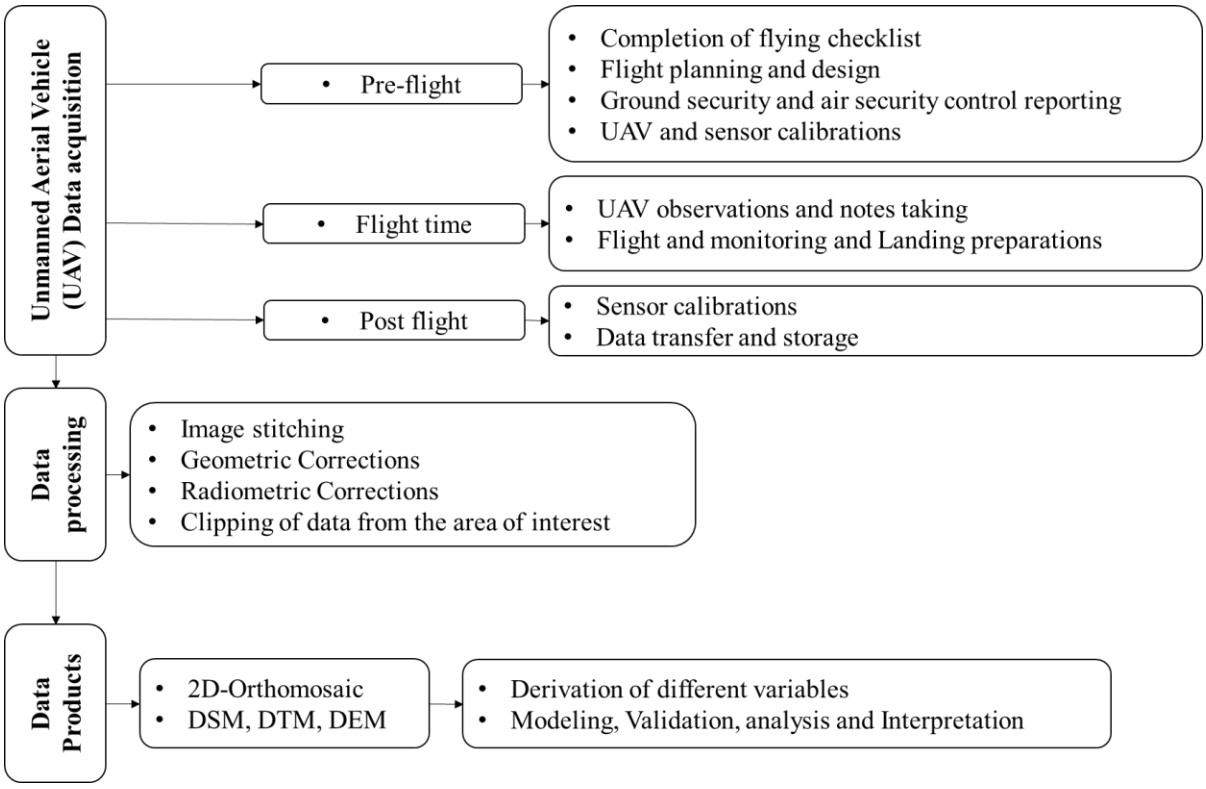

Figure 3.15: Flow diagram illustrating the steps necessary to achieve UAV data set.

Table 3.1: Flight plan details table for each survey.

Date of flight	Time	Sensor type	Height above ground (m)	Pixel size (cm)

08 August 2020	12:06	MS & TIR	120	2.7
22 September 2020	11:35	MS & TIR	120	2.7
14 October 2020	12:13	MS & TIR	120	2.7

All planned flights were conducted at the height of 120 m above the target with multispectral sensors (MS) and Thermal sensors (TIR) during mid-day on different dates (see Figure 3.15). All imageries had pixels of 2.7 cm, as indicated in Table 3.1 above. Flying at different heights depends largely on the resolution of interest, flying at 120 m above ground would give about 2.7 cm pixel size while flying at 30 m above ground gives about 1 cm pixel size. Flying at 120 m above target permits a large area coverage, whereas a low height flight reduces coverage area although the resolution gets imoproved. Low flying can be restricted by tall objects or by aviation rules which requires flying of UAV's between 30 m and 120 m height.

All flights were conducted within the allowed zone/space of Johannesburg Area South-West (FAJA ACC SW) flight level 1100 m- 4600 m. The flights were conducted at 27.91 km away from the Jan-Kempdorp airport. The fly region is located at the flight control frequency 128.3 MHz which was used for radio reporting as a safety measure throughout the missions.

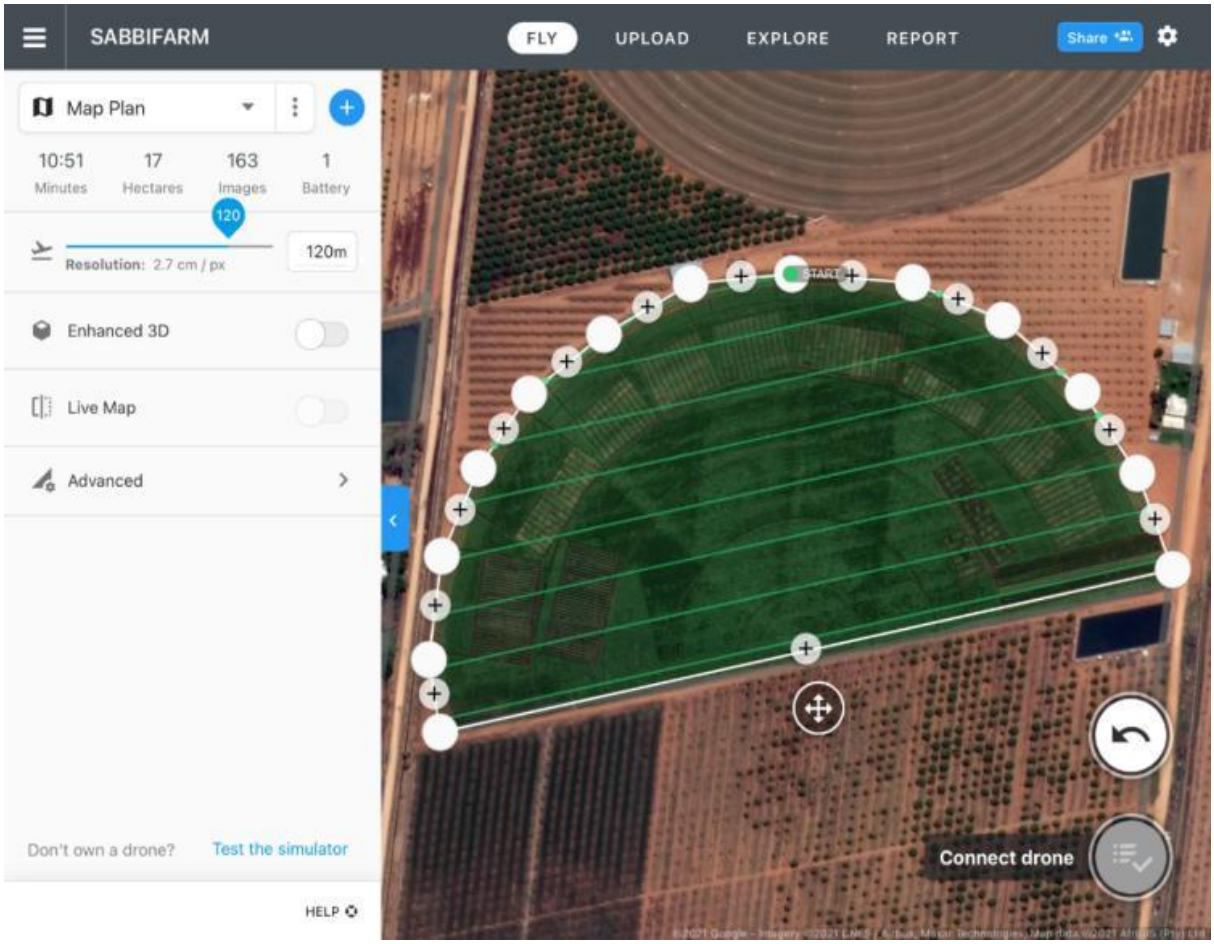

Figure: 3.16: Showing flight lines, height and duration.

3.7.2 Survey sensor types

Two types of sensors were used for this study as described below.

Multispectral sensor (camera) description

In this study, the Red Edge Mica-sense multispectral camera was used. The camera images the ground with five separate bands which are: (near-infrared (NIR)-840 nm band centre, 57 nm of bandwidth; red edge being 717 nm band centre, 12 nm bandwidth; red being 668 nm band centre, 14 nm of bandwidth; green being 560 nm band centre, 27 nm bandwidth and the Blue-475 nm band centre, 32 nm bandwidth). The camera can image the ground at the highest height of 120 m above ground at approximately 8 cm pixel resolution. The camera weighs 231.9 grams.

Thermal sensor (camera) description

The Zenmuse XT-2 thermal camera was used to acquire thermal images for this study. The camera is applicable in numerous fields, including power line inspection, solar panels

inspection, security search and rescue, precision agriculture, and firefighting and fire mapping. The camera has a lens focus of 19 mm, image resolution of 640x512, a pixel pitch of 17 µm, spectral band 8-15 µm, low scene range of -40℃ to 150℃ at high gain and 100℃ to 550℃ low gains.

3.7.3 Image processing and ortho-rectification

All images captured were processed and stitched together with various bands using Drone2Map for ArcGIS, which is professional drone mapping software. Extraction, manipulation, deriving of other variables and analysis from the images fit the study objectives**.**

Geometric Calibration

Ground control points within the flight path of the study area were used for the geometric calibration of the images. Known marked ground objects with known geographic positions were used as ground control points.

Radiometric Calibration

For multispectral camera images, a Calibrated Reflectance Panel (CRP) with white and dark colours in (see Figure 3.16) was placed at a fixed point below the sensors before and after flying, to acquire intrinsic camera parameters focal distance, distortions and sun angle. Calibrated reflectance panel images were used to convert individual radiance pixel values to reflectance pixel values by multiplication of each pixel radiance value of every captured image by the reflectance calibration factor.

The process was applied to all five bands independently to reflectance units. In general, the relationship established between raw individual pixel values/ digital numbers and reflectance pixel values was applied on the mosaicked imagery to change raw pixel digital numbers into reflectance pixel values.



Figure 3.17: Showing the calibration panel for multispectral radiometric calibration.

Thermal Calibration

Thermal images were calibrated using ground targets measured temperature using a ground hand-held thermal camera during the flight time (see Figure 3.17). Measurements taken by the ground thermal camera were compared with measurements taken using a thermal sensor on the UAV. The relationship between the UAV readings with the ground readings was applied to the thermal UAV imagery.

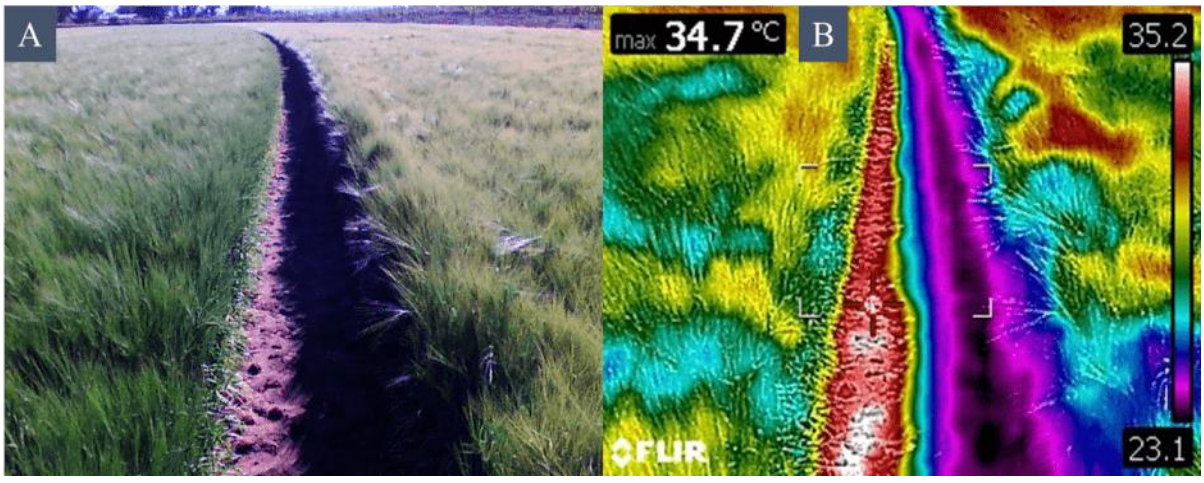

Figure 3.18: Thermal calibration images were taken using a handheld FLIR thermal camera (A) showing the natural colour of the field while (B) depicts the thermal image of the same field part.

3.8 Quantification of Evapotranspiration Based on UAV Data and Triangular Method

Evapotranspiration quantification from the UAV data set was carried out using a triangular method. The method uses multispectral and thermal data to generate vegetation index and the surface radiometric temperature. An area near the Lysimeters was selected as an area of assessment similarly to what had been done in the other sections; the area was covered by thermal (Tir) and multispectral (MSI) images. The Normalized Difference Vegetation Indexes (NDVI) were computed from the multispectral imageries for the survey days.

The temperature images were used to calculate the temperature-dryness index, which is the scaled surface radiance temperature. Temperature values are normalized to range between 0 and 1. High values of NDVI represent the full cover of vegetation, while low NDVI represents low coverage, usually bare soil. It is the same with temperature.

High temperatures indicate dry surfaces, whereas low temperatures denote wet surfaces. From NDVI and TIR images, pixels are selected to accommodate dense vegetation, dry surfaces and wet surfaces. Scaled surface radiance temperatures were plotted against the fractional vegetation index (T*/Fr) from the selected pixels.

The ratio of pixels were converted to moisture content denoted as (Mo) and the evaporative fraction was represented as (ET) using the mathematical equations given below. The spatial variability of soil water content (SCW) percentages were computed, from the linear relationship between the in-situ soil water content observations and moisture index (Mo), based on a simple linear regression model. Furthermore, the spatial distribution of actual evapotranspiration for different days at certain hours were computed based on the energy balance equations listed in this section.

$$NDVI = \frac{\text{NIR_band} - \text{RED_band}}{\text{NIR_band} + \text{RED_band}} \tag{3.32}$$

Where NDVI represents the normalized difference vegetation index, and NIR_band denotes near-infrared band while RED_band being the red band.

$$Fr = \frac{\text{NDVI} - \text{NDVI}_L}{\text{NDVI}_H - \text{NDVI}_L} \tag{3.34}$$

Where Fr represent the field fractional vegetation cover, $NDVI_L$ denotes the lowest NDVI values, while $NDVI_H$ denotes the highest NDVI values.

$$T* = \frac{\text{Tir} - \text{T}_{minimm}}{\text{T}_{maximum} - \text{T}_{minimum}} \quad (3.35)$$

Where T* is the scaled UAV mapped temperature index, Tir being the surface radiometric temperature, Tminimum denotes the minimum surface temperature and Tmaximum being the maximum surface temperature.

$$T * warmedge = 1 - Fr \quad (3.36)$$

Where T* is the scaled UAV temperature index.

$$Tirwarmedge = a + b \times NDVI \quad (3.37)$$

Where Tir is the surface UAV derived radiometric temperature.

$$Mo = 1 - T * (Pixel)/(1 - Fr) \quad (3.38)$$

Where M_0 is the moisture availability.

$$EF = EFsoil(1 - Fr) + FrEFveg = Mo(1 - Fr) + Fr \quad (3.39)$$

Where EF denotes Evapotranspiration fraction (EFsoil medium=Mo and EFvegetation area=1).

To determine the actual evapotranspiration, the following formula was applied.

$$EF = ETa/(Rn - G) \quad (3.40)$$

Where EF is the evaporative fraction, ETa being the actual evapotranspiration, Rn is the net radiation observed for a particular hour, and G is the sensible ground heat flux. Because G denotes the energy going into the soil during the day and being released at night, it was negligible in the analysis as it has a small component of the energy balance. The net radiation (Rn) was obtained as MJ m^{-2} day^{-1} from the weather station data and converted to millimetres (mm) using the conversion factor 0.408, which means 1 MJ m^{-2} day^{-1} is equal to 0.408 mm day^{-1}. Therefore, ETa was computed from:

$$ETa = (EF \times Rn \times \Delta t)/LE \quad (3.41)$$

Where delta (t) denotes time interval, and LE being the latent heat for vaporization obtained by partitioning the total energy from the energy balance equation. For example, to get the total water loss in mm per hour, the evaporative fraction (EF) would be multiplied by the net

hourly radiation times the time interval (3600 seconds = 1 hour), divided by the latent heat of evaporation, giving water loss in gram per day which is then converted to water loss in mm.

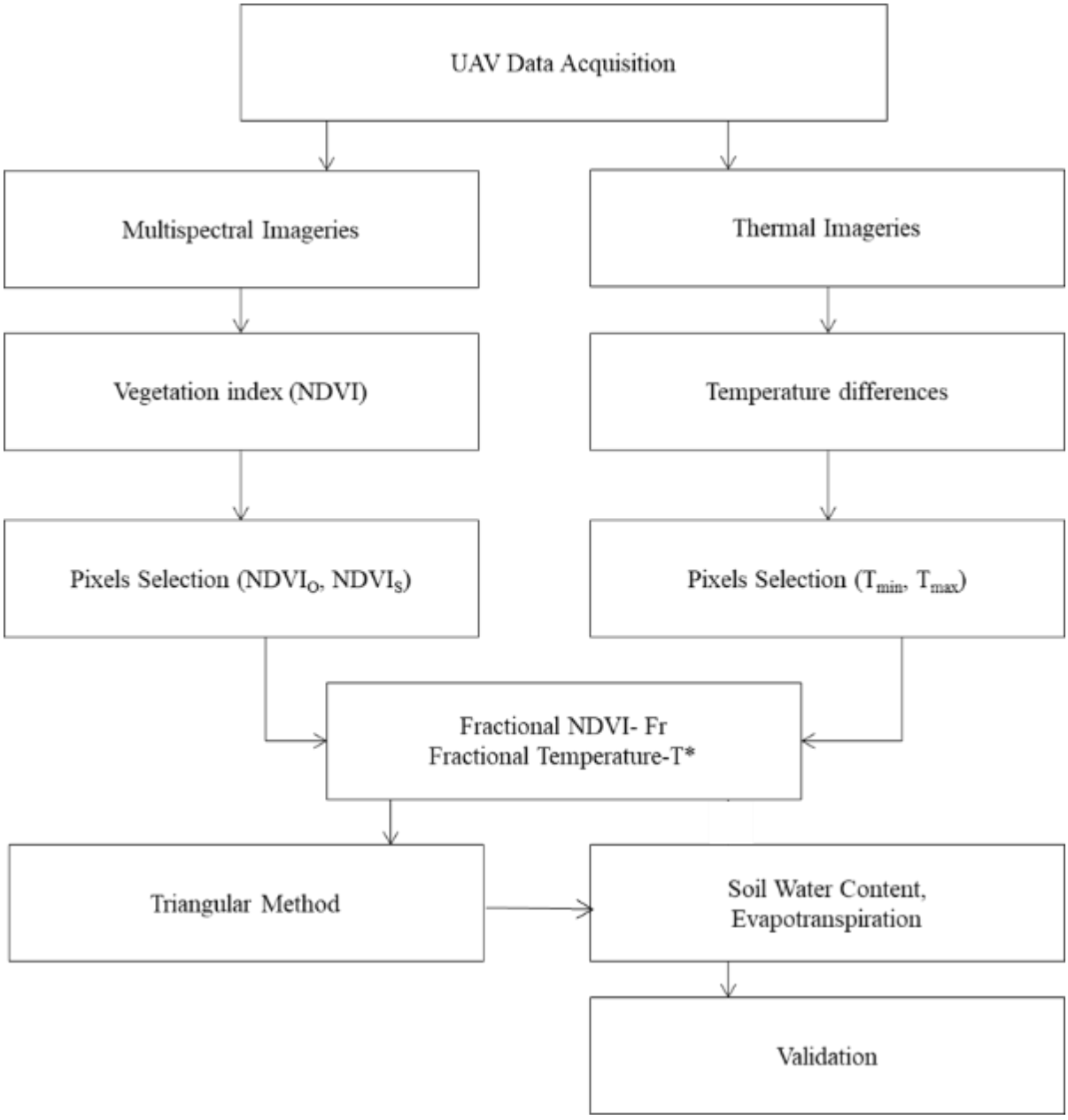

Figure: 3.19: Schematic chat illustrating stepwise quantification of evapotranspiration.

CHAPTER FOUR
RESULTS

4.1 The Assessment of Soil Water Content using Soil Electrical Conductivity

4.1.1 Spatial distribution of electrical conductivity use in determining soil water content

To map and establish soil electrical conductivity variability maps presented in Figures (4.1 to 4.4), an interpolation approach using inverse distance weighting was used to interpolate data obtained from the electromagnetic induction instrument (EM38). Ground soil water content measurement positions are indicated by the black points on the maps. Figure (4.1) shows the apparent electrical conductivity (ECa) spatial distribution map predicted from the first EM38 field campaign, where soil water content measurements were conducted at all soil depths (0 cm to 25 cm, 25 cm to 50 cm, 50 cm to 75 cm and 75 cm to 100 cm) for calibration purposes.

From 22 September 2020 EM38 field campaign to the last EM38 field campaign on 14 October 2020, soil water content measurements were conducted on the first layers (0-25 cm), and the measurements were utalized to quantify the variability of the spatial soil water content on other layers by calibration. The spatial variability of the soil electrical conductivity fluctuated with varying soil water content (θ) within the EM38 surveyed area of interest.

In August, the ECa values ranged between 1.1 mS/m and 11.85 mS/m, with an average soil water content of 6.63 percent. On 22 September 2020, the ECa values ranged between 5.1 mS/m and 19 mS/m at a 16.26 percent soil water content average. The results from 23 September 2020 show that the ECa readings ranged from 7.7 mS/m to 22.4 mS/m at an average soil water content of 18.77 percent, while predictions of the last campaign on 14 October 2020 showed ECa ranging from 1.1 mS/m to 18.6 mS/m with 5.33 percent average soil water content.

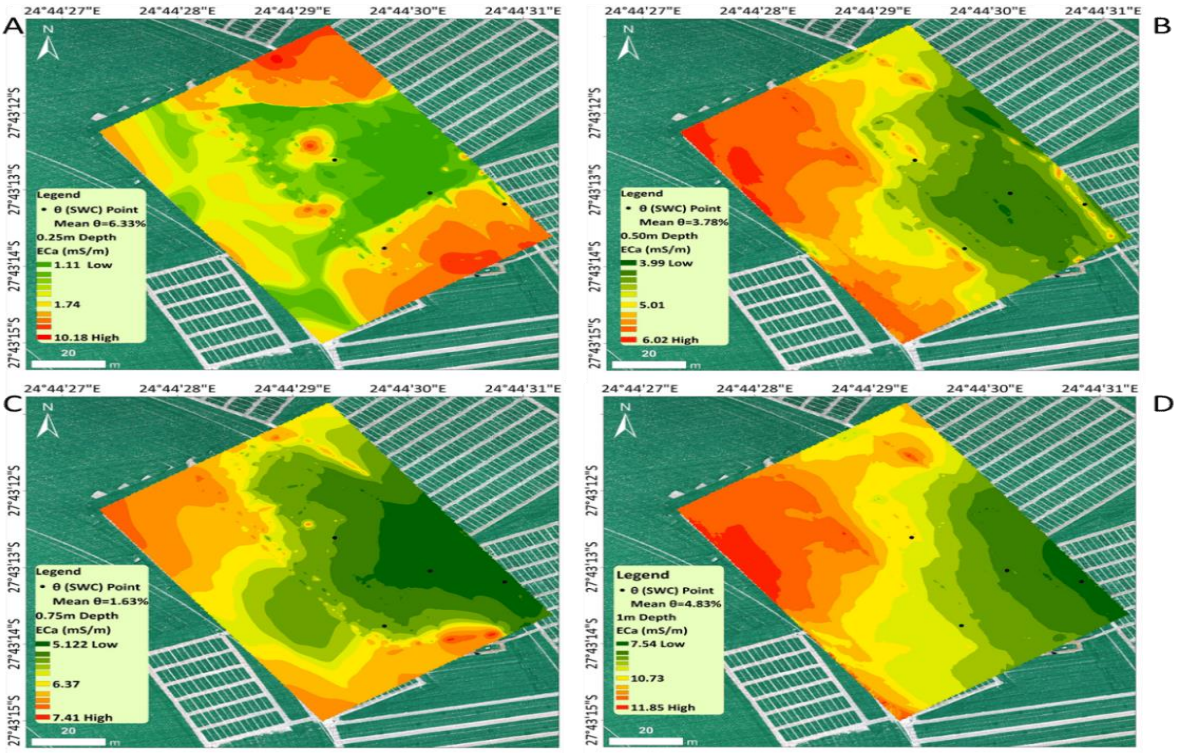

Figure 4.1: Spatial variability of soil electrical conductivity for four depths (A-D, represent top to bottom layers on 11 August 2020).

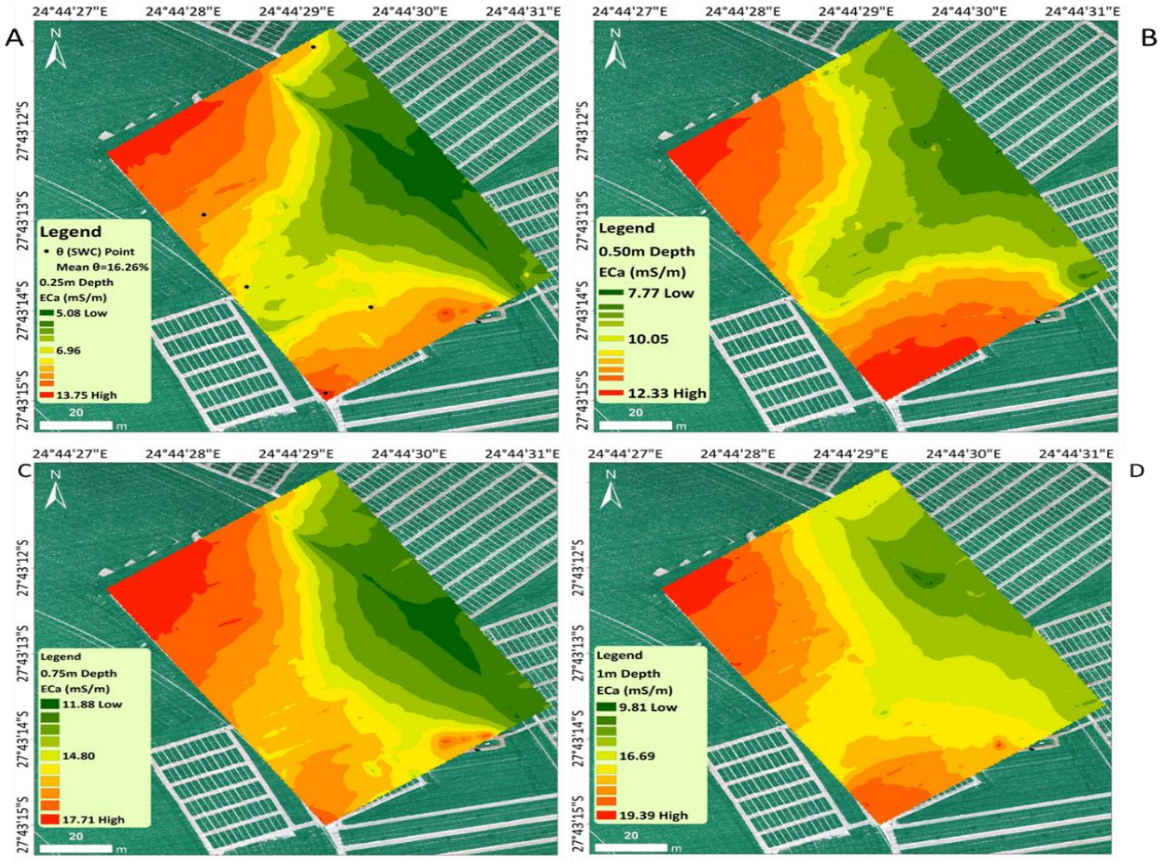

Figure 4.2: Spatial variability of soil electrical conductivity for four depths (A-D, represent top to bottom layers on 22 September 2020).

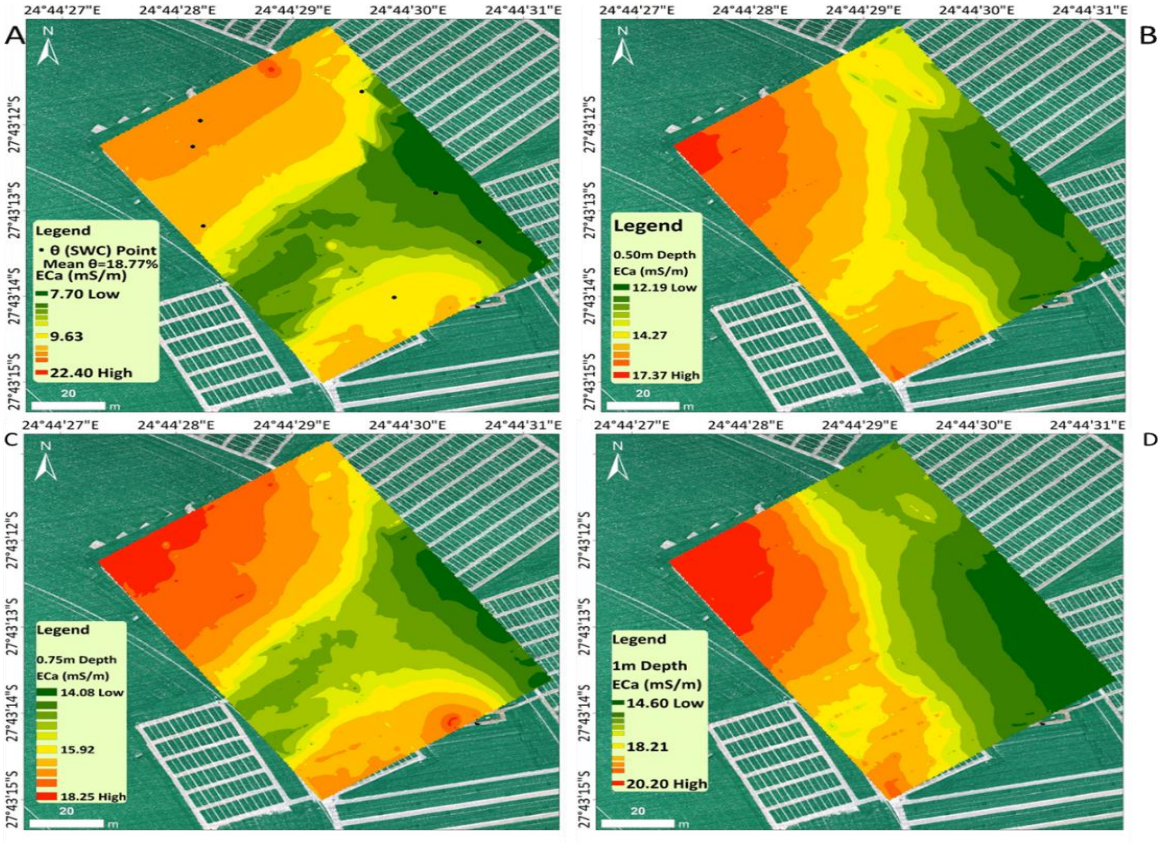

Figure 4.3: Spatial variability of soil electrical conductivity for four depths (A-D, represent top to bottom layers on 23 September 2020).

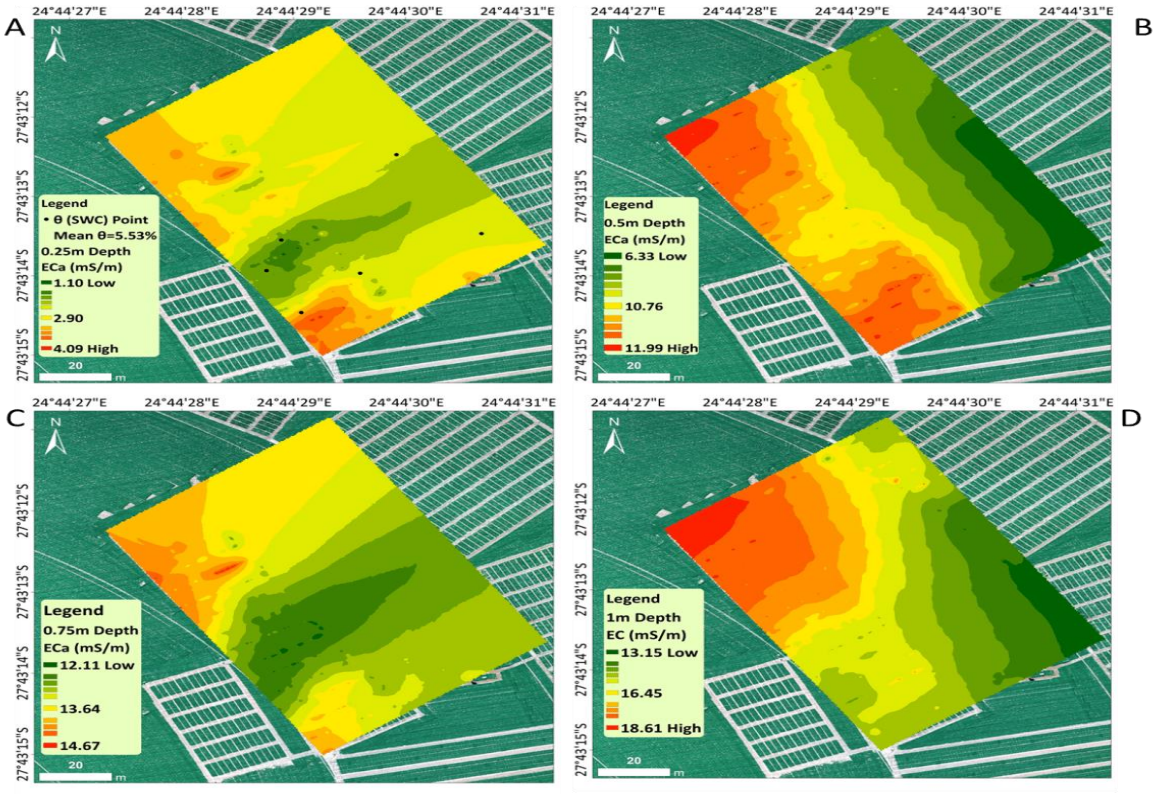

Figure 4.4: Spatial variability of soil electrical conductivity for four depths (A-D, represent top to bottom layers on 14 October 2020).

Relationship between the soil water content measured and predicted electrical conductivity.

The values extracted on the exact geographic location of measurement as the soil water content and the predicted electrical conductivity was used to determine any correlation between the two variables using linear relationships as indicated in the figure (4.5, a-d). During August 2020, the relationship between ECa and SWC was negative with a coefficient of determination R^2 of 0.85 with a correlation coefficient of -0.92. On 22 September 2020, the relationship between ECa and SWC was negative, with the R^2 value of 0.95 and the correlation coefficient of -0.98. On 23 September 2020, the relationship between ECa and SWC was positive, with an R^2 value of 0.71 and a correlation coefficient of 0.84. On 14 October 2020, the relationship between ECa and SWC showed a positive relationship with the R^2 value of 0.75 and a correlation coefficient of 0.87. For all the survey dates, the relationship between ECa and SWC portrayed a statistically significant difference of ($p \leq 0.05$). Therefore, the results show that more soil electrical conductivity was a function of soil water content.

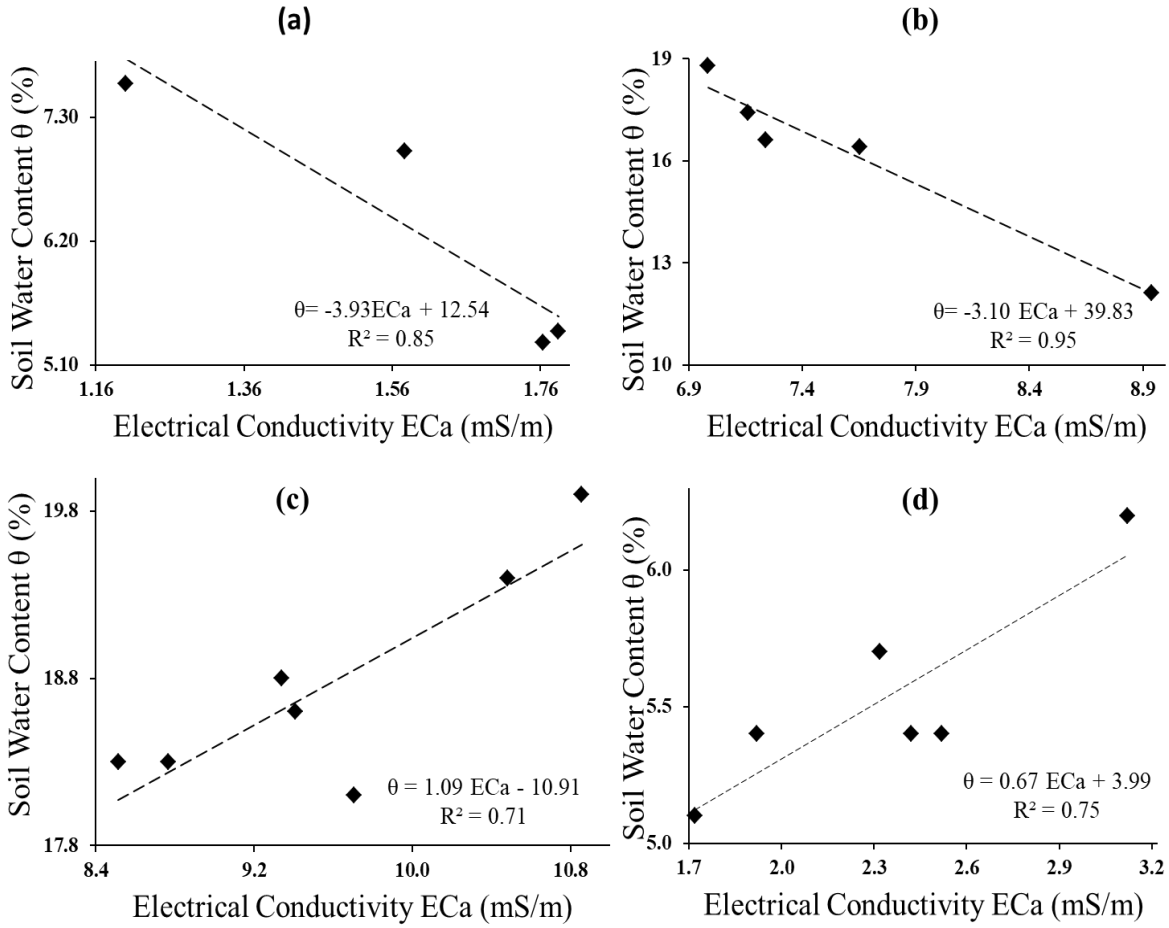

Figure 4.5: A Relationship between soil electrical conductivity and soil water content where (a to d) represent (11 August 2020; 22 September 2020; 23 September 2020 and 14 October 2020) dates of the survey.

Table 4.1: Statistical summary for the relationship between the measured soil water content and predicted electrical conductivity.

Day of the year	Model	R	P-value
11 August 2020	θ= -3.93 ECa + 12.54	-0.92	0.04
22 September 2020	θ= -3.10 ECa + 39.83	-0.98	0.02
23 September 2020	θ = 1.09 ECa - 10.91	0.84	0.05
14 October 2020	θ = 0.67 ECa + 3.99	0.87	0.04

Relationship between in-situ soil electrical conductivity and in-situ soil water content.

The relationships between the in-situ soil electrical conductivity taken using EC meter and soil water content measured using amplitude domain reflectometry soil moisture (ADR) probe at different soil depths and different soil sampling points are displayed in figure (4.6, a-d).

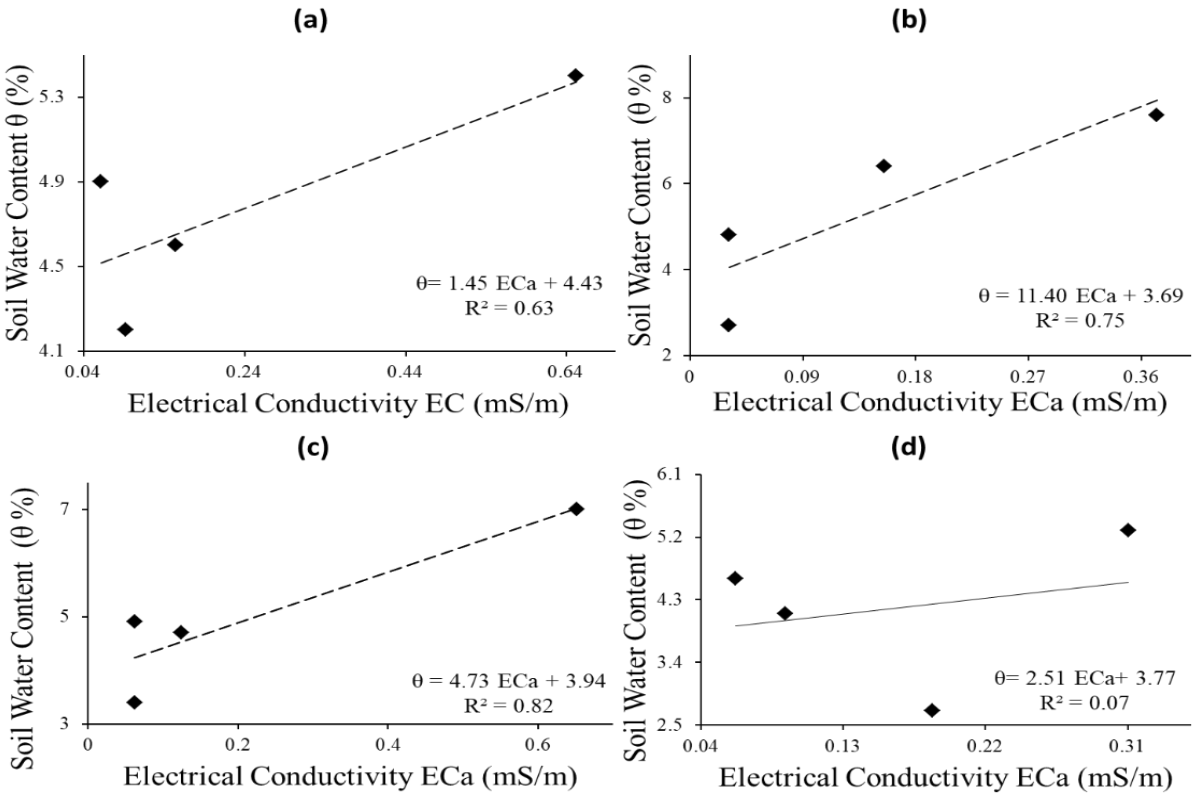

Figure 4.6: Pair relationship between in-situ soil electrical conductivity and soil water content at varying soil depths at sampled locations.

The Relationship between soil electrical conductivity and soil physiochemical properties.

A correlation matrix was developed to evaluate the influence of soil properties on electrical conductivity (ECa) and (ECe) readings, as indicated in Table 4.2. The table shows a very low correlation between ECe, magnesium (mg) and calcium (Ca), with a moderate correlation positive correlation between ECe, sodium (Na) and potassium (K). Soil pH and ECe showed a relatively strong negative correlation. The correlation between ECa and physiochemical properties appears to be low.

Table 4.2: Correlation matrix of soil physiochemical properties and extractable cations with electrical conductivity ECa and Ece.

	pH	Ca	Mg	K	Na	Ece	SOM	ECa
pH	1.00							
Ca	-0.28	1.00						
Mg	-0.01	0.03	1.00					
K	-0.31	0.75	0.43	1.00				
Na	-0.13	0.41	0.52	0.77	1.00			
Ece	-0.70	0.14	0.41	0.52	0.61	1.00		
SOM	0.51	0.18	-0.16	0.03	-0.02	-0.48	1.00	
ECa	-0.08	0.37	-0.56	0.07	0.05	0.03	-0.13	1.00

4.1.2 Soil electrical conductivity conversion to soil water content

Soil water content spatial distribution maps were generated by applying the developed model from the relationship of soil water content with the soil electrical conductivity on spatial distribution maps (see Figure 4.7). The predicted soil water content was given as percentages. Soil water content fluctuated within the geographical extent of the selected EM38 survey area. The soil water content variations varied with the survey dates, which shows varying ranges based on the irrigation events.

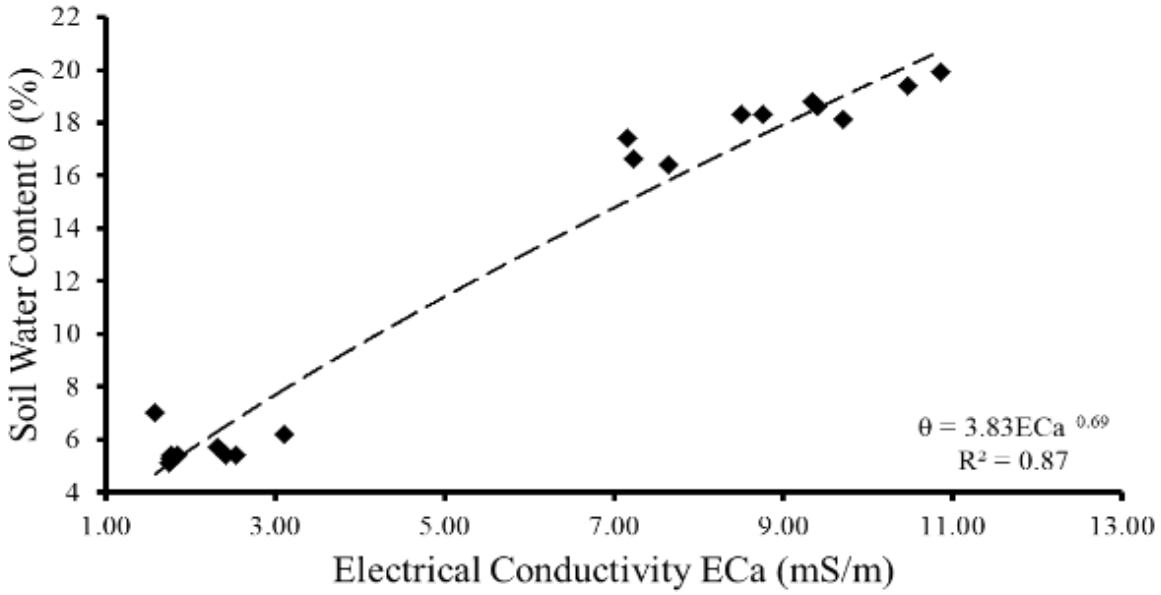

Figure 4.7: Showing a model used to convert ECa to soil water content (θ).

4.1.3 The Spatial distribution of soil water content

On 8 August 2020, the predicted soil water content ranged between 4.15 % on the top layer and increased up to 27.82 percent at the bottom layer. The amount of soil water content in soil was lower on the first layer, increasing with depth (see Figures 4.8 to 4.11). The soil water content predicted on 22 September 2020, ranged between 13.85 and 39.85 percent, and soil water content increased with an increase in depth.

On the following day 23 September 2020, soil water content predicted ranged between 5.26 and 39.85 percent, which increased around the upper soil layer to the bottom layer. On the last campaign conducted on 14 October 2020, the predicted soil water content ranged between 4.34 and 38.58 percent, indicating a rise in soil water content percentage increasing also with depth. For all the field campaigns, predicted soil water content depicted that the topsoil in the root zone contained less water than the bottom soil.

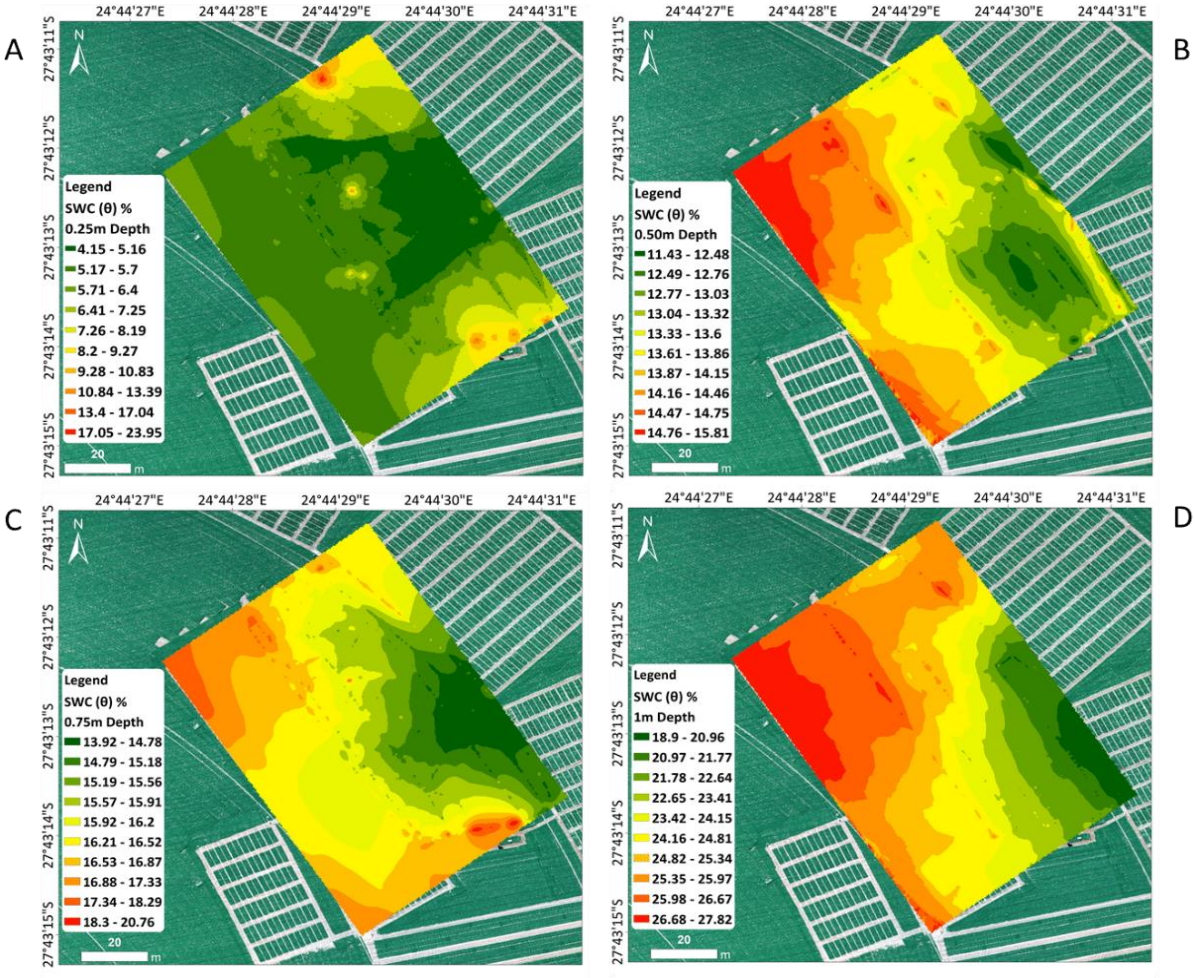

Figure 4.8: Predicted θ at four depths (A-D represents 0.25 m to 1 m on 8 August 2020).

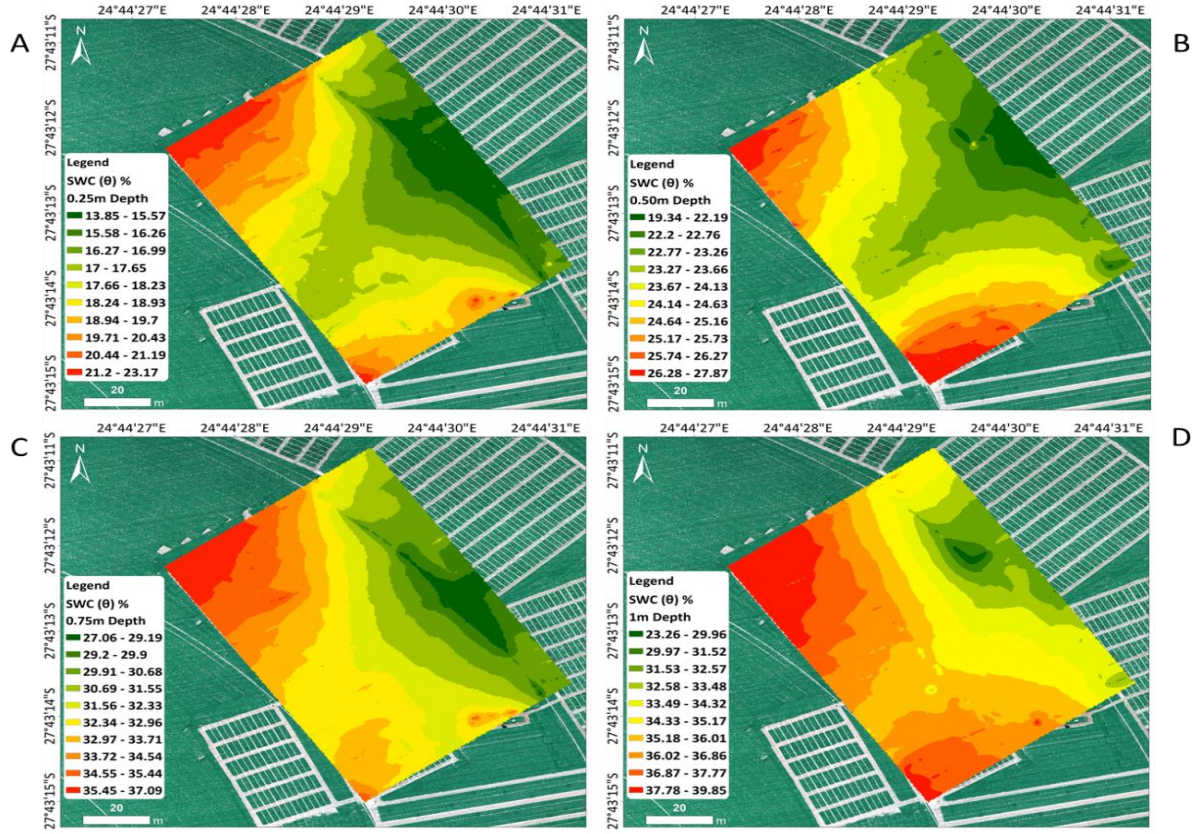

Figure 4.9: Predicted θ at four depths (A-D represents 0.25 m to 1 m on 22 September 2020).

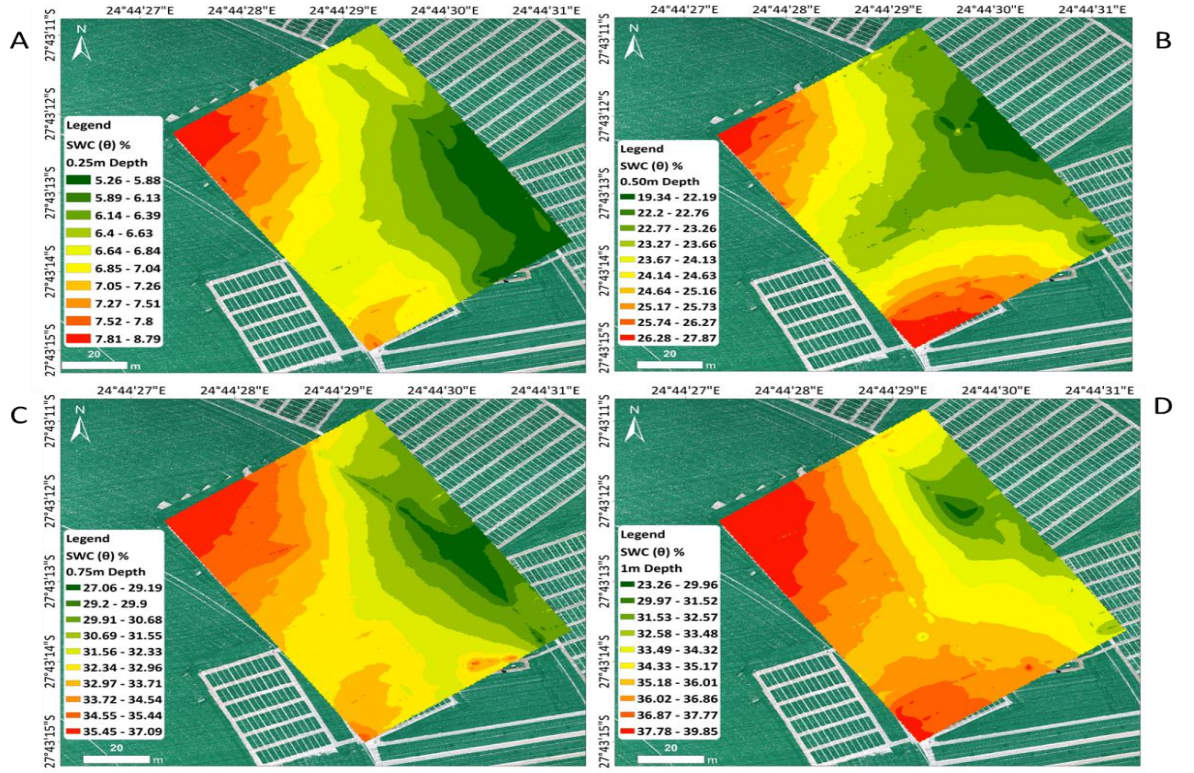

Figure 4.10: Predicted θ at four depths (A-D represents 0.25 m to 1 m on 23 September 2020).

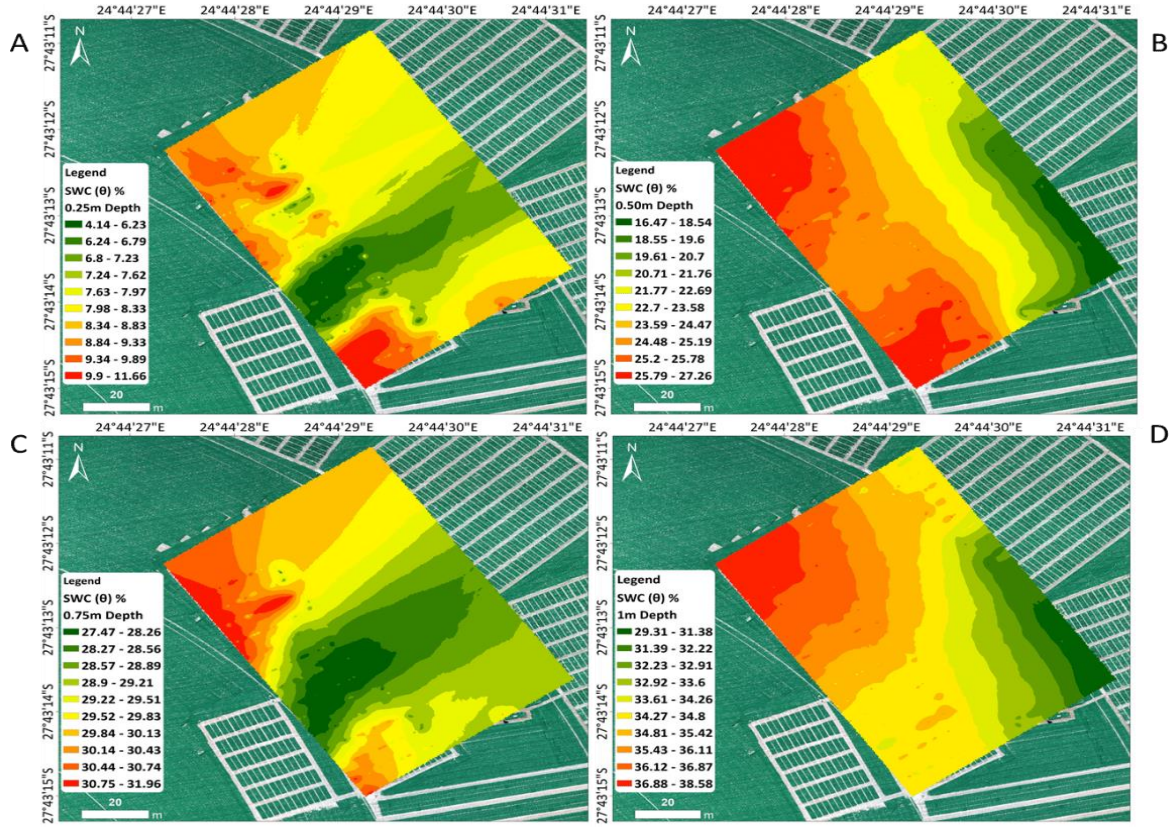

Figure 4.11: Predicted θ at four depths (A-D represents 0.25 m to 1 m on 14 October 2020).

4.2 Irrigation events

Figure 4.12 below shows soil water content throughout the barley cropping season obtained from a DFM soil water content probe. The upward spikes indicate a rise in field soil water content during irrigation events. Conversely, a decline in spike gradient depicts soil water content drawn down through crop water use, evaporation and infiltration. Soil water content in the figure below was measured from 0 m-0.8 m in depth.

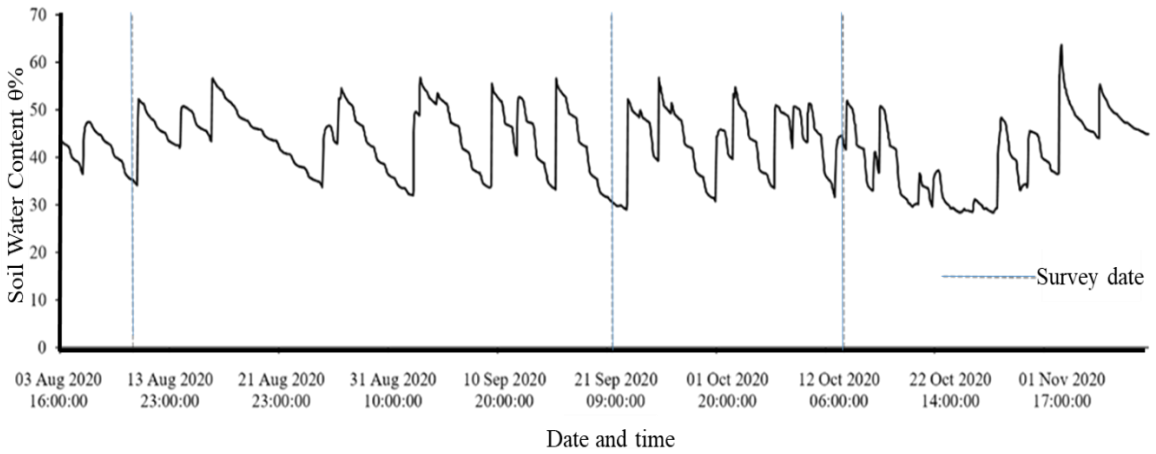

Figure 4.12: Soil water content depicting irrigation occurances.

The quantity of water given to the crop before each EM38 survey is given in Table 4.2 below, including the date and time of each survey campaign. In most irrigation dates, 10 mm drops were given to crops while a 3 mm amount was given during fertigation.

Table 4.3: Irrigation and EM38 survey date with time included the amount of water irrigated throughout the season.

Irrigation date and time	Survey date and time	Water irrigated	Condition
05 August 2020/14:00	11 August 2020/ 15:00	10 mm	Dry
21 September 2020/08:00	22 September 2020/15:00	10 mm	Wet
23 September 2020 /12:00	23 September 2020/ 16:00	3 mm	Wet
12 October 2020/21:00	14 October 2020/ 16:00	10 mm	Wet-Dry

4.3 Actual Evapotranspiration Estimation from Smart Field Weighing Lysimeters

Variation in actual evapotranspiration fluxes on an hourly basis for selected rainless and non-irrigated days is shown in Figures (4.13 to 4.15). Evapotranspiration was high primarily during the daytime. The total evapotranspiration per day is displayed for each lysimeter for the assessed days. Evapotranspiration estimated from the lysimeters on 10 August 2020 ranged between 0 mm hr^{-1} and 1.2 mm hr^{-1} with total evapotranspiration of 3.82 mm day^{-1} in lysimeter one and 5.01 mm day^{-1} in lysimeter two.

On 22 September 2020, daily evapotranspiration ranged about 0 mm hr^{-1} and 1.1 mm hr^{-1} amounting to a total of 7.66 mm day^{-1} and 3.27 mm day^{-1} for lysimeter one and two, respectively. For both lysimeters on 14 October 2020, a total of 7.93 mm day^{-1} and 6.26 mm day^{-1} evapotranspiration was estimated with hourly evapotranspiration ranging about 0.02 mm hr^{-1} and 0.9 mm hr^{-1}.

Soil mean soil water content in percentage for both lysimeters is portrayed in the figures representing evapotranspiration estimated by the lysimeters. Maximum crop water use was observed in August at 1.2 mm, followed by 1.02 mm observed in October and 0.9 mm recorded in September.

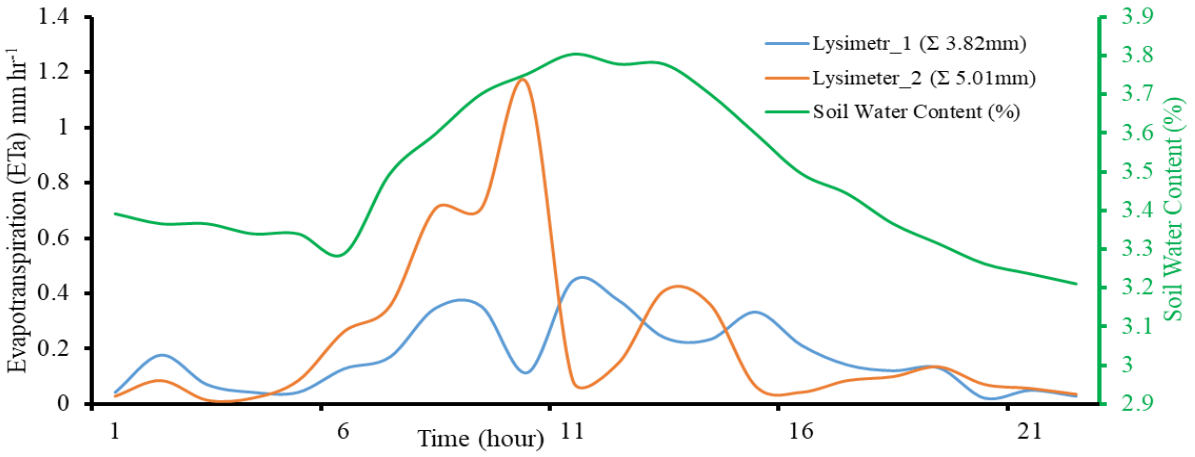

Figure 4.13: Evapotranspiration from lysimeters on the 10th of August 2020.

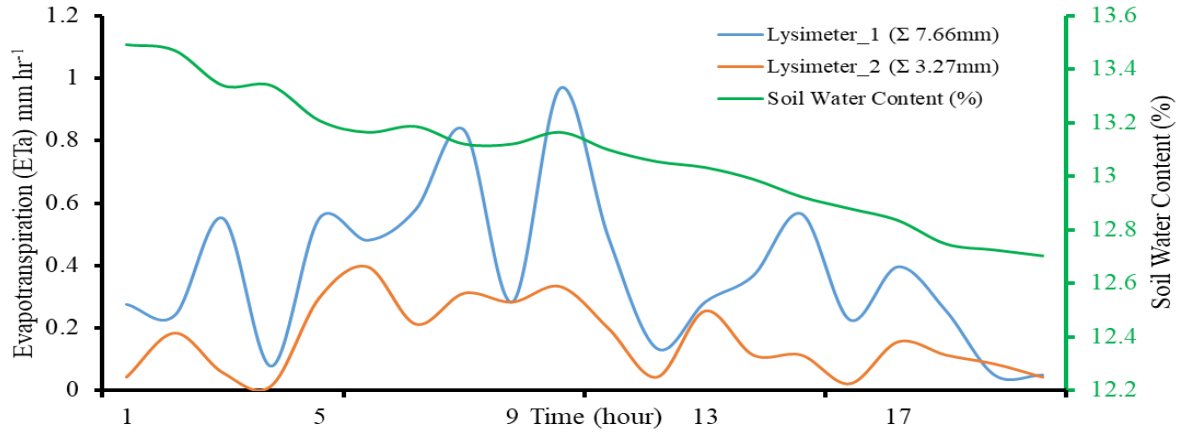

Figure 4.14: Evapotranspiration from lysimeters on the 22 September 2020.

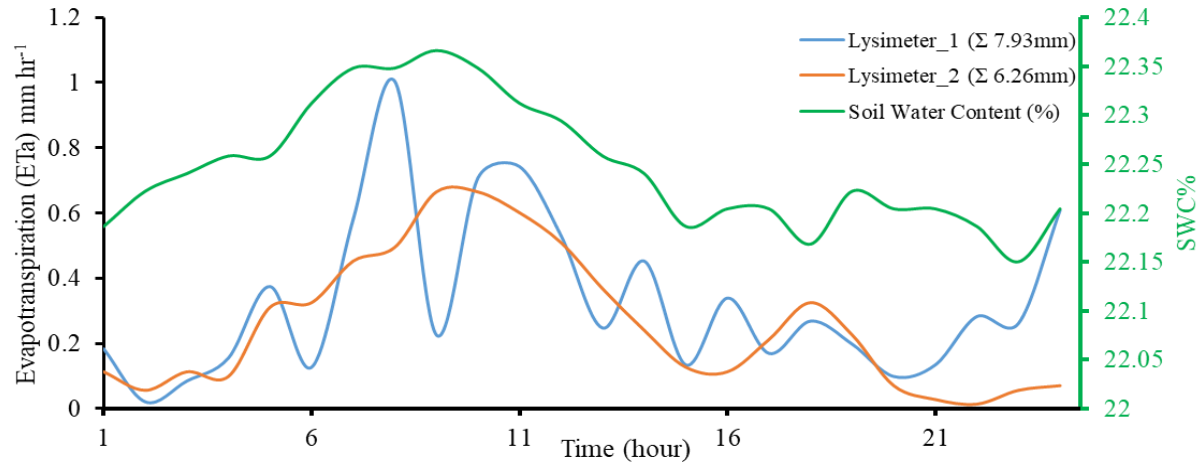

Figure 4.15: Evapotranspiration from lysimeters on the 14th of October 2020.

4.3.1 Evaluation criteria

Evapotranspiration estimation from the lysimeters was validated using the soil water content changes recorded from the moisture sensors within the lysimeters at three depths. Evapotranspiration and soil water content showed patterns in agreement as changes occurred.

Statistical analyses were used to evaluate the relationship between the crop evapotranspiration and the field soil water content given in the table below.

Table 4.4: Statistical relationship between field soil water content and evapotranspiration.

Date	r	P_value
10-Aug-2020	0.81	P<0.001
22-Sep-2020	0.51	P<0.011
14-Oct-2020	0.85	P<0.001

4.4 Reference Evapotranspiration Estimation from weather data

Utilizing the data from an automatic weather station located 10 meters from the smart field lysimeters, the reference evapotranspiration was quantified using the Penman-Monteith approach and Priestly-Taylor method. The aim of computing reference evapotranspiration from two methods was to evaluate the estimation accuracy for one method by another as they use different albedo values.

Figure 4.16 below shows daily reference evapotranspiration between August and 20 October 2020. The reference evapotranspiration ranged between 9.02 mm and 9.63 mm per day from the Penman-Monteith technique while for the Priestly-Taylor method, reference evapotranspiration ranging between 6.97 mm and 7.46 mm per day.

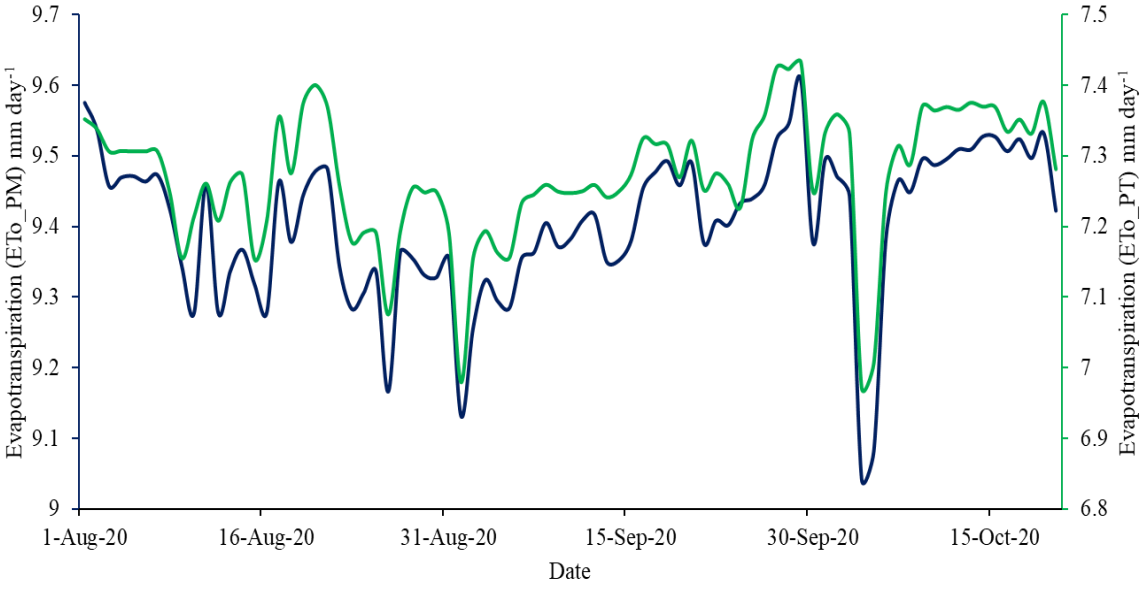

Figure 4.16: Reference evapotranspiration estimation using Penman-Monteith (Blue) and Priestly-Taylor (Green) methods between August 2020 and 20 October 2020.

4.4.1 Reference evapotranspiration evaluation

To evaluate the reliability of Penman-Monteith reference evapotranspiration estimation, the Priestly-Taylor method was used to quantify the reference evapotranspiration for the same days. A Pairwise relationship analysis was performed using linear regression analysis for the reliability of weather data evaluation in quantifying ET_0 (see Figure 4.17). A high coefficient of determination (R^2) value of 0.89 was obtained with a high significance difference ($P \leq 0.001$), a correlation coefficient (r) of 0.94.

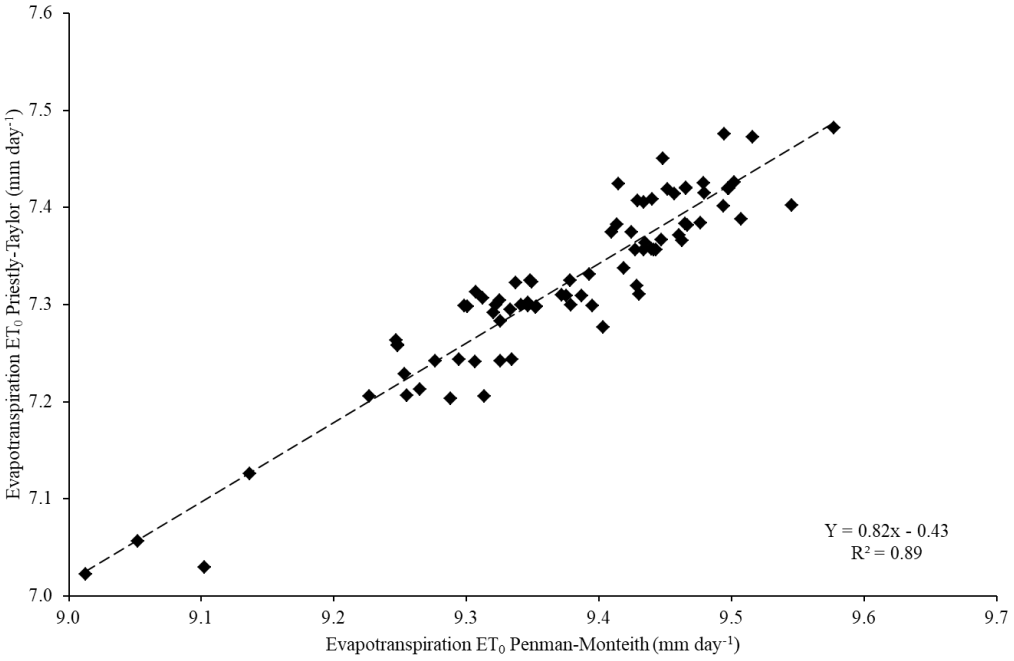

Figure 4.17: Relationship between reference evapotranspiration estimated from Penman-Monteith and Priestly-Taylor methods.

4.4.2 Comparison between actual evapotranspiration (ETa) and Reference Evapotranspiration (ET_0)

The daily reference evapotranspiration ET_0 for rainless and days with no irrigation was computed using an automatic field weather station situated 10 m away from the two smart field-weighing lysimeters, applying the Penman-Monteith formulas shown in chapter three. The actual evapotranspiration estimated from lysimeters was averaged into a single value for each day. ET_0 and ETa values were then compared using simple linear regression to assess the statistical significance (see Figure 19). Figure (4.18) shows a series of daily reference and actual evapotranspiration for the selected days. Between 21 August 2020 and 3 September 2020, ETa had dropped sharply when ET_0 increased sharply. Such occurrences might be

attributed to low soil moisture around the barley crop not being sufficient for total evapotranspiration. On most occasions, ET_0 increased with an increase in ETa mainly after irrigation events when soil moisture was higher for fewer days, which was sufficient enough to trigger evapotranspiration. On 22 September 2020, ET_0 dropped close to ETa due to soil surface dryness.

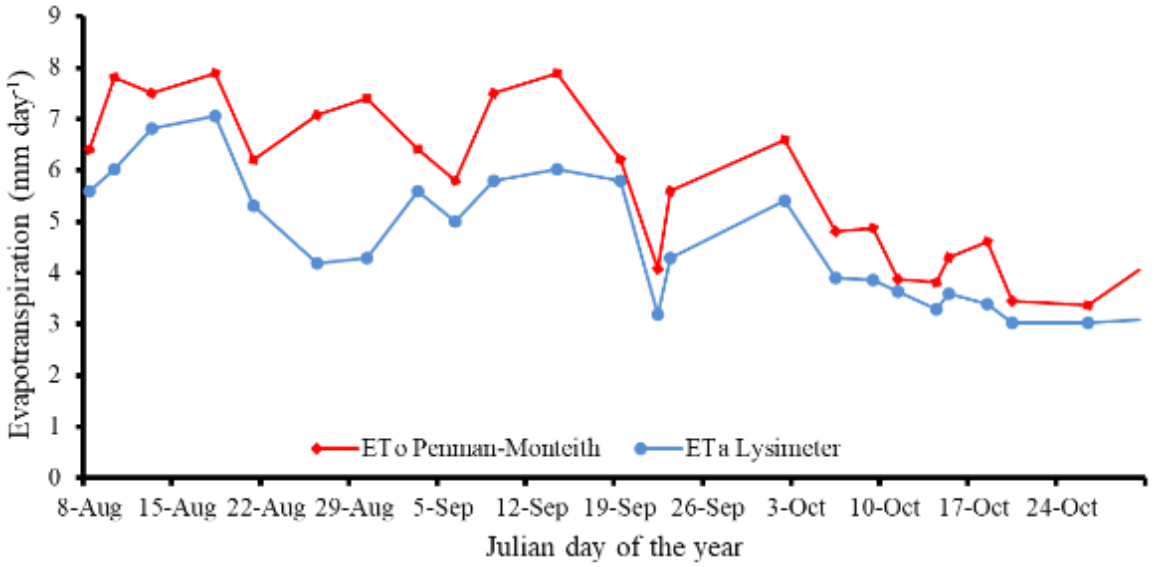

Figure 4.18: Showing daily evapotranspiration fluxes from lysimeters and weather data.

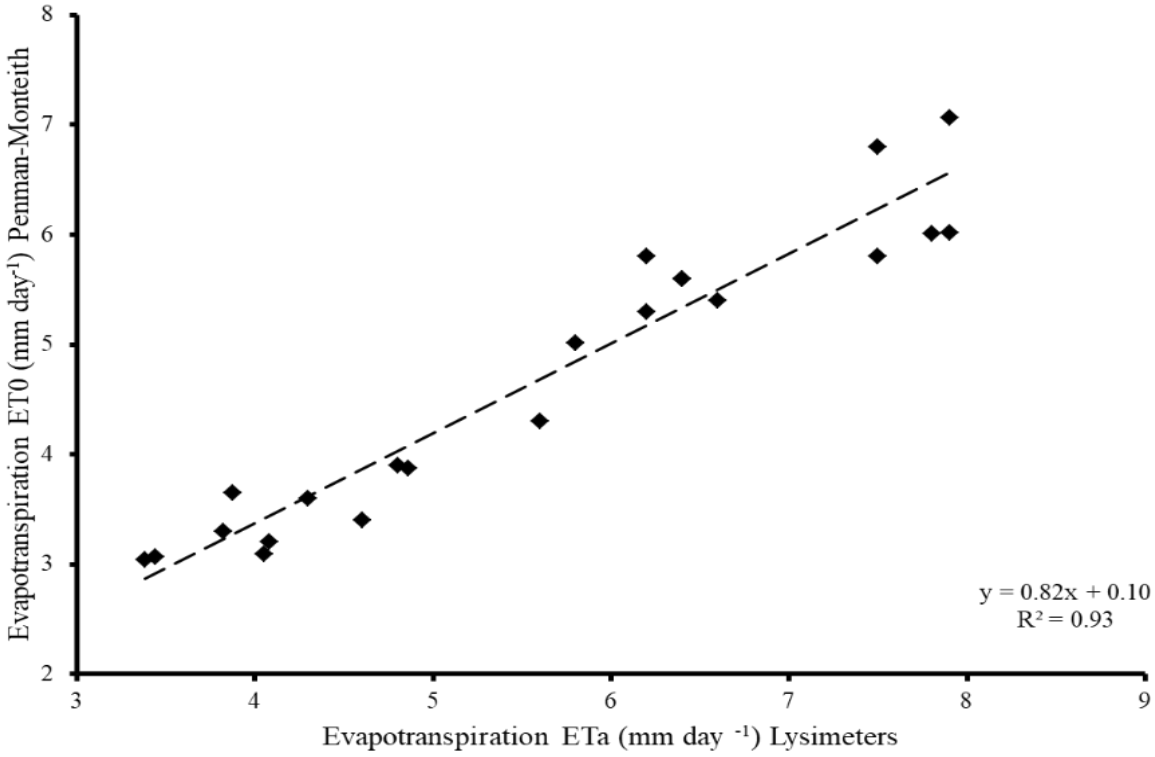

Figure 4.19: The relationship between actual and reference evapotranspiration.

4.5 The Capabilities of Unmanned Aerial Vehicle (UAV) Data in Estimation of Evapotranspiration and Soil Water Content

Estimation of evapotranspiration and soil water content using a multispectral and thermal unmanned aerial vehicle (UAV) in this section was established using a triangular algorithm remote sensing method. The choice for this method was based on the fact that sensitivity to atmospheric conditions, surface conditions and net radiation, as stated by Carlson (2020), is extremely low. The triangular method is based on surface energy balance and the main process is that surface radiant temperature changes depend on the content of surface water available, either on soil or crop canopy. The method in this study made use of multispectral images shown in Figure (4.20) to compute vegetation indices. The index computed in the study was the normalized difference vegetation index (NDVI) shown in Figure (4.21). The NDVI maps were used to derive fractional vegetation cover maps shown in Figure (4.22). Thermal images were taken at the exact flight plan campaigns, as multispectral data, to establish radiant surface temperatures within the field. Image pixels were selected over bare soil surfaces, dense vegetation surfaces and low vegetation density surfaces from both temperature and fractional vegetation images. Pixel values were extracted from both images as indicated in Figure (3.20) and the relationship between the pair was established. The method was applied to three UAV campaigns conducted on 10 August 2020, 22 September 2020 and 14 October 2020. Figure (4.20) shows the multispectral UAV images for different campaigns that show different phenological stages. It is evident from image-A that the crop was in ears development with low canopy cover, depicted by light patches and lines of bare soil. The central image-B of Figure (4.20) shows a full canopy cover on the soil patches evident in image-A with lodging starting to show up; Image-C shows lodging in most parts.

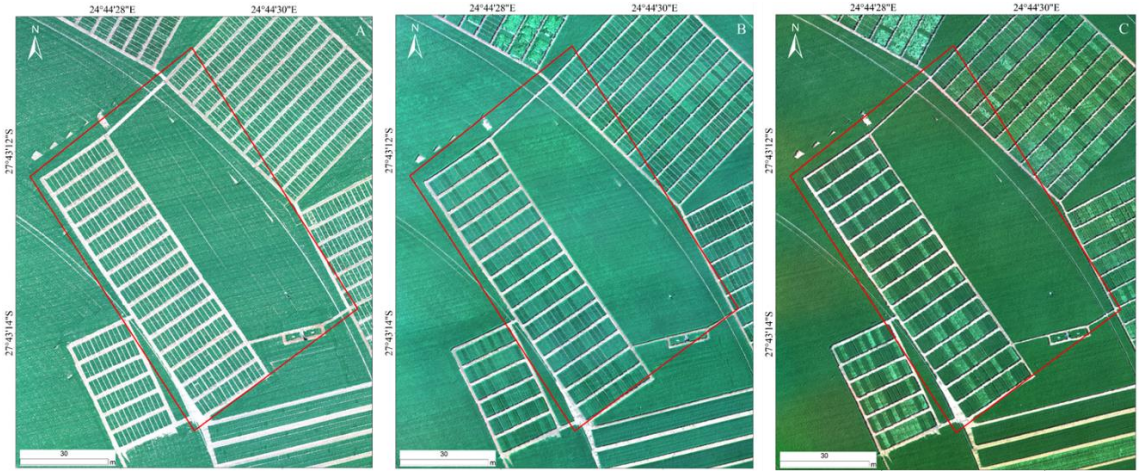

Figure 4.20: Showing multispectral composite for different phenological stages, labels (A-C) represent; August, September and October 2020 survey days.

Computations of Normalized Difference Vegetation Index (NDVI) for the three varying phenological stages are presented in Figure (4.21) labelled A-C. Image (A) represents the NDVI status during the early development growth stage ranging between 0.03 and 0.75. The mixing of pixels in this stage is more evident because the canopy cover does not shield much of the soil surrounding each crop. During the September month in the image (B), the NDVI values were observed to have increased ranging between 0.08 and 0. 86.

The increase was due to an increase in canopy cover when more crop eyes were developing. The percentage of bare soil pixels in this stage was reduced. The last observations were made in October, as shown in image (C), showed a slight decline in NDVI values ranging between 0.02 and 0.84. The reduction in NDVI values was due to the initial stage of barley drying because it had reached its maximum productivity.

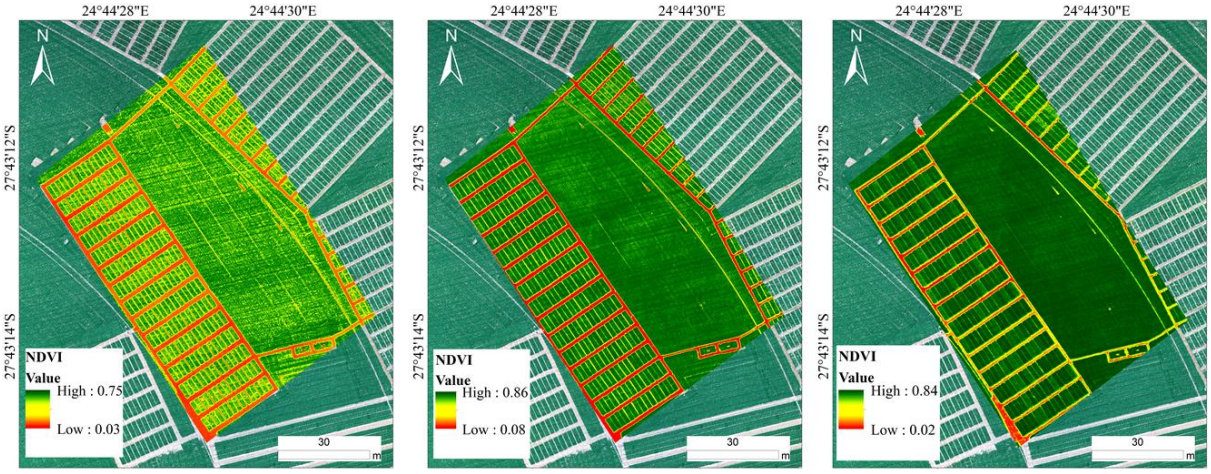

Figure 4.21: Normalized Difference Vegetation Index (NDVI) for different phenological stages, labels (A-C) represent; August, September and October 2020 survey days.

Thematic maps indicating fractional vegetation cover derived from NDVI maps are displayed in Figure (4.22) below. The fractional vegetation cover for the early crop development stage is indicated with the label (A), which corresponds with the image (D). A mix of vegetation and soil patches is evident from the fractional vegetation map.

The central map labelled (B) shows the crop's mid-season growing stage, which corresponds to the image (E), where patches of soil have disappeared because of the canopy filling the open spaces. The last map, indicated as (C), shows the late stages of development when the crop had developed grains and lodging because of production weight during windy days and heavy irrigation or rain.

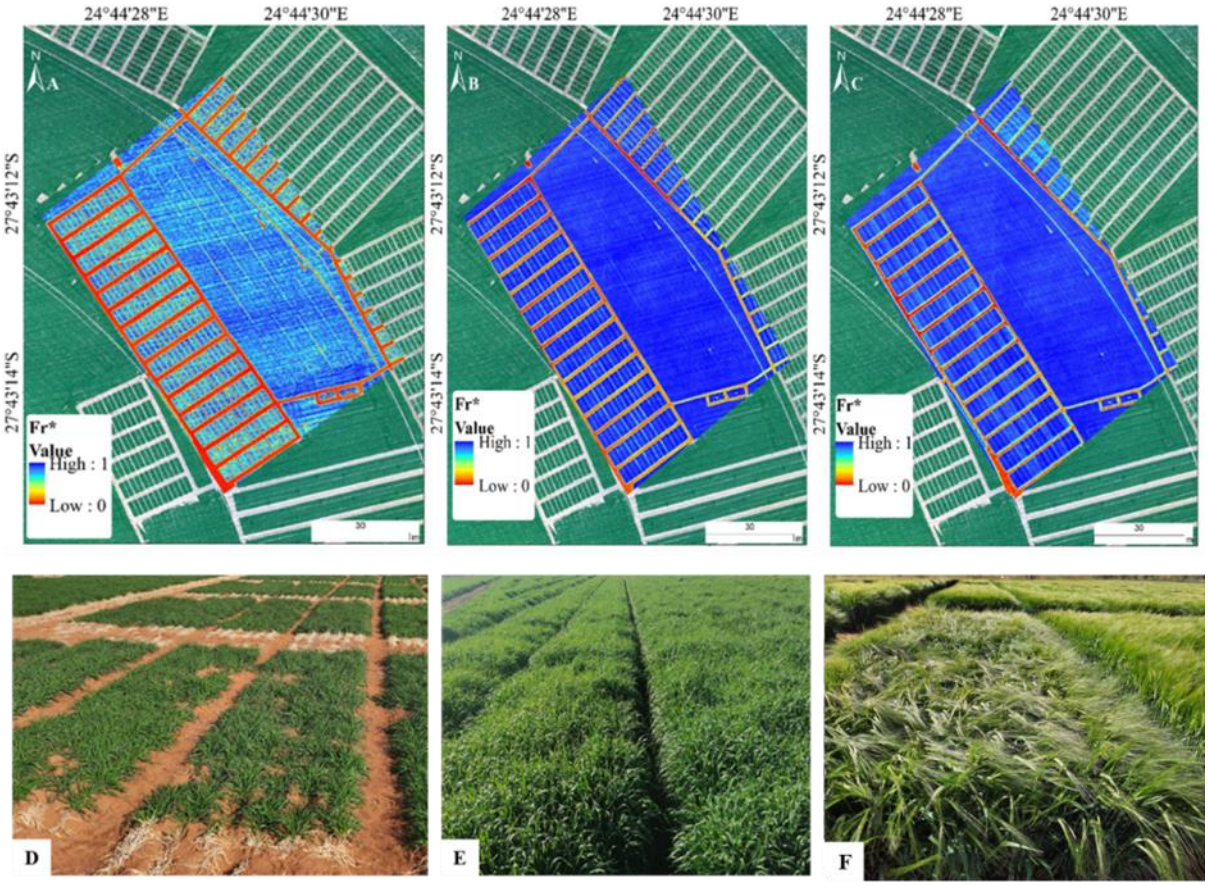

Figure 4.22: Showing fractional vegetation cover at three phenological stages, labels (A-C) represent; 10 August, 22 September and 14 October 2020 survey days, while D-F represents the same days of the images above them.

The scatterplots shown in Figure (4.23) labelled A-C show the relationship between selected UAV radiant temperature (T*) and the field fractional vegetation cover (Fr*) pixels. All points shown represent pixels covering the three types of land surface cover; a fully vegetated surface, bare soil surface and a surface containing vegetation cover, with soil patches plotted against the temperature measured during a particular time of the day. The red line shows the boundary limit of all high-temperature pixels, which corresponds to the dry or warm edge.

By contrast, the green line denotes the pixels with low temperatures associated with the wet or cold edge. The cold and warm edges were computed from a string of low and high temperatures, respectively, using a linear regression model. The triangle's top vertex represent pixels extracted from full vegetated surfaces with low temperatures. At the same time, the central part shows pixels covered with vegetation containing soil patches with moderate temperatures and the lower vertex shows pixels of bare soil with high temperatures.

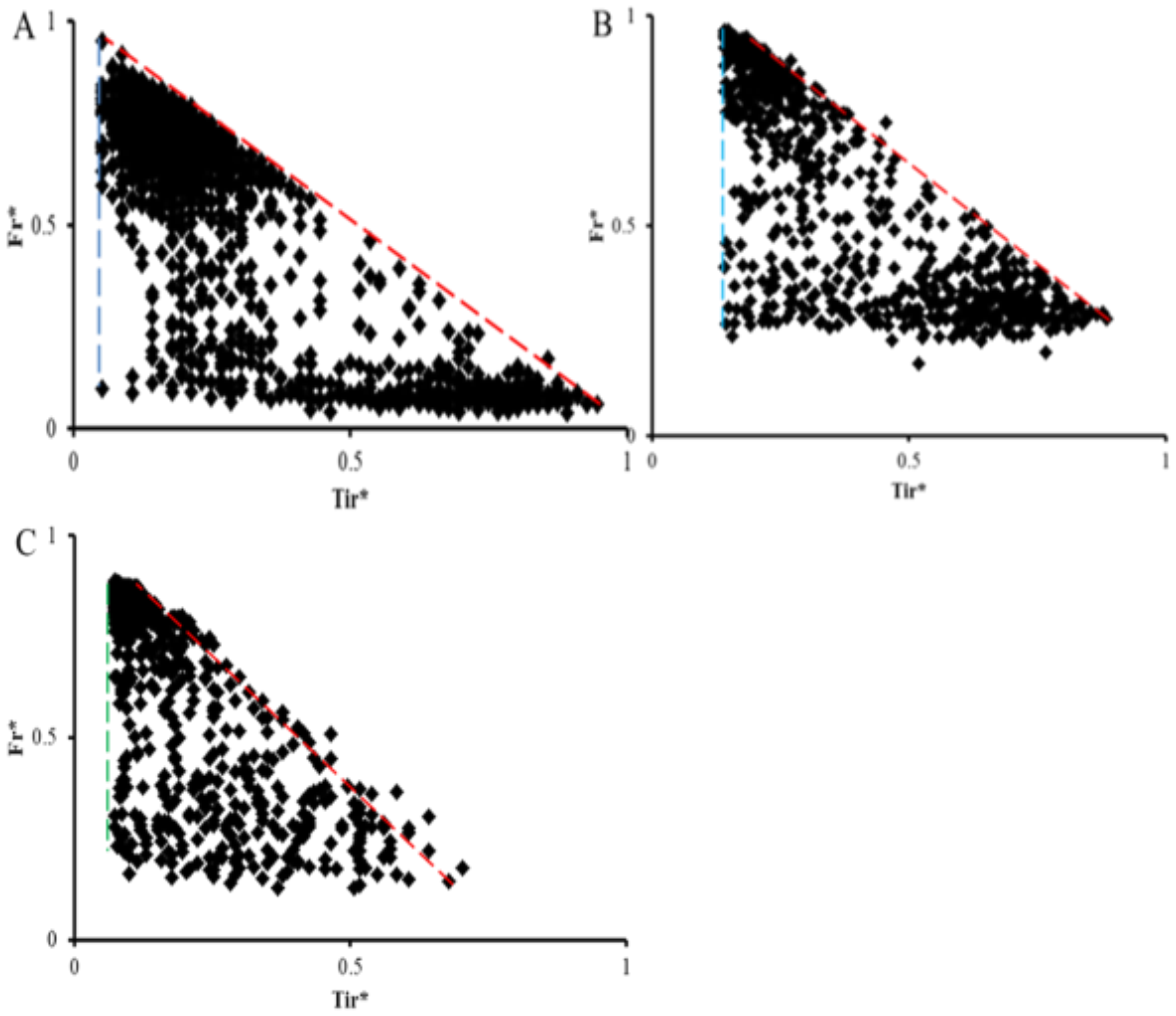

Figure 4.23: Showing vegetation-temperature relationship derived triangles, labels (A-C) represent; August, September and October 2020 survey days.

Estimation of soil moisture index (Mo)

Figure (4.24) labelled (A-C) depicts the soil moisture index for different days of the year on different phenological stages. On the first image labelled (A), the moisture index looks to fluctuate spatially across the surveyed area because of the existence of mixed pixels of bare soil and barley crop. In image (B), the moisture index was observed to be higher on the vegetated area and lower on bare soil, appearing red between the green.

Similarly, to image (B), image (C) has the same trend wherein moisture index was higher in the vegetated area and lower in portions of bare soil. It must be well noted that values closer to zero represent areas where the soil was extremely dry, while values more relative to one represent extremely wet area conditions. Estimating such an index adds values in monitoring soil water content variability on the farm scale.

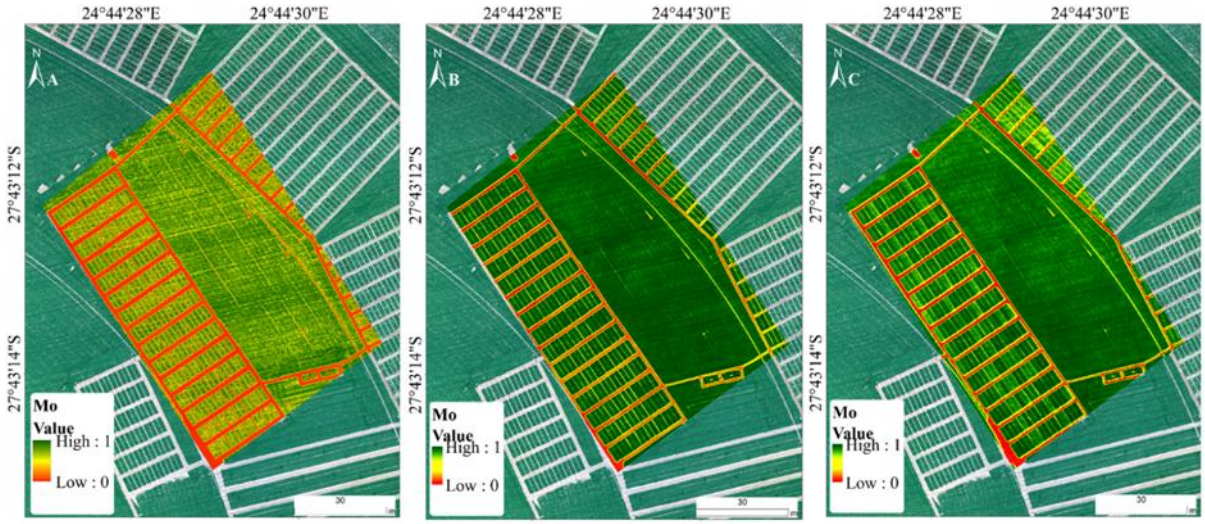

Figure 4.24: Showing moisture availability at different phenological stages, labels (A-C) represent; August, September and October 2020 survey days.

Estimation of Evaporative Fraction (EF)

The evaporative fraction maps shown in (see Figure 4.25, A-C) represent energy distribution between soil and crop vegetated area. The maps depict the proportion of the latent heat fluxes to the total amount of the latent heat at a time, and the amount of sensible heat fluxes. Image (A) shows the distribution of energy to evaporate water occurring in both soil surfaces and crop vegetated areas due to soil low vegetation cover. Image (B) shows that less evaporation occurs on bare surfaces but more in canopy cover surfaces as the crop leaves cover more soil. Image (C) shows a reduction in an evaporative fraction over the canopy surfaces due to barley crop lodging and the exposed portion of the ground.

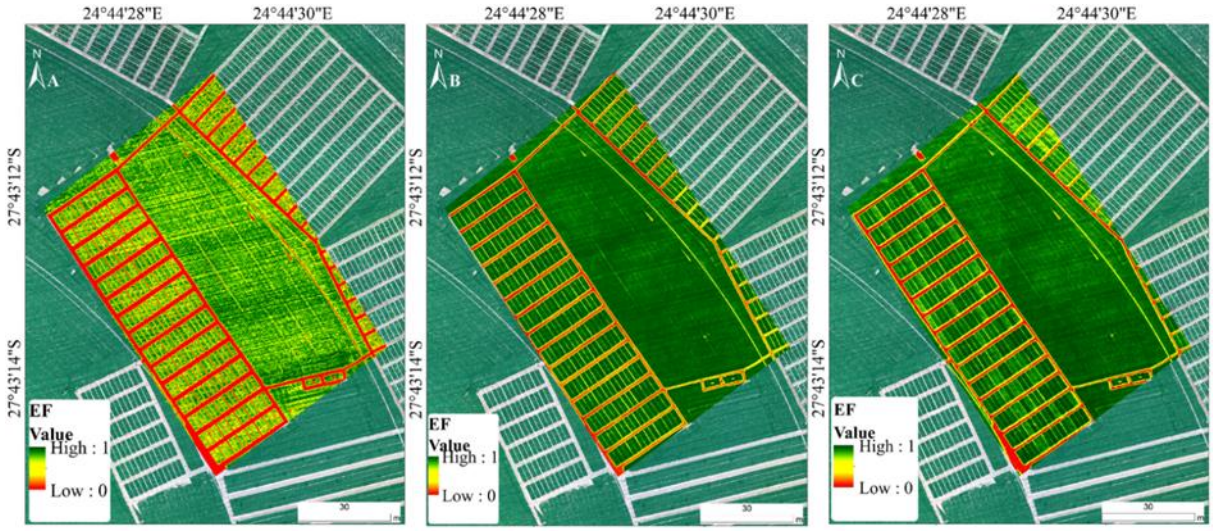

Figure 4.25: Showing evaporative fraction at different phenological stages, labels (A-C) represent; August, September and October 2020 survey days.

Evaluation criteria

As part of assessing the reliability and validation of the estimated soil water content available in the barley field, moisture index (Mo) obtained from the triangular method and in-situ soil water content were correlated. Figure (4.26 (a-c)) portrays the in-situ soil water content measurement values and the Mo values extracted on the location where in-situ measurements were done. The relationship in (Figure 4.26 (a-c)) shows a strong positive correlation with a high statistically significant difference ($P<0.001$) between the measured soil water content and the moisture index estimated from the triangular method. The observation complements the triangular method's reliability in estimating soil water content.

To assess the reliability of the triangular method in estimating evaporative fraction, the evaporative fraction was correlated with the actual evapotranspiration estimated from the smart field weighing lysimeters. Within each lysimeter, an average value of the pixels inside the 30 cm diameter cylinder collar was taken and matched with the average value of the actual evapotranspiration obtained at the same date and time with the flight dates from the two smart field-weighing lysimeters (see Figure 4.27). A positive correlation was observed with a correlation coefficient of 0.98, and the two variables are the highly statistically significant difference (p-value<0.001). This confirms the reliability of the triangular method for evapotranspiration estimation.

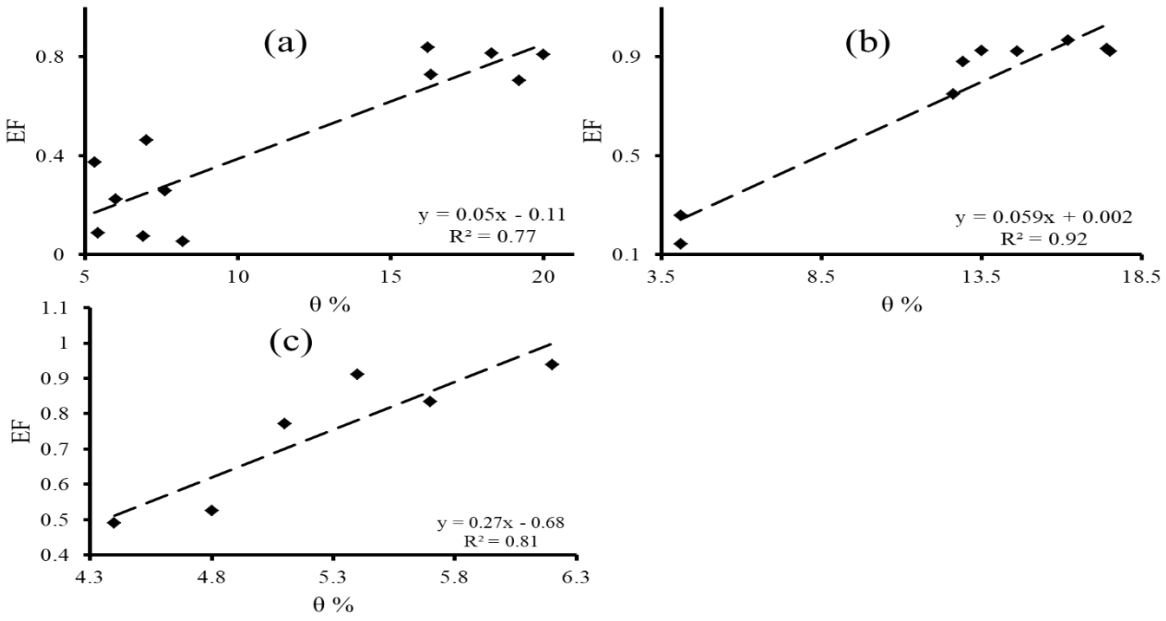

Figure 4.26: Depicts the correlation between the estimated moisture availability from the UAV-based simulated triangular method and in-situ soil water content measurements, labels (A-C) represent; August, September and October 2020 survey days.

Estimation of the spatial variability of soil water content (SWC) based on UAV data

Moisture index derived from vegetation- temperature relationship was correlated to ground-based surface soil moisture observations as indicated in the Figure (4.26). A high correlation between the two variables was observed in all the surveyed days with r>0.8 and p<0.005. Based on such observations, the inverse relationship between moisture index and ground moisture was used to derive the spatial variation of soil moisture displayed in Figure (4.27) below. From visual observations of Figure (4.27; A-C), it is evident that soil water content is higher when vegetation cover is lower during the August campaign. As fractional vegetation cover increases, the soil water content decreases; this is evident with the decrease in mean soil water content with crop growth progression. This might be because the soil surface is shielded below the barley canopy cover preventing the UAV sensors from obtaining sufficient information regarding soil water content.

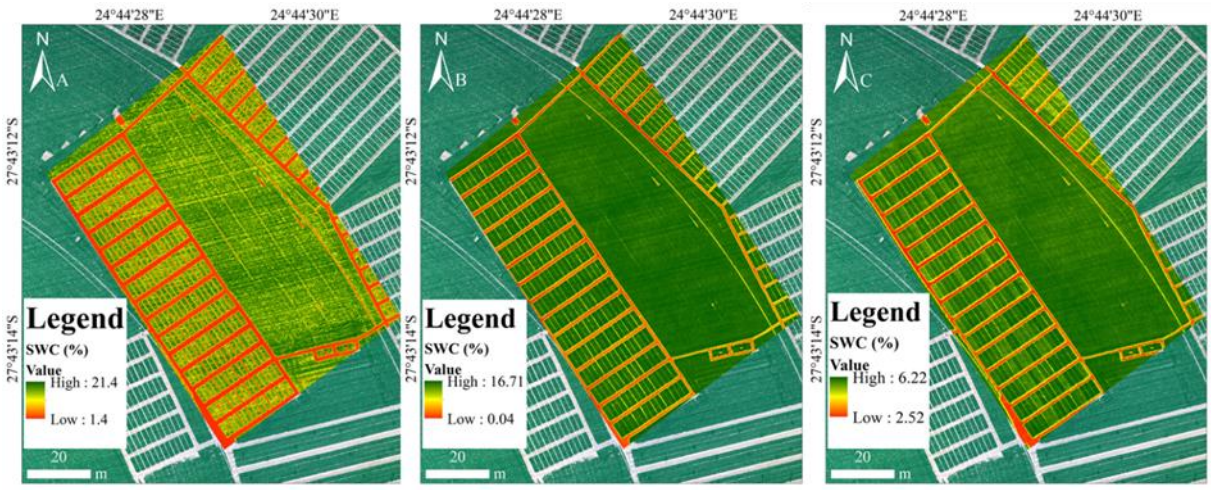

Figure 4.27: Showing the spatial variation of soil water content for different days, labels (A-C) represents; August, September and October 2020 survey days.

Estimation of spatial variability of the actual evapotranspiration (ETa) from UAV data

Estimation of the spatial distribution of the actual evapotranspiration (ETa) was obtained based on the energy balance derived equations as explained in chapter three. Hourly spatial distribution of evapotranspiration is shown in Figure (4.28) labelled (A-C), representing different days of the year. There is evidence from the images that the spatial variation of ETa was higher on image (A) and lower in image (C). Relating the variability of ETa with the soil water content shown in the last section, it can be judged that ETa increases when there is sufficient soil water content to be evaporated and transpired from the crop. The estimations are based on the total quantity of solar energy (daily net radiation), sensible heat partitioned,

and the latent heat responsible for the evapotranspiration process. It must be noted that besides soil water content, the total radiation that goes into the ground or surfaces of the crop canopy and wind which runs through the field plays a role in the rate of ETa per hour.

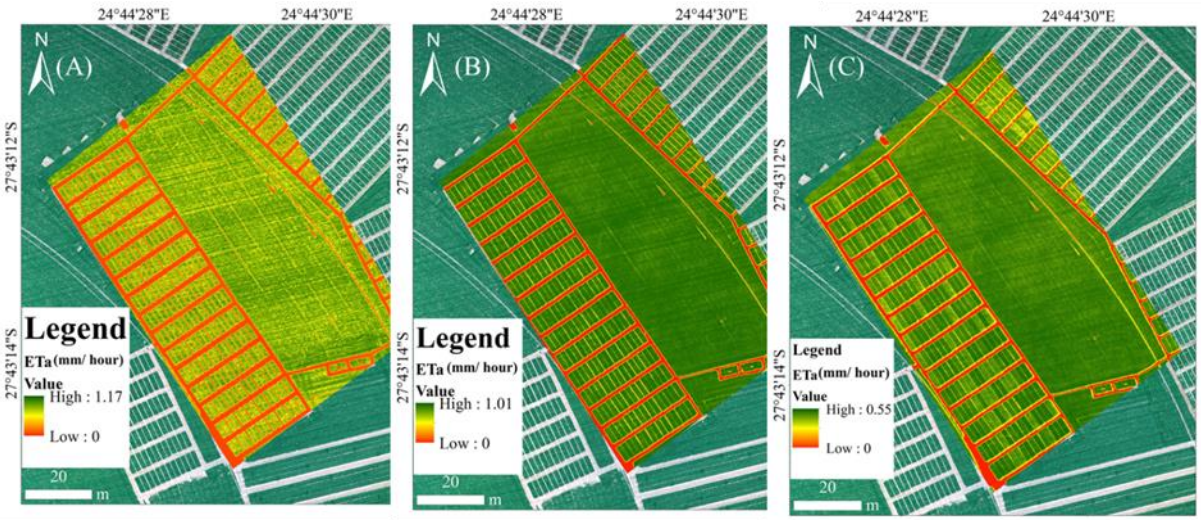

Figure 4.28: Showing the spatial variability of the daily actual evapotranspiration for different days, labels (A-C) represents; August, September and October 2020 survey days.

CHAPTER FIVE
DISCUSSIONS

Quantification of crop water use in Agricultural environments for many years has been considered an essential component in the natural water resources monitoring and management, as reported by (Carlson and Buffum, 1989; Carlson *et al*., 1994; Granger, 2000; Moran *et al*., 2000; Carlson, 2007; Hashem *et al*., 2020). Previous studies have given evapotranspiration quantification more attention with field lysimeters, weather data and Remote Sensing using satellite data (Allen *et al*., 1998; Bastiaanssen *et al*., 1998; Gowda *et al*., 2008; Wang *et al*., 2014; Doležal *et al*., 2018; Carlson, 2020).

Researchers have argued that one method is not adequate to quantify accurately crop water use (Gebler *et al*., 2015; Huang *et al*., 2018; Elkatoury *et al*., 2020). On the other hand, (Matese *et al*., 2015; Emilien *et al*., 2021; Sozzi *et al*., 2021) pointed out that the use of satellite data has limitations in quantifying spatial variability because of coarse resolutions, especially on small-scale fields. This study demonstrates the integration of different techniques to understand post irrigation crop water usage, including smart-lysimeters, weather station data, ground sensors and UAV mapping sensors. Using a stationary weather station and stationary lysimeters on a field scale does not adequately explain the spatial variability of water use. As a solution, using a UAV high resolution multispectral and thermal data set provides the ability to map the spatial variability of crop water use on a pixel basis within the field. Quantifying crop water use and the available soil water content within the field on a pixel basis enables the Agricultural land users to identify water-stressed areas and the amount of water required.

5.1 Estimation of soil water content using an electromagnetic induction instrument

Soil water content in agricultural fields is essential for crop development and growth by aiding in nutrient movement and crop nutrient uptake. Soil water content availability provides a cooling mechanism for crops through evapotranspiration, protecting the crops from heat stress or crop depression. Reduction of soil water content in crop planted areas indicates water evaporation from the wet surfaces of soil and transpiration from the leaves of crops, leading to evapotranspiration. Complete exhaustion of soil water content means soil dryness and crop water stress conditions. Therefore, monitoring soil water content is vital to determining crop and water management usage. In this study, an electromagnetic sensor

EM38 was used in measuring changes in soil electrical conductivity to quantify the changes in soil water content, measured using ADR handheld and DFM probes. An EM38 sensor was chosen based on its ability to map electrical conductivity variability without damaging the crop and soil.

The soil water content distribution reduced when the electrical conductivity readings were low and increased when the conductivity readings were higher. The results link each irrigation date and the amount of irrigation water given to the crop from analysis. In the August 2020 campaign, the survey was done on a dry field, while in October 2020, the field was medium dry. The electrical conductivity readings were also low as a result of the low soil water content available. By contrast, the (22nd and 23rd) September campaigns undertaken on the irrigated wet soils indicated high electrical conductivity due to increased soil water content availability. It was also evident from the soil electrical conductivity and soil water content spatial distribution maps of all campaigns that the bottom layers (50 cm-75 cm and 75cm to 100 cm) contained the highest soil water content and electrical conductivity from other layers. This was because the top layers are the root containing zones where crops use water, and there is exposure to evapotranspiration and deep percolation to lower layers.

It is also evident from the study findings that, the range of electrical conductivity was dependent on the quantity of soil water content availability. The simple regression statistical linear relationship tests confirmed that soil water content was the primary factor influencing the soil electrical conductivity reading fluxes. Since the field was irrigated, irrigation events and the days of the survey influenced the correlation of soil electrical conductivity with soil water content; this was similar to the works of Bai *et al.* (2013), using their own designed equipment, observed that soil electrical conductivity increases or decreases with the amount of soil water content present. Edeh (2017) also found that soil electrical conductivity correlated with soil water content availability when she used EM38 and DFM soil water content depth probes to assess the relationship among the two variables.

For the surveys undertaken when the difference in time between irrigation and survey days was high, the link between soil water content availability and soil electrical conductivity was observed by a decline in both variables, which is similar to that shown by investigations by (Abraham *et al*., 2000; Sudduth *et al*., 2005; Edeh, 2017; Altdorff *et al*., 2018; Martinez *et al*., 2018). Their studies used statistical approaches to express the relationship between soil electrical conductivity and the surface soil water content, finding the correlations to be

statistically significant (P<0.05). The results of this study have proven that the relationship between soil water content and soil electrical conductivity can be applied to map the spatial variability of soil water content since the correlation between the variables showed a statistically significant difference (P<0.05) for all surveys conducted under different wetness conditions. Dry periods without sufficient soil water content showed shallow apparent electrical conductivity values due to electrical charges not moving within the soil medium; this situation is described in the investigation by (Kitchen *et al.,* 1999).

This study observed that soil electrical conductivity could be used to estimate soil water content if it is (>0<113 mS/m). The relationship can be used as an indicator of soil wetness or dryness, which the farmer can use to indicate crop water requirement. Analysis from the laboratory relating soil electrical conductivity and other soil attributes showed that there was a moderate positive correlation between electrical conductivity (ECe), sodium (Na) and potassium (K). The correlation influence was because sodium and potassium are salts, good conductors of electricity. Conversely, soil pH and ECe showed a positive correlation resulting from the existence of salts available in the causing the soil to be acidic and able to conduct electric current.

5.2 Evapotranspiration Estimation based on lysimeters

Evapotranspiration estimated from the lysimeters for the three months showed that evapotranspiration increased from sunrise and decreased at sunset, with maximum estimations occurring during midday. This was because photosynthesis occurred when there was sufficient sunlight during the day than at night, as stated by Marques *et al*. (2020). Humidity was also very low during the day, forcing water stored in the crop and soil water content out to the atmosphere, similar to what was reported by Allen *et al*. (1998). Li *et al*. (2012) also indicated that strong wind causes the crop leaf surfaces to be dry as it wipes away the available water, leading to more occurrence of transpiration.

A rise in evapotranspiration was observed when the number of days increased from the last irrigation day. This was a consequence of water diffusion caused by the difference between the environment inside the crop and the surrounding field environment, as also concluded in the work of Gaastra (1959). Less attention had been given to evapotranspiration events at night (Marques *et al*., 2020). As a solution, smart lysimeters offers the opportunity to explore and understand losses that happen at night, based on the weight changes in the absence of sunlight. Although evapotranspiration does occur at night, findings from this study have

proven that the losses that occur between sunset and sunrise are low. Such occurrences have been observed by Malek (1992); Groh *et al*. (2019) who indicated that evapotranspiration at night could be high when the wind speed was higher. Evapotranspiration readings from this study showed an agreement in pattern with soil water content at varying depths. However, the similarities did not occur at similar depths. An increase in soil water content showed an increase in evapotranspiration, which agrees with conclusions drawn by Wang *et al*., 2009.

On further analysis, based on the estimates of ET_0 from the weather data throughout the cropping season progression, evapotranspiration was observed to be higher around days after irrigation, especially in the early growing stages when the crop canopy does not shield the exposed surface of the soil. This was because there was sufficient soil water content to be evaporated, adding to the total evapotranspiration. Assumptions are that when the canopy cover was less, and the leaf area was smaller, the total evapotranspiration was derived by soil water evaporation than crop transpiration, as described by Irmak (2003) on the concept of evapotranspiration. When the quantity of water in the soil is reduced, the soil's surface becomes dry, and no further evaporation can occur.

Similarly, when the crop leaf surfaces are dry, the crop stomata close, and transpiration ceases. This only means that more evapotranspiration occurs when the soil is wet or when the crop canopy contains sufficient water to transpire post irrigation or natural rainfall. The fluxes of ET_0 and ETa demonstrated that as the crop growth stages progress, the canopy density increases, reducing the amount of radiation reaching the soil surface, leading to more evapotranspiration occurring from crop transpiration and evaporation from canopy surfaces. In this context, the crop roots absorb the amount of water in the soil as evaporation is less. When ET drops, it is an indication that further irrigation is required to supplement the crop life.

5.3 Unmanned Aerial Vehicle (UAV) Evapotranspiration and Soil Water Content Estimation

Remote sensing observations were made from the triangular model based on vegetation fraction and surface radiant temperatures based on the visible (red) and infrared (NIR) for each Julian day campaign. The top vertex contained a cluster of pixels at higher vegetation fraction and lower scaled surface radiant temperatures from each triangle. This was due to the idea that temperature doesn't fluctuate much in canopy shaded surfaces, as indicated by (Carlson, 2007; Minacapilli *et al*., 2016; Du *et al*., 2017; Fuzzo and Rocha, 2018; Carlson

and Petropoulos, 2019). Another cluster of pixels occurs on the lower vertex of the triangle as a consequence of high surface radiant temperatures striking a bare soil surface with no vegetation. The middle section contains scattered pixels, indicating a high variation in radiant surface temperature and fractional vegetation cover; this has been well established also in the works of (Zhao and Liu, 2014; Du *et al*., 2017; Fuzzo and Rocha, 2018; Carlson and Petropoulos, 2019). A warm and cold edge exists in all triangles, which indicates the boundaries where soil water content is zero. At the same time, the scaled surface radiant temperature is equal to 1 on the warm/dry edge.

Conversely, on the cold or wet edge, soil water content is closer or equal to 1 while surface radiant temperature approaches or is equal to zero. Evapotranspiration increased with an increase in radiant surface temperature. This was a consequence of radiation supplying sufficient energy to transform soil water content (liquid) into water vapour (gas) and crops opening their stomata, giving water access to pass into the atmosphere (Carlson and Buffum, 1989). The relationship between radiant surface temperature, near infra-red (NIR) and the red band provides an opportunity to quantify soil water content availability accurately and the amount of water used by the crop over time (Minacapilli *et al*. (2016; Fuzzo and Rocha, 2018; Carlson, 2020).

The stage of development at which a crop pose determines the rate at which water is utalised by the crop and lost from the soil. When vegetation cover is not dense during early growing stages, more surface radiant energy allows more water to evaporate from the soil and plant into the atmosphere surrounding it. Therefore, soil water content variation under densely vegetated surfaces is minimum compared to an area with less vegetation cover were more soil is exposed and prone to evaporation. At the same time, a pulse was observed on bare soil. Spatial distribution of moisture availability (Mo) estimated from the triangular method demonstrated correlation when plotted against soil water content measurement. This is in agreement with the observations made in the study of Kasim *et al*. (2020), who correlated gravimetric soil water content with moisture availability (Mo) obtained from the triangular method. Any non-correlation might be a result of correlating soil water content readings measured in dense vegetation cover where the UAV imaging sensor cannot reach the soil covered by the crop canopy.

CHAPTER SIX
CONCLUSIONS, CHALLENGES AND RECOMMENDATIONS

6.1 Conclusions

The main objective of this work was to estimate barley crop water use post different irrigation quantity events for three consecutive months in the South African Barley Breeding Institute (SABBI) experimental farm. This objective was achieved by applying different monitoring methods under specific objectives, which included smart weighing lysimeters, electromagnetic induction sensing, weather data and unmanned aerial vehicle remote sensing-based models to quantify soil water content and evapotranspiration fluxes. From the findings in this particular study, it can therefore be concluded that:

The electromagnetic induction instrument (EM38) is worth using to quantify the spatial variability of soil water content by measuring the spatial variability of soil electrical conductivity as a surrogate. The EM38 based on the soil electrical conductivity was able to quantify the amount of soil water content under different field soil wetness conditions. Soil water content estimations were done for four depths up to 1 m which offers EM38 an advantage over most sensors that measure soil water content at shallow depths.

A significant observation in the simulation of soil water content variability based on soil electrical conductivity was that soil electrical conductivity response to the instrument occurs when there is sufficient amount of water content available in the soil to move the charges around. Although the results proved that soil electrical conductivity measurement could be used as a surrogate for determining soil water content using EM38, calibration for every soil type is required for better results. On the other hand, the instrument is expensive, and the interpretation of data requires scientific analysts rather than simply people with agricultural knowledge.

It is noteworthy that estimation of the actual evapotranspiration estimations can be estimated on a field scale with high accuracy and high temporal resolution ranging from a minute, an hour to daily estimations. Estimations of the actual ET from lysimeters are guided by the quantity of soil water content available in the monolith, which influences the weight changes in the lysimetric balance. Therefore, farmers can make guided decisions on their irrigation events and scheduling on understanding the weight changes. Any amount of water that goes into or out of the lysimeter is weighed depending on the lysimeter’s sensitivity. Such small

changes make lysimeters accurate and unique in estimating ETa fluxes. The cost associated with the use of smart field-weighing lysimeters and additional charges for data management on visual environments could be a limiting factor for the use of such devices.

Although the weather stations do not explain the spatial variability of the ET, they are very useful in determining the reference evapotranspiration (ET_0), which shows the influence of the atmospheric conditions in crop water use. The reference evapotranspiration (ET_0) can be used to determine the crop coefficients from the development stage through maturity to the harvest stage when used with the actual evapotranspiration (ETa). Alternatively, knowing the crop coefficient of a particular crop permits the determination of the actual evapotranspiration (ETa) if the reference evapotranspiration (ET_0) is known. It can also be concluded that ETa values on rainless days do not exceed the reference evapotranspiration (ET_0), thus making it easier to determine the water requirement by crops.

Estimating hourly evapotranspiration fluxes from the unmanned aerial vehicles were closer to the observations made from the smart weighing lysimeters. The use of unmanned aerial vehicles in the acquisition of multispectral and thermal images proved to be very advanced on a field-scale level. More pixels are acquired with high resolution than what most satellites would offer. The opportunity to have more pixels improves the spatial variability of soil water content and crop evapotranspiration. As such, dry and wet soil locations are easily obtained. With the availability of UAVs and their flexibilities, more data can be acquired to quantify daily ET without the problems of revisiting issues of time and cloud shown in satellite products.

6.2 Challenges

With the lysimeters, two problems were identified: the solar power cut affecting data logging and flooding water leaking to the drainage container box. That happened on days when their data was not used in processing. A number of flights were carried out for this study besides the presented findings due to software processing issues being unable to handle some of the data, resulting in patches in processed multispectral images. The purchase of alternative software was not possible due to financial constraints. Conversely, it was challenging to obtain some thermal UAV products due to the short battery life, which required costly replacement. Consequently, fewer days were selected and used because thermal products are essential in evapotranspiration modelling for sensible heat flux.

6.3 Recommendations

The findings of this study can solve the over-use of water through irrigation and ensure that crops are not water-stressed to maximize crop productivity. UAV technology application is relatively new in the South African agricultural field. More work with advancement in mapping sensors is required. Processing UAV data using different software can help improve the quality of acquired data. The development of small, inexpensive weighing lysimeters can assist farmers in understanding their crop water use; as such, there is a need to move in that direction, which can also cover smallholder farmers. More work in quantifying crop water use should be undertaken using different approaches in the entire irrigation scheme to understand the water losses and device means of managing and protecting water resources.

REFERENCES

Aboutalebi, M., Torres-Rua, A.F., McKee, M., Kustas, W.P., Nieto, H., Alsina, M.M., White, A., Prueger, J.H., McKee, L., Alfieri, J. and Hipps, L., 2020. Incorporation of Unmanned Aerial Vehicle (UAV) Point Cloud Products into Remote Sensing Evapotranspiration Models. *Remote sensing*, 12(1), p. 50.

Abraham, N., Hema, P.S., Saritha, E.K. and Subramannian, S., 2000. Irrigation automation based on soil electrical conductivity and leaf temperature. *Agricultural Water Management*, 45(2), pp.145-157.

Acharya, B.S., Bhandari, M., Bandini, F., Pizarro, A., Perks, M., Joshi, D.R., Wang, S., Dogwiler, T., Ray, R.L., Kharel, G. and Sharma, S., 2021. Unmanned Aerial Vehicles in Hydrology and Water Management: Applications, Challenges, and Perspectives. *Water Resources Research*, 57(11), p.e2021WR029925.

Alavi, S.A. and Rahimikhoob, A., 2016. A simple model for determining reference evapotranspiration using NOAA satellite data: A case study. *Environmental Processes*, *3*(2), pp. 479-493.

Allen, R.G., Pereira, L.S., Raes, D. and Smith, M., 1998. *Crop evapotranspiration-Guidelines for computing crop water requirements-FAO Irrigation and drainage paper 56*. Fao, Rome, 300(9), p.D05109.

Allen, R.G., Tasumi, M., Trezza, R., Waters, R. and Bastiaanssen, W., 2002. Sebal (surface energy balance algorithms for land). *Advance Training and User's Manual–Idaho Implementation*, version, 1, p. 97.

Altdorff, D., Galagedara, L., Nadeem, M., Cheema, M. and Unc, A., 2018. Effect of agronomic treatments on the accuracy of soil moisture mapping by electromagnetic induction. *Catena*, 164, pp.96-106.

Amankwah, E.A., 2007. Predictive modelling of organic pollutant leaching and transport behaviour at the lysimeter and field scales. (MSc dissertation, Univ. Dresden).

Anderson, M.C., Allen, R.G., Morse, A. and Kustas, W.P., 2012. Use of Landsat thermal imagery in monitoring evapotranspiration and managing water resources. *Remote Sensing of Environment*, 122, pp.50-65.

Andresen, C.G., Lawrence, D.M., Wilson, C.J., McGuire, A.D., Koven, C., Schaefer, K., Jafarov, E., Peng, S., Chen, X., Gouttevin, I. and Burke, E., 2020. Soil moisture and hydrology projections of the permafrost region–a model intercomparison. *The Cryosphere*, *14*(2), pp. 445-459.

Arp, R.S., Fraser, G.C.G. and Hill, M.P., 2017. Quantifying the economic water savings benefit of water hyacinth (Eichhornia crassipes) control in the Vaalharts Irrigation Scheme. *Water Sa*, 43(1), pp.58-66.

Bai, W., Kong, L. and Guo, A., 2013. Effects of physical properties on electrical conductivity of compacted lateritic soil. *Journal of Rock Mechanics and Geotechnical Engineering*, 5(5), pp.406-411.

Bastiaanssen, W.G., 2000. SEBAL-based sensible and latent heat fluxes in the irrigated Gediz Basin, Turkey. *Journal of Hydrology*, 229(1-2), pp. 87-100.

Bastiaanssen, W.G., Menenti, M., Feddes, R.A. and Holtslag, A.A.M., 1998. A remote sensing surface energy balance algorithm for land (SEBAL). 1. Formulation. *Journal of Hydrology*, 212, pp. 198-212.

Bawa, A., Senay, G.B. and Kumar, S., 2021. Regional crop water use assessment using Landsat-derived evapotranspiration. *Hydrological Processes*, *35*(1), p.e14015.

BBA 1990. Guidelines for the testing of plant protection products in Approval Procedure, Part IV, 4–3, Lysimeter Examinations for Relocation of plant protection products underground. *Biological Federal Agency for Agriculture and Forestry*, Braunschweig.

Belcaid, A., Benaicha, M., Le Palec, G. and Draoui, A., 2020. Simulation of Water Infiltration Process into a Porous Unsaturated Soil: Application on Tangier's Bay Region-Morocco. *Geotechnical and Geological Engineering*, *38*(1), pp. 353-365.

Berliner, P.R. and Oosterhuis, D.M., 1987. Effect of root and water distribution in lysimeters and in the field on the onset of crop water stress. *Irrigation science*, 8(4), pp. 245-255.

Bhatt, R. and Hossain, A., 2019. Concept and consequence of evapotranspiration for sustainable crop production in the Era of climate change. In *Advanced Evapotranspiration Methods and Applications*. IntechOpen.

Braune, E. and Roger, K.H., 1987. *The Vaal River catchment: problems and research needs.*

Brown, P., 2008, December. Flood vs. pivot irrigation for forage crops: what are the advantages and disadvantages. In *Proceedings, California Alfalfa & Forage Symposium and Western Seed Conference, San Diego, CA.*

Calera, A., Campos, I., Osann, A., D'Urso, G. and Menenti, M., 2017. Remote sensing for crop water management: From ET modelling to services for the end users. *Sensors*, *17*(5), p. 1104.

Carlson, T.N. and Buffum, M.J., 1989. On estimating total daily evapotranspiration from remote surface temperature measurements. *Remote Sensing of Environment*, 29(2), pp. 197-207.

Carlson, T.N. and Petropoulos, G.P., 2019. A new method for estimating of evapotranspiration and surface soil moisture from optical and thermal infrared measurements: The simplified triangle. *International Journal of Remote Sensing*, 40(20), pp. 7716-7729.

Carlson, T.N. and Ripley, D.A., 1997. On the relation between NDVI, fractional vegetation cover, and leaf area index. *Remote Sensing of Environment*, 62(3), pp. 241-252.

Carlson, T.N., 2007. An overview of the so-called "triangle method" for estimating surface evapotranspiration and soil moisture from satellite imagery. *Sensors*, 2007, 7, 1612-1629.

Carlson, T.N., 2020. A Brief Analysis of the Triangle Method and a Proposal for its Operational Implementation. *Remote Sensing*, 12(22), p. 3832.

Carlson, T.N.; Gillies, R.R.; Perry, E.M., 1994. A method to make use of thermal infrared temperature and NDVI measurements to infer surface soil water content and fractional vegetation cover. *Remote Sensing Reviews* 1994, 9,161-173.

Cavalcante, E.G., Medeiros, J.F.D., Espínola, J., Figueirêdo, V.B., da Costa, J.P. and Santos, W.D.O., 2016. Development and water requirements of cowpea under climate change conditions in the Brazilian semi-arid region. *Brazilian Journal of Agricultural and Environmental Engineering*, 20, pp. 783-788.

Corwin, D.L. and Plant, R.E., 2005. Applications of apparent soil electrical conductivity in precision agriculture. *Computers and Electronics in Agriculture*, 46(1-3), pp.1-10.

Corwin, D.L., 2021. Climate change impacts on soil salinity in agricultural areas. *European Journal of Soil Science*, *72*(2), pp. 842-862.

Costa, M.M., Queiroz, D.M.D., Pinto, F.D.A.D.C., Reis, E.F.D. and Santos, N.T., 2014. Moisture content effect in the relationship between apparent electrical conductivity and soil attributes. Acta Scientiarum. *Agronomy*, 36(4), pp.395-401.

Damkjaer, S. and Taylor, R., 2017. The measurement of water scarcity: Defining a meaningful indicator. *Ambio*, *46*(5), pp. 513-531.

Datta, S., Taghvaeian, S., Ochsner, T.E., Moriasi, D., Gowda, P. and Steiner, J.L., 2018. Performance assessment of five different soil moisture sensors under irrigated field conditions in Oklahoma. *Sensors*, *18*(11), p. 3786.

Doležal, F., Hernandez-Gomis, R., Matula, S., Gulamov, M., Miháliková, M. and Khodjaev, S., 2018. Actual evapotranspiration of unirrigated grass in a smart field lysimeter. *Vadose Zone Journal*, *17*(1), pp. 1-13.

Dorigo, W., Wagner, W., Albergel, C., Albrecht, F., Balsamo, G., Brocca, L., Chung, D., Ertl, M., Forkel, M., Gruber, A. and Haas, E., 2017. ESA CCI Soil Moisture for improved Earth system understanding: State-of-the art and future directions. *Remote Sensing of Environment*, *203*, pp. 185-215.

Du, L., Song, N., Liu, K., Hou, J., Hu, Y., Zhu, Y., Wang, X., Wang, L. and Guo, Y., 2017. Comparison of two simulation methods of the temperature vegetation dryness index (TVDI) for drought monitoring in semi-arid regions of China. *Remote Sensing*, 9(2), p. 177.

Edeh, J.A., 2017. Quantifying spatio-temporal soil water content using electromagnetic induction (*Doctoral dissertation*, University of the Free State).

Eigenberg, R.A., Doran, J.W., Nienaber, J.A., Ferguson, R.B. and Woodbury, B.L., 2002. Electrical conductivity monitoring of soil condition and available N with animal manure and a cover crop. *Agriculture, Ecosystems & Environment*, *88*(2), pp. 183-193.

Elfarkh, J., Ezzahar, J., Er-Raki, S., Simonneaux, V., Ait Hssaine, B., Rachidi, S., Brut, A., Vincent, R., Khabba, S., Chehbouni, A. and Jarlan, L., 2020. Multi-Scale Evaluation of the TSEB Model over a Complex Agricultural Landscape in Morocco. *Remote Sensing*, 12(7), p. 1181.

Elkatoury, A., Alazba, A.A. and Mossad, A., 2020. Estimating Evapotranspiration Using Coupled Remote Sensing and Three SEB Models in an Arid Region. *Environmental Processes*, 7(1), pp. 109-133.

Ellsäßer, F., Röll, A., Stiegler, C. and Hölscher, D., 2020. Introducing QWaterModel, a QGIS plugin for predicting evapotranspiration from land surface temperatures. *Environmental Modelling & Software*, p. 104739.

Emilien, A.V., Thomas, C. and Thomas, H., 2021. UAV & satellite synergies for optical remote sensing applications: A literature review. *Science of Remote Sensing*, p.100019.

Evans, R.G. and Sadler, E.J., 2008. Methods and technologies to improve efficiency of water use. *Water Resources Research*, *44*(7).

Evett, S.R., Heng, L.K., Moutonnet, P. and Nguyen, M.L., 2008. Field estimation of soil water content: A practical guide to methods, instrumentation, and sensor technology. *IAEA: Vienna*.

Fischer, G., Tubiello, F.N., Van Velthuizen, H. and Wiberg, D.A., 2007. Climate change impacts on irrigation water requirements: Effects of mitigation, 1990–2080. *Technological Forecasting and Social Change*, *74*(7), pp. 1083-1107.

Fuzzo, D.F.D.S.S. and Rocha, J.V., 2018. Simplify the triangle method for estimating evapotranspiration and its use in agrometeorological modeling. *Applied Research & Agrotechnology*, 11(1), pp. 07-15.

Gaastra, P., 1959. *Photosynthesis of crop plants as influenced by light, carbon dioxide, temperature, and stomatal diffusion resistance* (Doctoral dissertation, Veenman).

Gebler, S., Hendricks Franssen, H.J., Pütz, T., Post, H., Schmidt, M. and Vereecken, H., 2015. Actual evapotranspiration and precipitation measured by lysimeters: a comparison with eddy covariance and tipping bucket. *Hydrology and Earth System Sciences*, 19(5), pp. 2145-2161.

Gentine, P., Chhang, A., Rigden, A. and Salvucci, G., 2016. Evaporation estimates using weather station data and boundary layer theory. *Geophysical Research Letters*, 43(22), pp. 11-661.

Ghaderi, A., Dasineh, M., Shokri, M. and Abraham, J., 2020. Estimation of Actual Evapotranspiration Using the Remote Sensing Method and SEBAL Algorithm: A Case Study in Ein Khosh Plain, Iran. *Hydrology*, 7(2), p. 36.

Gong, L., Xu, C.Y., Chen, D., Halldin, S. and Chen, Y.D., 2006. Sensitivity of the Penman–Monteith reference evapotranspiration to key climatic variables in the Changjiang (Yangtze River) basin. *Journal of Hydrology*, *329*(3-4), pp. 620-629.

Gowda, P.H., Chavez, J.L., Colaizzi, P.D., Evett, S.R., Howell, T.A. and Tolk, J.A., 2008. ET mapping for agricultural water management: present status and challenges. *Irrigation Science*, 26(3), pp. 223-237.

Granger, R.J., 2000. Satellite-derived estimates of evapotranspiration in the Gediz basin. *Journal of Hydrology* 2000, 229, pp. 70–76.

Grisso, R.B., Alley, M., Holshouser, D. and Thomason, W., 2009. Precision farming tools: Soil electrical conductivity. DOCPLAYER.

Grobler, DC,* Toerien, DF* & Rossouw, J., 1987. A review of sediment I water quality interaction with particular reference to the Vaal River system. *Water SA*, 13(1), pp.15-22.

Groh, J., Puetz, T., Gerke, H.H., Vanderborght, J. and Vereecken, H., 2019, December. Quantifying and predicting nighttime evapotranspiration for two distinct grassland ecosystems. In *AGU Fall Meeting Abstracts* (Vol. 2019, pp. H23C-05).

Guion, A., Turquety, S., Polcher, J., Pennel, R., Bastin, S. and Arsouze, T., 2021. Droughts and heatwaves in the Western Mediterranean: impact on vegetation and wildfires using the coupled WRF-ORCHIDEE regional model (RegIPSL). *Climate Dynamics*, pp. 1-23.

Hashem, A.A., Engel, B.A., Bralts, V.F., Marek, G.W., Moorhead, J.E., Rashad, M., Radwan, S. and Gowda, P.H., 2020. Landsat Hourly Evapotranspiration Flux Assessment using Lysimeters for the Texas High Plains. *Water*, 12(4), p. 1192.

Hedley, C.B. and Yule, I.J., 2009. Soil water status mapping and two variable-rate irrigation scenarios. *Precision Agriculture*, *10*(4), pp. 342-355.

Herold, C.E and Bailey, A.K., 1996. Long term salt balance of the Vaalharts Irrigation Scheme. WRC Report No. 420/1/96. *Water Research Commission*, Pretoria.

Hough, J.J.H. and Rudolph, D.C., 2003. Vaalharts Groundwater Protocol for on-site sanitation. *Report fr VKE Engineers, by GHT. GHT Consulting Report No. RVN*, *331*, p.482.

Huang, Y., Chen, Z.X., Tao, Y.U., Huang, X.Z. and Gu, X.F., 2018. Agricultural remote sensing big data: Management and applications. *Journal of Integrative Agriculture*, *17*(9), pp.1915-1931.

Hutson, J.L., Green, G.C. and Meyer, W.S., 1980. A weighing lysimeter facility at Roodeplaat for crop evapotranspiration studies. *Water SA*, 6(1), pp. 41-48.

Inman-Bamber, N.G. and McGlinchey, M.G., 2003. Crop coefficients and water-use estimates for sugarcane based on long-term Bowen ratio energy balance measurements. *Field Crops Research*, *83*(2), pp. 125-138.

Irmak, S. and Haman, D.Z., 2003. Evapotranspiration: potential or reference. *IFAS Extension, ABE*, *343*, pp. 1-3.

Irmak, S., Kabenge, I., Rudnick, D., Knezevic, S., Woodward, D. and Moravek, M., 2013. Evapotranspiration crop coefficients for mixed riparian plant community and transpiration crop coefficients for Common reed, Cottonwood and Peach-leaf willow in the Platte River Basin, Nebraska-USA. *Journal of Hydrology*, *481*, pp. 177-190.

Javadinejad, S., Dara, R. and Jafary, F., 2019. Impacts of Extreme Events on Water Availability. *Annals of Geographical Studies*, *2*(3), pp. 16-24.

Kasim, A., Nahum Carlson, T. and Shehu Usman, H., 2020. Limitations in validating derived soil water content from thermal/optical measurements using the simplified triangle method. *Remote Sensing*, 12(7), p. 1155.

Kergoat, L., Lafont, S., Douville, H., Berthelot, B., Dedieu, G., Planton, S. and Royer, J.F., 2002. Impact of doubled CO2 on global-scale leaf area index and evapotranspiration: Conflicting stomatal conductance and LAI responses. *Journal of Geophysical Research: Atmospheres*, *107*(D24), pp.ACL-30.

Kitchen, N.R., Sudduth, K.A. and Drummond, S.T., 1999. Soil electrical conductivity as a crop productivity measure for clay pan soils. *Journal of Production Agriculture*, *12*(4), pp. 607-617.

Kongo, V.M. and Jewitt, G.P.W., 2006. Preliminary investigation of catchment hydrology in response to agricultural water use innovations: A case study of the Potshini catchment–South Africa. *Physics and Chemistry of the Earth*, Parts A/B/C, 31(15-16), pp. 976-987.

Kramer, J.H., Cullen, S.J. and Everett, L.G., 2018. Vadose Zone Monitoring with the neutron moisture probe "Handbook *of vadose zone characterization & monitoring darin"*, p. 291.

Kruger, M., Van Rensburg, J.B.J. and Van den Berg, J., 2009. Perspective on the development of stem borer resistance to Bt maize and refuge compliance at the Vaalharts irrigation scheme in South Africa. *Crop protection*, 28(8), pp. 684-689.

Kutilek, M. and Nielsen, D.R., 1994. *Soil hydrology: textbook for students of soil science, agriculture, forestry, geoecology, hydrology, geomorphology, and other related disciplines*. Catena Verlag.

Lehmann, P., Berli, M., Koonce, J.E. and Or, D., 2019. Surface evaporation in arid regions: Insights from lysimeter decadal record and global application of a surface evaporation capacitor (SEC) model. *Geophysical Research Letters*, *46*(16), pp. 9648-9657.

Le Roux, P.A.L., du Preez, C., Strydom, M., van Rensburg, L. and Bennie, A., 2007. Effect of irrigation on soil salinity profiles along the Lower Vaal River, South Africa. *Water SA*, 33(4).

Lei, F., Crow, W.T., Holmes, T.R., Hain, C. and Anderson, M.C., 2018. Global investigation of soil moisture and latent heat flux coupling strength. *Water Resources Research*, *54*(10), pp. 8196-8215.

Li, Z., Zheng, F.L. and Liu, W.Z., 2012. Spatiotemporal characteristics of reference evapotranspiration during 1961–2009 and its projected changes during 2011–2099 on the Loess Plateau of China. *Agricultural and Forest Meteorology*, 154, pp. 147-155.

Little, K.M., Metelerkamp, B. and Smith, C.W., 1998. A comparison of three methods of soil water content determination. *South African Journal of Plant and Soil*, *15*(2), pp. 80-89.

Makkink, G.F., 1959. Limitations and perspectives of lysimeter research. In Colloque de Hannoversch-Muenden 8-14 September 1959 = *Symposium of Hannoversch-Muenden* 8-14 September 1959 (No. 48, 49, pp. 13-25). AIHS.

Malek, E., 1992. Night-time evapotranspiration vs. daytime and 24h evapotranspiration. *Journal of Hydrology*, *138*(1-2), pp. 119-129.

Maliva, R., 2021. *Climate Change and Groundwater: Planning and Adaptations for a Changing and Uncertain Future: WSP Methods in Water Resources Evaluation Series No. 6*. Springer Nature.

Marques, T.V., Mendes, K., Mutti, P., Medeiros, S., Silva, L., Perez-Marin, A.M., Campos, S., Lúcio, P.S., Lima, K., dos Reis, J. and Ramos, T.M., 2020. Environmental and biophysical controls of evapotranspiration from Seasonally Dry Tropical Forests (Caatinga) in the Brazilian Semiarid. *Agricultural and Forest Meteorology*, 287, p. 107957.

Martinez, G., Huang, J., Vanderlinden, K., Giraldez, J.V. and Triantafilis, J., 2018. Potential to predict depth-specific soil–water content beneath an olive tree using electromagnetic conductivity imaging. *Soil Use and Management*, 34(2), pp.236-248.

Masasi, B. and Ng'ombe, J.N., 2019. Does a market systems approach revitalize smallholder irrigation schemes? Evidence from Zimbabwe.

Matese, A., Toscano, P., Di Gennaro, S.F., Genesio, L., Vaccari, F.P., Primicerio, J., Belli, C., Zaldei, A., Bianconi, R. and Gioli, B., 2015. Intercomparison of UAV, aircraft and satellite remote sensing platforms for precision viticulture. *Remote Sensing*, *7*(3), pp.2971-2990.

McNally, A., 2016. FLDAS Noah Land Surface Model L4 daily 0.1 × 0.1 Degree for Southern Africa (GDAS and RFE2) V001; NASA/GSFC/HSL: Greenbelt, MD, USA, 2016.

Meissner, R., Prasad, M.N.V., Du Laing, G. and Rinklebe, J., 2010. Lysimeter application for measuring the water and solute fluxes with high precision. *Current Science (Bangalore)*, *99*(5), pp. 601-607.

Minacapilli, M., Consoli, S., Vanella, D., Ciraolo, G. and Motisi, A., 2016. A time domain triangle method approach to estimate actual evapotranspiration: Application in a Mediterranean region using MODIS and MSG-SEVIRI products. *Remote sensing of environment*, 174, pp. 10-23.

Mkhwanazi, M., 2014. Developing a modified SEBAL algorithm that is responsive to advection by using limited weather data (*Doctoral dissertation*, Colorado State University. Libraries).

Mokhtari, A., Noory, H., Pourshakouri, F., Haghighatmehr, P., Afrasiabian, Y., Razavi, M., Fereydooni, F. and Naeni, A.S., 2019. Calculating potential evapotranspiration and single crop coefficient based on energy balance equation using Landsat 8 and Sentinel-2. *ISPRS Journal of Photogrammetry and Remote Sensing*, *154*, pp. 231-245.

Moorhead, J.E., Marek, G.W., Colaizzi, P.D., Gowda, P.H., Evett, S.R., Brauer, D.K., Marek, T.H. and Porter, D.O., 2017. Evaluation of sensible heat flux and evapotranspiration estimates using a surface layer scintillometer and a large weighing lysimeter. *Sensors*, 17(10), p. 2350.

Moran, M.S., Hymer, D.C., Qi, J., Sano, E.E., 2000. Soil moisture evaluation using multi-temporal Synthetic Aperture Radar (SAR) in semiarid rangeland. *Agriculture and Forest Meteorology* 2000, 105, pp. 69–80.

Morse, A., Kramber, W.J., Allen, R.G. and Tasumi, M., 2004, September. Use of the METRIC evapotranspiration model to compute water use by irrigated agriculture in Idaho. In IGARSS 2004. 2004 *IEEE International Geoscience and Remote Sensing Symposium* (Vol. 3, pp. 2134-2137). IEEE.

Mukherjee, A., Kundu, M. and Sarkar, S., 2010. Role of irrigation and mulch on yield, evapotranspiration rate and water use pattern of tomato (Lycopersicon esculentum L.). *Agricultural Water Management*, 98(1), pp. 182-189.

Mutanga, O., Dube, T. and Galal, O., 2017. Remote sensing of crop health for food security in Africa: Potentials and constraints. *Remote Sensing Applications: Society and Environment*, 8, pp. 231-239.

Ndou, N.N., Palamuleni, L.G. and Ramoelo, A., 2018. Modelling depth to groundwater level using SEBAL-based dry season potential evapotranspiration in the upper Molopo River Catchment, South Africa. *The Egyptian Journal of Remote Sensing and Space Science*, 21(3), pp. 237-248.

Nhamo, L., Magidi, J., Nyamugama, A., Clulow, A.D., Sibanda, M., Chimonyo, V.G. and Mabhaudhi, T., 2020. Prospects of Improving Agricultural and Water Productivity through Unmanned Aerial Vehicles. *Agriculture*, *10*(7), p. 256.

Norman, J.M., Kustas, W.P., Prueger, J.H. and Diak, G.R., 2000. Surface flux estimation using radiometric temperature: A dual-temperature-difference method to minimize measurement errors. *Water Resources Research*, 36(8), pp. 2263-2274.

Ortega-Farías, S., Ortega-Salazar, S., Poblete, T., Poblete-Echeverría, C., Zúñiga, M., Sepúlveda-Reyes, D., Kilic, A. and Allen, R., 2015, June. Estimation of olive evapotranspiration using multispectral and thermal sensors placed aboard an unmanned aerial vehicle. In VIII International Symposium on Irrigation of Horticultural Crops 1150 (pp. 1-8).

Peng, T., Deng, H., Lin, Y. and Jin, Z., 2021. Assessment on water resources carrying capacity in karst areas by using an innovative DPESBRM concept model and cloud model. *Science of The Total Environment*, *767*, p. 144353.

Pereira, D.T.B., David, R.B. and Menani, J.V., 2002. Episodes of water deprivation enhance daily hypertonic NaCl intake in rats. *Brazilian Journal of Medical and Biological Research*, *35*, pp. 465-468.

Pretorius, W.M., 2018. *Vaalharts: environmental aspects of agricultural land and water use practices* (Doctoral dissertation, North-West University).

Prinz, D. and Singh, A.K., 2000. Water resources in arid regions and their sustainable management. *Annals of Arid Zone*, 39(3), pp. 251-272.

Ramatsimela, M.J., 2007. *Realizing agricultural potential in land reform: The case of Vaalharts Irrigation Scheme in the Northern Cape Province* (Doctoral dissertation, University of the Western Cape).

Rauneker, P. and Lischeid, G., 2012. Spatial distribution of water stress and evapotranspiration estimates using an unmanned aerial vehicle (UAV). EGUGA, p. 10477.

Robinson, J.B., Silburn, D.M., Foley, J. and Orange, D., 2010, August. Root zone soil moisture content in a Vertosol is accurately and conveniently measured by electromagnetic induction measurements with an EM38. In *19th World Congress of Soil Science, Soil Solutions for a Changing World* (pp. 78-81).

Robock, A., Vinnikov, K.Y., Srinivasan, G., Entin, J.K., Hollinger, S.E., Speranskaya, N.A., Liu, S. and Namkhai, A., 2000. The global soil moisture data bank. *Bulletin of the American Meteorological Society*, *81*(6), pp. 1281-1300.

Ruhoff, A.L., Paz, A.R., Collischonn, W., Aragao, L.E., Rocha, H.R. and Malhi, Y.S., 2012. A MODIS-based energy balance to estimate evapotranspiration for clear-sky days in Brazilian tropical savannas. *Remote Sensing*, 4(3), pp. 703-725.

Salamé, L., Bogardi, J.J., Sebesvari, Z., Tockner, K., Yazici, B., Turan, F., Calli, B., Kerç, A., Ünver, O. and Walz, Y., 2021. Drivers, Pressures and Stressors: The Societal Framework of Water Resources Management. In *Handbook of Water Resources Management: Discourses, Concepts and Examples* (pp. 329-364). Springer, Cham.

Santos, C.A.C.D., Bezerra, B.G., Silva, B.B.D. and Rao, T.V.R., 2010. Assessment of daily actual evapotranspiration with SEBAL and S-SEBI algorithms in cotton crop. *Revista Brasileira de Meteorologia*, 25(3), pp. 383-392.

Scott, R.L. and Biederman, J.A., 2017. Partitioning evapotranspiration using long-term carbon dioxide and water vapour fluxes. *Geophysical Research Letters*, *44*(13), pp. 6833-6840.

Seshoka, J.L. and Willem Faysse, N., 2004. *The transformation of irrigation boards into water user associations in South Africa: Case studies of the Lower Olifants, Great Letaba and Vaalharts water user associations. Volume 1* (Vol. 72). IWMI.

Sheets, K.R. and Hendrickx, J.M., 1995. Noninvasive soil water content measurement using electromagnetic induction. *Water resources research*, 31(10), pp.2401-2409.

Singels, A., Jarmain, C., Bastidas-Obando, E., Olivier, F.C. and Paraskevopoulos, A.L., 2018. Monitoring water use efficiency of irrigated sugarcane production in Mpumalanga, South Africa, using SEBAL. *Water SA*, 44(4), pp. 636-646.

Singh, R.K. and Senay, G.B., 2016. Comparison of four different energy balance models for estimating evapotranspiration in the Midwestern United States. *Water*, 8(1), p. 9.

Sovoe, S., 2011. Mapping irrigated area fragments for crop water use assessment using handheld spectroradiometer. *International Journal of Agronomy*, 2011.

Sozzi, M., Kayad, A., Gobbo, S., Cogato, A., Sartori, L. and Marinello, F., 2021. Economic comparison of satellite, plane and UAV-acquired NDVI images for site-specific nitrogen application: Observations from Italy. *Agronomy*, *11*(11), p.2098.

Stanley, J.N., Lamb, D.W., Falzon, G. and Schneider, D.A., 2014. Apparent electrical conductivity (ECa) as a surrogate for neutron probe counts to measure soil moisture content in heavy clay soils (Vertosols). *Soil research*, 52(4), pp.373-378.

Streutker, A., 1977. The dependence of permatlent crop production on efficient irrigation and drainage at the Vaalharts Government Water scheme. *Water SA*, *3*(2), pp.90.

Sudduth, K.A., 1999, May. Engineering technologies for precision farming. In *International Seminar on Agricultural Mechanization Technology for Precision Farming* (pp. 5-27). Suwon: Rural Development Admin.

Sudduth, K.A., Kitchen, N.R., Wiebold, W.J., Batchelor, W.D., Bollero, G.A., Bullock, D.G., Clay, D.E., Palm, H.L., Pierce, F.J., Schuler, R.T. and Thelen, K.D., 2005. Relating apparent electrical conductivity to soil properties across the north-central USA. *Computers and electronics in agriculture*, 46(1-3), pp. 263-283.

Sun, Z., Wei, B., Su, W., Shen, W., Wang, C., You, D. and Liu, Z., 2011. Evapotranspiration estimation based on the SEBAL model in the Nansi Lake Wetland of China. *Mathematical and Computer Modelling*, 54(3-4), pp. 1086-1092.

Topp, G.C., Davis, J.L. and Annan, A.P., 1980. Electromagnetic determination of soil water content: Measurements in coaxial transmission lines. *Water Resources Research*, *16*(3), pp. 574-582.

Trenberth, K.E., 2011. Changes in precipitation with climate change. *Climate Research*, *47*(1-2), pp. 123-138.

Verstraeten, W.W., Veroustraete, F. and Feyen, J., 2008. Assessment of evapotranspiration and soil moisture content across different scales of observation. *Sensors*, *8*(1), pp. 70-117.

Verwey, P.M.J. and Vermeulen, P.D., 2011. Influence of irrigation on the level, salinity, and flow of groundwater at Vaalharts Irrigation Scheme. *Water SA*, *37*(2).

Wang, L., Good, S.P. and Caylor, K.K., 2014. Global synthesis of vegetation control on evapotranspiration partitioning. *Geophysical Research Letters*, 41(19), pp. 6753-6757.

Wang, P., Li, X.Y., Wang, L., Wu, X., Hu, X., Fan, Y. and Tong, Y., 2018. Divergent evapotranspiration partition dynamics between shrubs and grasses in a shrub-encroached steppe ecosystem. *New Phytologist*, 219(4), pp. 1325-1337.

Wang, Y.M., Traore, S. and Kerh, T., 2009. Applying evapotranspiration reference model and rainfall contribution index for agricultural water management plan in Burkina Faso. *African Journal of Agricultural Research*, 4(12), pp. 1493-1504.

Williams, L.E. and Ayars, J.E., 2005. Grapevine water use and the crop coefficient are linear functions of the shaded area measured beneath the canopy. *Agricultural and Forest Meteorology*, *132*(3-4), pp. 201-211.

Wolff, B., Kühnert, J., Lorenz, E., Kramer, O. and Heinemann, D., 2016. Comparing support vector regression for PV power forecasting to a physical modelling approach using measurement, numerical weather prediction, and cloud motion data. *Solar Energy*, 135, pp. 197-208.

Xia, T., Kustas, W.P., Anderson, M.C., Alfieri, J.G., Gao, F., McKee, L., Prueger, J.H., Geli, H.M., Neale, C.M., Sanchez, L. and Alsina, M.M., 2016. Mapping evapotranspiration with high-resolution aircraft imagery over vineyards using one-and two-source modeling schemes. *Hydrology and Earth System Sciences*, 20(4), pp.1523-1545.

Yang, X., Wu, J.J., Shi, P.J. and Yan, F., 2008. Modified triangle method to estimate soil moisture status with MODerate resolution Imaging Spectroradiometer (MODIS) products. Proc. Int. Arch. Photogramm. *Remote Sens*ing. Spat. Inf. Sci, 37, pp. 555-560.

Zhang, R., Kim, S. and Sharma, A., 2019. A comprehensive validation of the SMAP Enhanced Level-3 Soil Moisture product using ground measurements over varied climates and landscapes. *Remote Sensing of Environment*, *223*, pp. 82-94

Zhao, X. and Liu, Y., 2014. Relative contribution of the topographic influence on the triangle approach for evapotranspiration estimation over mountainous areas. *Advances in Meteorology*, 2014.

Zhu, W., Jia, S. and Lv, A., 2017. A universal Ts-VI triangle method for the continuous retrieval of evaporative fraction from MODIS products. *Journal of Geophysical Research: Atmospheres*, 122(19), pp. 10-206.

Zhu, Y., Irmak, S., Jhala, A.J., Vuran, M.C. and Diotto, A., 2019. Time-domain and frequency-domain reflectometry type soil moisture sensor performance and soil temperature effects in fine-and coarse-textured soils. *Applied Engineering in Agriculture*, p. 117-134.

Zotarelli, L., Dukes, M.D., Romero, C.C., Migliaccio, K.W. and Morgan, K.T., 2010. Step by step calculation of the Penman-Monteith Evapotranspiration (FAO-56 Method). *Institute of Food and Agricultural Sciences. University of Florida*.

Zwieback, S., Westermann, S., Langer, M., Boike, J., Marsh, P. and Berg, A., 2019. Improving permafrost modelling by assimilating remotely sensed soil moisture. *Water Resources Research*, *55*(3), pp. 1814-1832.

APPENDIX

Appendix I: Multispectral UAV data processing report (10 August 2020)

Processing Report

esri

Generated with Drone2Map for ArcGIS

Summary

Project	Hartswater10082020
Processed	2020-08-20 11:39:46
Camera Model Name(s)	RedEdge-M_5.5_1280x960 (Blue), RedEdge-M_5.5_1280x960 (Green), RedEdge-M_5.5_1280x960 (Red), RedEdge-M_5.5_1280x960 (NIR), RedEdge-M_5.5_1280x960 (Red edge)
Average Ground Sampling Distance (GSD)	6.76 cm / 2.66 in
Area Covered	0.322 km^2 / 32.2407 ha / 0.12 sq. mi. / 79.7096 acres
Time for Initial Processing (without report)	02h:46m:47s

Quality Check

Images	median of 5371 keypoints per image	⚠
Dataset	3265 out of 3265 images calibrated (100%), all images enabled	✓
Camera Optimization	0.09% relative difference between initial and optimized internal camera parameters	✓
Matching	median of 3874.8 matches per calibrated image	✓
Georeferencing	yes, no 3D GCP	⚠

Preview

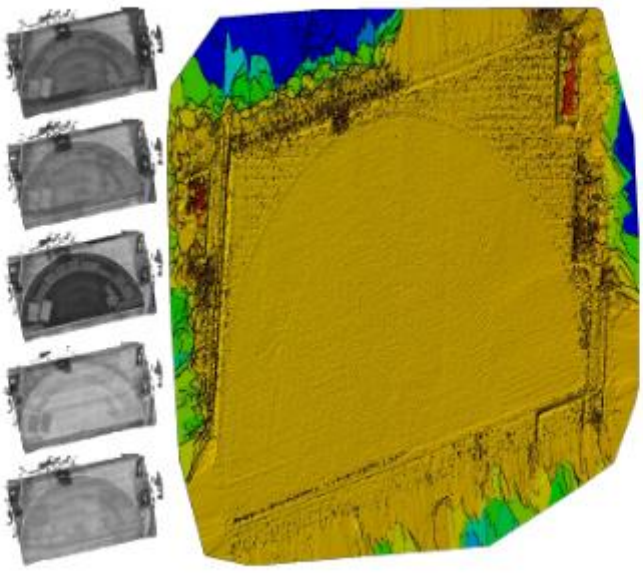

Figure 1: Orthomosaic and the corresponding sparse Digital Surface Model (DSM) before densification.

Report available on:

https://drive.google.com/drive/folders/1W_VpwfUDQ_jSl_PRjc3Snx4YtF0KqW1g?usp=sharing

Appendix II: Multispectral UAV data processing report (22 September 2020)

Processing Report

esri

Generated with Drone2Map for ArcGIS

Summary

Project	HW22092020MS1
Processed	2020-10-30 21:28:56
Camera Model Name(s)	RedEdge-M_5.5_1280x960 (Blue), RedEdge-M_5.5_1280x960 (Green), RedEdge-M_5.5_1280x960 (Red), RedEdge-M_5.5_1280x960 (NIR), RedEdge-M_5.5_1280x960 (Red edge)
Average Ground Sampling Distance (GSD)	5.55 cm / 2.18 in
Area Covered	0.379 km^2 / 37.9180 ha / 0.15 sq. mi. / 93.7460 acres
Time for Initial Processing (without report)	11h:33m:30s

Quality Check

Images	median of 5337 keypoints per image	⚠
Dataset	4372 out of 4380 images calibrated (99%), 15 images disabled	✓
Camera Optimization	0.05% relative difference between initial and optimized internal camera parameters	✓
Matching	median of 3254.52 matches per calibrated image	✓
Georeferencing	yes, no 3D GCP	⚠

Preview

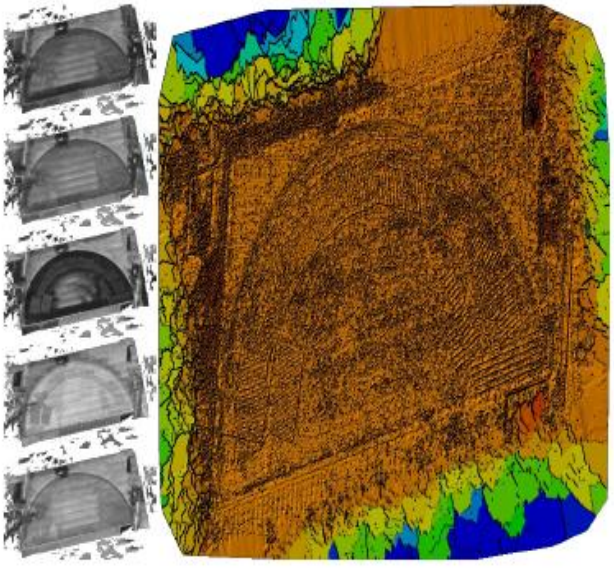

Figure 1: Orthomosaic and the corresponding sparse Digital Surface Model (DSM) before densification.

Report available on:

https://drive.google.com/drive/folders/1W_VpwfUDQ_jSl_PRjc3Snx4YtF0KqW1g?usp=sharing

Appendix III: Multispectral UAV data processing report (14 October 2020)

Processing Report

esri

Generated with Drone2Map for ArcGIS

Summary

Project	HW14102020MS3
Processed	2020-11-11 17:42:34
Camera Model Name(s)	RedEdge-M_5.5_1280x960 (Blue), RedEdge-M_5.5_1280x960 (Green), RedEdge-M_5.5_1280x960 (Red), RedEdge-M_5.5_1280x960 (NIR), RedEdge-M_5.5_1280x960 (Red edge)
Average Ground Sampling Distance (GSD)	6.25 cm / 2.46 in
Area Covered	0.386 km^2 / 38.5569 ha / 0.15 sq. mi. / 95.3254 acres
Time for Initial Processing (without report)	04h:32m:22s

Quality Check

Images	median of 5065 keypoints per image	⚠
Dataset	2821 out of 2990 images calibrated (94%), all images enabled, 5 blocks	⚠
Camera Optimization	0.72% relative difference between initial and optimized internal camera parameters	✓
Matching	median of 3093.46 matches per calibrated image	✓
Georeferencing	yes, no 3D GCP	⚠

Preview

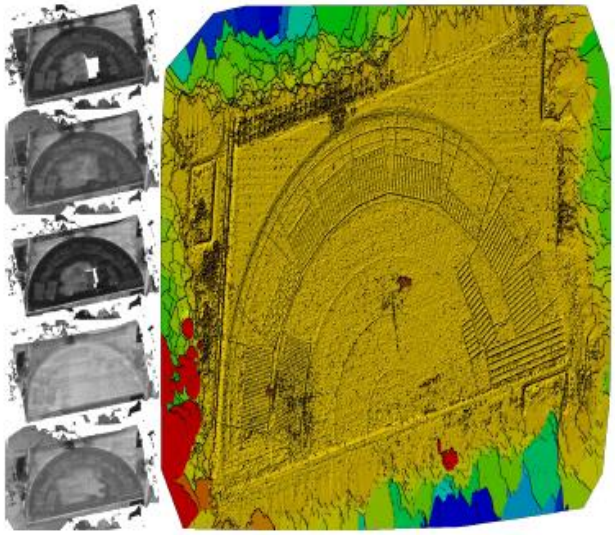

Figure 1: Orthomosaic and the corresponding sparse Digital Surface Model (DSM) before densification.

Report available on:

https://drive.google.com/drive/folders/1W_VpwfUDQ_jSl_PRjc3Snx4YtF0KqW1g?usp=sharing

Appendix IV: The calibration for the RED and NIR bands based on the calibration panel images

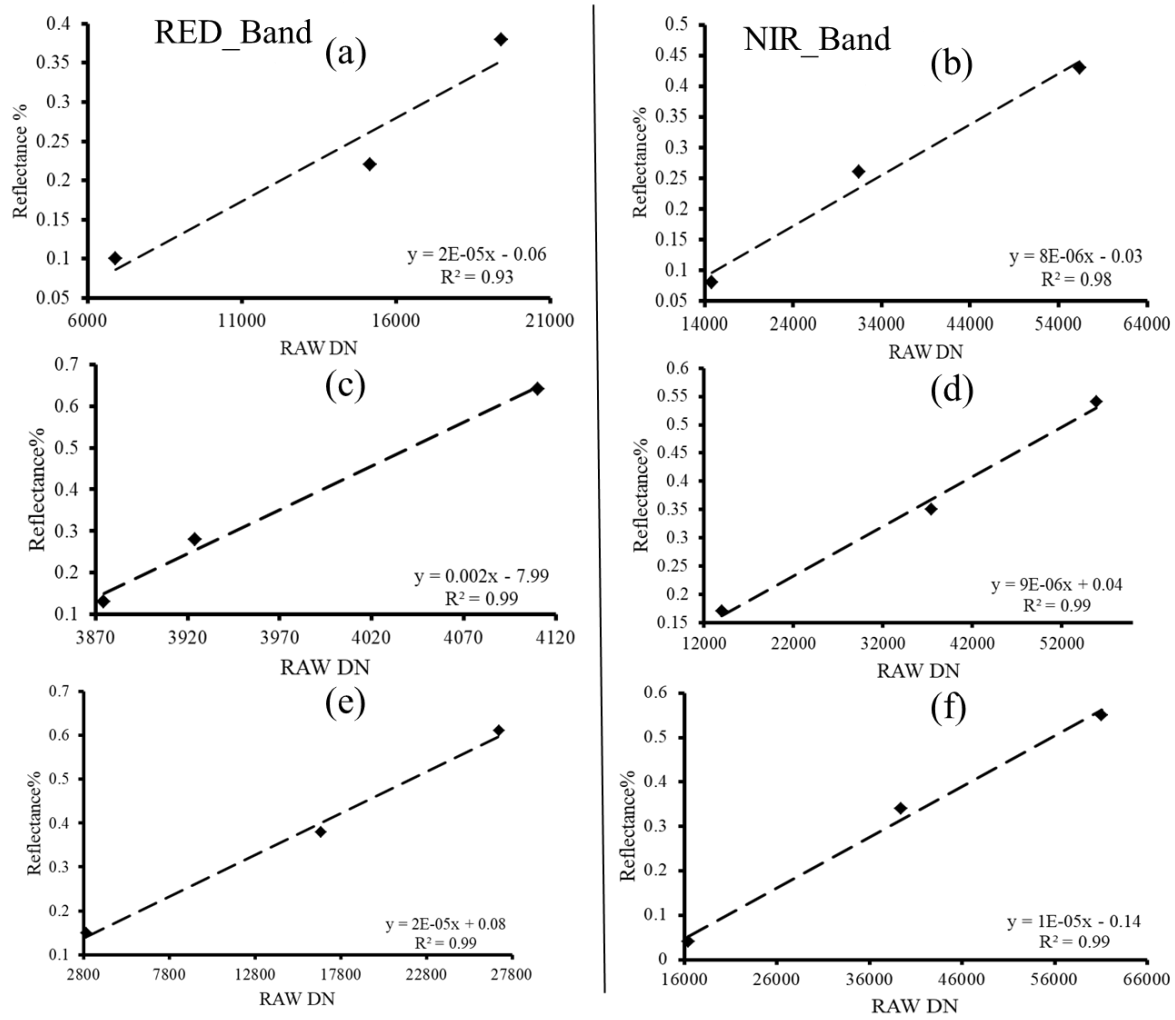

(a and b are the Red and NIR bands for 10 August 2020, c and d are the Red and NIR bands for 12 September 2020, while e and f are the Red and NIR bands for 14 October 2020).